The Deacon Process from the Perspective of Surface Science: HCl Oxidation on CeO_{2-x}(111)/Ru(0001) Thin Films

Genehmigte Dissertation

zur Erlangung des akademischen Grades

Doktor der Naturwissenschaften

- Dr. rer. nat. -

vorgelegt dem

Fachbereich Biologie und Chemie

der

Justus-Liebig-Universität Gießen

von

Volkmar Koller

Gießen, März 2024

“Now go, get the paprika!”

Melinda

1. Gutachter: Prof. Dr. Herbert Over

2. Gutachter: Prof. Dr. Bernd Smarsly

Die vorliegende Arbeit wurde im Zeitraum von Juni 2019 bis März 2024 am Physikalisch-Chemischen Institut der Justus-Liebig-Universität Gießen unter Betreuung von Prof. Dr. Herbert Over angefertigt.

Selbständigkeitserklärung

Ich erkläre:

Ich habe die vorgelegte Dissertation selbstständig und ohne unerlaubte fremde Hilfe und nur mit den Hilfen angefertigt, die ich in der Dissertation angegeben habe. Alle Textstellen, die wörtlich oder sinngemäß aus veröffentlichten Schriften entnommen sind, und alle Angaben, die auf mündlichen Auskünften beruhen, sind als solche kenntlich gemacht. Ich stimme einer evtl. Überprüfung meiner Dissertation durch eine Antiplagiat-Software zu. Bei den von mir durchgeführten und in der Dissertation erwähnten Untersuchungen habe ich die Grundsätze guter wissenschaftlicher Praxis, wie sie in der „Satzung der Justus-Liebig-Universität Gießen zur Sicherung guter wissenschaftlicher Praxis“ niedergelegt sind, eingehalten.

Reuse Permissions

The results of the present thesis are published in the two publications given below. Figures and text passages are adapted, complemented, and reprinted with the here stated permissions and labelled in the thesis as reference[1] and reference[2] respectively:

First publication, reference[1]: Adapted and reprinted with permission from Koller, V.; Sack, C.; Lustemberg, P.; Ganduglia-Pirovano, M.V.; Over, H. Dynamic Response of Oxygen Vacancies in the Deacon Reaction over Reduced Single-Crystalline CeO_{2-x}(111) Surfaces. *J. Phys. Chem. C* **2022**, *126*, 13202–13212, DOI: 10.1021/acs.jpcc.2c03821

Second publication, reference[2]: Koller, V.; Lustemberg, P., Spriewald-Luciano, A.; Gericke, S.M.; Larsson, A.; Sack, C., A.; Preobrajenski, A.; Lundgren, E.; Ganduglia-Pirovano, M.V.; Over, H. Critical Step in the HCl Oxidation Reaction over Single-Crystalline CeO_{2-x}(111): Peroxo-Induced Site Change of Strongly Adsorbed Surface Chlorine. *ACS Catal.* **2023**, *13*, 12994–13007, DOI: 10.1021/acscatal.3c03222

List of Publications

i. *Critical Step in the HCl Oxidation Reaction over Single-Crystalline CeO_{2-x}(111): Peroxo-Induced Site Change of Strongly Adsorbed Surface Chlorine.*
Koller, V.; Lustemberg, P.G.; Spriewald-Luciano, A.; Gericke, S.M.; Larsson, A.; Sack, C., A.; Preobrajenski, A.; Lundgren, E.; Ganduglia-Pirovano, M.V.; Over, H.
ACS Catal. **2023**, *13*, 12994–13007.

ii. *Dynamic Response of Oxygen Vacancies in the Deacon Reaction over Reduced Single-Crystalline CeO_{2-x}(111) Surfaces.*
Koller, V.; Sack, C.; Lustemberg, P.; Ganduglia-Pirovano, M.V.; Over, H.
J. Phys. Chem. C **2022**, *126*, 13202–13212.

iii. *Dynamics of Early-Stage Oxide Formation on a Ni-Cr-Mo Alloy.*
Larsson, A.; Gericke, S.M.; Grespi, A.; **Koller, V.**; Eidhagen, J.; Yue, X.; Frampton, E.; Appelfeller, S.; Generalov, A.; Preobrajenski, A.; Pan, J.; Over, H; Lundgren, E.
npj Mater. Degrad. **2024**, *8*, 39.

iv. *Operando Stability Studies of Ultrathin Single-Crystalline IrO_2(110) Films under Acidic Oxygen Evolution Reaction Conditions.*
Weber, T.; Vonk, V.; Escalera-López, D.; Abbondanza, G.; Larsson, A.; **Koller, V.**; Abb, M.J.S.; Hegedüs, Z.; Bäcker, T.; Lienert, U.; Harlow, G.S.; Stierle, A.; Cherevko, S.; Lundgren, E.; Over, H.
ACS Catal. **2021**, *11*, 12651–12660.

v. *Thermal Stability of Single-Crystalline IrO_2(110) Layers: Spectroscopic and Adsorption Studies.*
Abb, M.J.S.; Weber, T.; Langsdorf, D.; **Koller, V.**; Gericke, S.M.; Pfaff, S.; Busch, M.; Zetterberg, J.; Preobrajenski, A.; Grönbeck, H.; Lundgren, E.; Over, H.
J. Phys. Chem. C **2020**, *124*, 15324–15336.

vi. *Interaction of HCl with a CeO_2(111) Layer Supported on Ru(0001): A Theory and Experiment Combined Study.*
Sack, C.; Lustemberg, P.G.; **Koller, V.**; Ganduglia-Pirovano, M.V.; Over, H.
J. Phys. Chem. C **2018***, 122*, 19584–19592.

vii. *Nonexponential Kinetics of Ion Pair Dissociation in Electro Freezing Water.*
Alaghemandi, M.; **Koller, V.**; Green, J.R.
Phys. Chem. Chem. Phys. **2017***, 19*, 26396–26402.

Acknowledgements

First of all, I would like to thank **Prof. Dr. Herbert Over** for his encouraging interest in the HCl oxidation and his constant support during all stages of my graduate and doctorate studies. He has always an open door for questions and I appreciate his solution-oriented thinking and enabling a constructive and helping working atmosphere inside the working group.

Secondly, I would like to thank **Prof. Dr. Bernd Smarsly** for taking over the second review of this thesis and his working group's support during daily lab work.

Thirdly, I would like to thank **Prof. Dr. Jürgen Janek** for his interest to carry on the HCl oxidation research in a DFG project and for a partial funding of my PhD. Additionally, I would like to thank him and his working group and all members of the physical-chemical institute for an uncomplicated use of the research infrastructure.

Another special thanks go to **Prof. Dr. Wolfgang Moritz** in Munich for his help and advice in the analysis and interpretation of low-energy electron diffraction data.

Moreover, I would like to **Prof. Dr. Edvin Lundgren** and **Dr. Alexei Preobrajenski** for making the beamtime at FlexPES, MAX IV in Lund, Sweden in November 2021 possible which results are a core element of this thesis.

Likewise, my special thanks go to **Dr. M. Verónica Ganduglia-Pirovano** and **Dr. Pablo G. Lustemberg** in Madrid, Spain for the fruitful collaboration of experiment and theory. I am grateful for **Pablo's** *Mercator* visit in Gießen which promoted the project, by corroborating the findings of the beamtime via additional computational studies.

Especially, I would like to thank **Dr. Christian Sack** for his previous achievements on the HCl oxidation over cerium dioxide and I would like to thank him for introducing me to work with ultrahigh vacuum technology during my Master's thesis and passing on his knowledge on the ruthenium-supported cerium dioxide thin film system.

Furthermore, I would like to thank **Dr. Alexander Generalov**, **Dr. Sabrina M. Gericke**, **Dr. Alfred Larsson**, **Alexander Spriewald-Luciano** for their work during the beamtime at FlexPES in November 2021 and **Dr. Stephan Appelfeller**, **Dr. Lindsay R. Merte**, **Dr. Sara Blomberg** and **Dr. Sebastian Pfaff** for their work during the pioneering beamtime at FlexPES in June 2020.

Also, I would like to thank **Alexander Spriewald-Luciano** and **Florian Rink** for continuing the project by moving the model system to ambient pressure.

Likewise, I would like to thank all members and former members of the Over research group for their work, help and mutual support, namely **Prof. Dr. Franziska Heß, Dr. Marcel Abb, Dr. Tim Weber, Dr. Daniel Langsdorf, Dr. Omeir Khalid, Dr. Yu Sun, Dr. Chenwei Li, Dr. Phillip Timmer, Dr. Wei Wang, Dr. Zheng Wang, Alexander Spriewald-Luciano, Lorena Glatthaar, Yu Wang,** and especially our secretary **Gabi Scheller**. Also I would like to thank **PD Dr. Georg Mellau** and **Hansjörg Ruppender** for technical support.

Additionally, I would like to thank the members of the physical-chemical institute, in particular **Dr. Bjoern Luerßen**, **Dr. Boris Mogwitz**, **Dr. Klaus Peppler**, **Dr. Felix Richter**, **PD Dr. Marcus Rohnke**, **Dr. Joachim Sann**, **Kvetoslava Pica**, **Kerstin Rose**, and

Antonella D'Ambrosio for their work and help in all situations. Especially I would like to thank the members of the electronical and mechanical workshop **Harald Weigand**, **Harry Heidt**, and **Ralf Sack** for their fast and constructive help in all situations, which made progress in the lab possible.

I would like to thank **Dr. Tim Weber** and **Melinda Csenki** for proof reading and their constructive and helpful feedback.

Finally, I would like to thank my parents **Brunhilde** and **Horst**, my godfather **Fritz**, my sisters **Dorothea** and **Catharina,** my grandmother **Karoline,** and my friends, with special thanks to my girlfriend **Melinda** for their endless support and company during my studies and the thesis in all situations.

Abstract

Chlorine is a basic chemical essential for a broad range of products, with a current annual demand of 90 million tons. However, hydrogen chloride is often an inevitable byproduct, accumulating to around ten million tons per year. A sustainable way to solve this waste issue is to recover molecular chlorine by thermal catalysis in the Deacon process ($4\ HCl + O_2 \rightarrow 2\ Cl_2 + 2\ H_2O$). Compared to conventional hydrogen chloride electrolysis, only 15% of the energy is required. Cerium oxide is a viable catalyst for this reaction, which is active yet stable, but it is still unclear why. A reaction mechanism has been proposed based on density functional theory (DFT) calculations, but it has yet to be confirmed experimentally.

The approach for corresponding model studies in this work is to divide the overall reaction into two half-reactions, based on so-called chemical looping, where the catalyst is alternately cycled between two reactants. Similarly, the proposed mechanism for the Deacon process over $CeO_{2-x}(111)$ can also be divided: first, the catalyst is exposed to HCl, corresponding to an exothermic surface chlorination process, and the byproduct water is formed. Secondly, oxygen is activated upon exposure and adsorbed, and chlorine is formed in an endothermic de-chlorination process.

The model catalyst, i.e., single-crystalline reduced $CeO_{2-x}(111)$ thin films, is prepared via physical vapor deposition PVD. The films are characterized using dedicated surface-sensitive methods: X-ray photoelectron spectroscopy XPS, near edge X-ray absorption fine structure NEXAFS, low-energy electron diffraction LEED, X-ray reflectivity XRR, and temperature programmed desorption TPD. Complementary density functional theory calculations DFT+U are realized in collaboration.

First, chlorination of the reduced cerium oxide is modeled on reduced single-crystalline $CeO_{2-x}(111)$ model surfaces, which stabilizes various ordered surface structures, e.g., $(\sqrt{7} \times \sqrt{7})R19.1°$, (3×3), or (4×4), depending on the concentration of oxygen vacancies (V_O). Saturating these phases with HCl at room temperature, followed by annealing to the Deacon process temperature of 700 K, results for all cases in a uniformly covering $(\sqrt{3} \times \sqrt{3})R30°$-$Cl_{vac}$ overlayer structure with identical coverage and adsorption geometry of Cl in oxygen vacancies (Cl_{vac}). Water or hydrogen formation can be observed depending on the reduction degree x. In order to rationalize why the formation of the $(\sqrt{3} \times \sqrt{3})R30°$-$Cl_{vac}$ structure on $CeO_{2-x}(111)$ is independent of the original reduction degree x of $CeO_{2-x}(111)$ efficient diffusion of surface and bulk oxygen vacancies is required.

Second, as a key experiment, the stepwise re-oxidation of the chlorinated surface is investigated. Here, the displacement of tightly bound chlorine in an oxygen vacancy is predicted to be the most critical step. Synchrotron-based XPS and NEXAFS disentangle the surface and bulk properties of the surface-chlorinated model catalyst during re-oxidation. The re-oxidation process is found to start from the bulk of the catalyst and propagate towards the surface. Chlorine recombines and forms the desired product Cl_2 solely during surface oxidation. DFT+U calculations evidence Cl is displaced by an adsorbed peroxo species in a concerted reaction, likely not being the rate determining step. The formation and dissociation of the peroxide species drive the re-oxidation and de-chlorination processes, hence being considered essential for cerium oxide-based catalysis in general.

Kurzfassung

Chlor ist eine Grundchemikalie, die für eine Vielzahl von Produkten und Gütern unentbehrlich ist. Weltweit beträgt der jährliche Bedarf derzeit etwa 90 Millionen Tonnen. Chlorwasserstoff ist häufig ein unvermeidbares Nebenprodukt bei der Chlorverwendung, mit einer Gesamtmenge von etwa 10 Millionen Tonnen pro Jahr. Eine nachhaltige Möglichkeit zur Lösung dieses Abfallproblems ist die Rückgewinnung von molekularem Chlor durch thermische Katalyse im Deacon-Verfahren ($4\ HCl + O_2 \rightarrow 2\ Cl_2 + 2\ H_2O$). Im Vergleich zur konventionellen Chlorwasserstoff-Elektrolyse werden hierbei nur 15 % der Energie benötigt. Ceroxid ist ein vielversprechender Katalysator für diese Reaktion, der aktiv und dennoch stabil ist. Ausgehend von Dichtefunktionaltheorie-Rechnungen (DFT) wurde ein Reaktionsmechanismus vorgeschlagen, der allerdings noch nicht experimentell verifiziert wurde.

Der in dieser Arbeit vorgestellte Ansatz für entsprechende Modellstudien besteht darin, die Gesamtreaktion in zwei Halbreaktionen zu unterteilen, die auf dem so genannten chemischen Looping basieren, bei dem der Katalysator abwechselnd zwischen zwei Reaktanten zirkuliert wird. Der vorgeschlagene Mechanismus für den Deacon-Prozess über $CeO_{2-x}(111)$ lässt sich ebenfalls auf diese Weise unterteilen: Zunächst wird der Katalysator durch HCl in einem exothermen Schritt chloriert, wodurch Wasser als Nebenprodukt entsteht. Anschließend wird die Exposition von Sauerstoff, dieser aktiviert und adsorbiert, und Chlor in einem endothermen Dechlorierungsprozess gebildet.

Der Modellkatalysator, in Form einkristalliner, reduzierter $CeO_{2-x}(111)$ Dünnschichten, wurde durch physikalische Gasphasenabscheidung (PVD) präpariert und mit verschiedenen oberflächensensitiven Methoden charakterisiert: Röntgenphotoelektronenspektroskopie XPS, Röntgen-Nahkanten-Absorptions-Spektroskopie NEXAFS, Niederenergie-Elektronenbeugung LEED, Röntgenreflektometrie XRR und temperaturprogrammierter Desorption TPD. Komplementäre Dichtefunktionaltheorieberechnungen DFT+U wurden in einer Kooperation realisiert.

Reduzierte einkristalline $CeO_{2-x}(111)$ Oberflächen können, abhängig von der Konzentration der Sauerstoffleerstellen (V_O), verschiedene geordnete Oberrekonstruktionen ausbilden, z. B. $(\sqrt{7} \times \sqrt{7})R19.1°$, (3×3), oder (4×4). Die Sättigung dieser Phasen mit HCl bei Raumtemperatur und ein Heizschritt auf die Deacon-Verfahrenstemperatur von 700 K führt in allen Fällen zu einer gleichmäßig bedeckten $(\sqrt{3} \times \sqrt{3})R30°$-$Cl_{vac}$-Überstruktur mit identischer Bedeckung und Adsorptionsgeometrie von Cl in Sauerstofflücken (Cl_{vac}). Die Bildung von Wasser oder Wasserstoff kann in Abhängigkeit des Reduktionsgrads x beobachtet werden. Unabhängig vom ursprünglichen Reduktionsgrad x ist für die Ausbildung der $(\sqrt{3} \times \sqrt{3})R30°$-$Cl_{vac}$-Überstruktur eine effiziente Diffusion von Sauerstoffleerstellen an der Oberfläche und im Volumen erforderlich.

Als Schlüsselexperiment wurde die schrittweise Reoxidation der chlorierten Oberfläche untersucht, da die Aktivierung von Chlor als ratenbestimmender Schritt vorhergesagt wird (DFT). Mit Synchrotron basiertem XPS und NEXAFS wurden die Oberflächen- und Volumeneigenschaften des oberflächenchlorierten Modellkatalysators während der Reoxidation analysiert. Es konnte gezeigt werden, dass der Reoxidationsprozess im Volumen beginnt und Chlorbildung ausschließlich während der Oberflächenoxidation stattfindet. DFT+U-Rechnungen konnten zeigen, dass Cl hierbei durch eine adsorbierte Peroxospezies in einer konzertierten Reaktion aktiviert wird, und dies somit nicht dem geschwindigkeitsbestimmenden Schritt entspricht. Die beschriebene Peroxospezies ist für Ceroxid-basierte Katalysatoren von grundlegender Bedeutung.

Table of Contents

1 Introduction

Chlorine is a chemical element with the atomic number 17 and belongs to the group of the halogens. In industry, it is a basic chemical with a current annual production of an estimated 90 Mt worldwide[3,4] including an estimated 10 Mt in Europe[5] in 2021. Most chlorine is produced via the chlor-alkali process, which is the electrolysis of an aqueous sodium chloride solution (brine) that also produces sodium hydroxide NaOH. It is estimated "that over 50% of all the industrial chemicals and polymers depend on chlorine",[6] which, however, is no longer contained in one third of the final products.[7] A key example is the production of the three polymers polyurethane PU, polycarbonate PC, and polyvinyl chloride PVC for which more than half of the chlorine produced is consumed.[6] PU, PC, and PVC, are encountered every day in broad range of applications: PU is often used as foam in insulation materials, as well as mattress, seat upholstery, shoe soles, or sponges. Polycarbonate has a broad application in electronic devices because of its outstanding electrical insulation and stability.[8] Due to its transparency it is also suited for durable glasses or for CDs, DVDs, and Blu-rays as well as safety goggles in the laboratory. PVC is used, e.g., for piping, window frames, and flooring, but also for daily consumer products like credit cards or basket balls. **Figure 1.1** depicts the exemplified manufacturing process of polycarbonate:

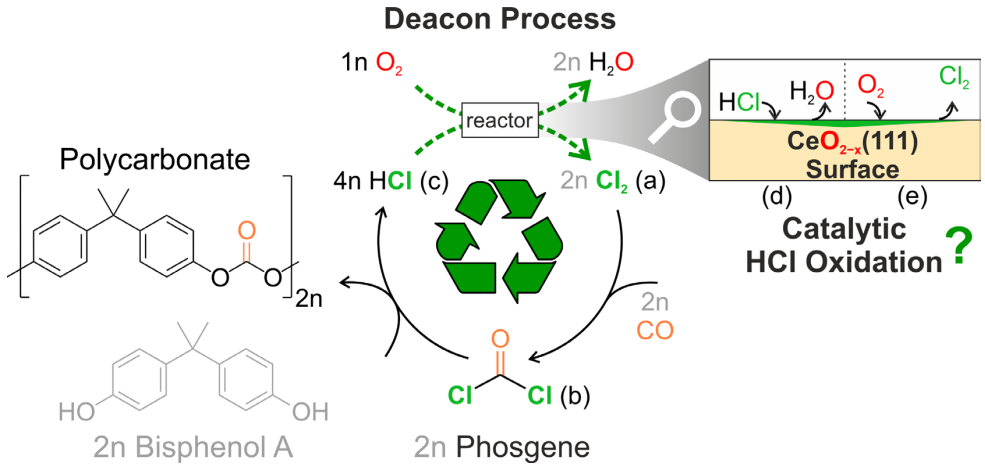

Figure 1.1: The chlorine cycle depicted as for the production of polycarbonate. The cycle starts with chlorine Cl_2 (a) oxidizing carbon monoxide to phosgene while Cl_2 is reduced (b). In a condensation reaction of phosgene with bisphenol A, the desired product polycarbonate is formed, yielding HCl (c) as a byproduct in the ratio 1:2. The cycle is closed by the catalytic HCl oxidation (Deacon process) with oxygen to recover chlorine and form water as a byproduct. As a viable catalyst, cerium dioxide is investigated in dedicated model experiments, i.e,. on $CeO_{2-x}(111)$ thin films separated in a chlorination step (d) and de-chlorination (e) step. Inspired by reference[9].

Conventionally, chlorine (**Figure 1.1**a) from the chlor-alkali process is used as an oxidizing agent here for carbon monoxide CO, yielding phosgene $COCl_2$ (**Figure 1.1**b) by changing the oxidation state of the carbon atom from +II to +IV, while the two chlorine atoms are reduced from 0 to −I. Afterwards, phosgene can react in a condensation reaction with Bisphenol A to form the desired product polycarbonate. However, during the condensation two moles HCl are formed per mole monomeric unit polycarbonate as residual waste product. In the case of polyurethane, with diisocyanates as key intermediate, the ratio is even 1:4, meaning that per monomeric unit four moles of HCl are generated.

Partially, HCl can be used in the production of PVC, as the polymer contains one chlorine atom per monomeric unit. However, in the end, there is an increasing excess of around 10 Mt HCl omnipresent waste, which the market cannot absorb.[2] In the future this issue is expected to aggravate, as, for example, the demand for superior PU and PC is rising faster than that for PVC.[6] Commonly, the HCl waste is processed in HCl electrolysis or even in neutralization with a base, which is energy intensive and undesirable.[7,10–12] Additionally HCl originates in large scales from metallurgy processes.[10]

The issue of excess HCl as waste product dates back to the end of the 19th century, due to the production of sodium sulfate Na_2SO_4 as the basis for the historic Leblanc process (soda ash Na_2CO_3 production). Given this, Henry Deacon and Ferdinand Hurter[6,13] started around 1870 to develop the heterogeneously catalyzed oxidation of HCl with molecular oxygen O_2 (Deacon-Hurter process):[14,15]

$$\overset{+I\ -I}{4\,HCl} + \overset{0}{O_2} \rightarrow \overset{0}{2\,Cl_2} + \overset{+I\ -II}{2\,H_2O} \qquad \Delta_r H = -114\ \text{kJ/mol} \quad (1.1)$$

Here, four moles of HCl (**Figure 1.1**c) are oxidized by one mole of oxygen via a solid catalyst to recover two moles of desired chlorine and two moles of water as a side product containing the reduced oxygen. During the HCl oxidation four electrons and four hydrogen atoms need to be transferred from the four chlorine atoms to the two oxygen atoms. This process closes the depicted chlorine cycle (cf. **Figure 1.1**) and offers the possibility to recycle HCl directly at the production site where it is generated, enabling a circular economy. This is especially desirable, as chlorine, phosgene, and HCl are toxic and corrosive gases. The main advantage of thermal heterogeneous catalysis is its low energy utilization of only 15% compared to conventional HCl electrolysis.[9] However a active yet stable, but also environmentally safe and economically viable catalyst is essential for a successful application which has been a challenge for over 150 years (cf. **Chapter 3.1**).

The original cupric chloride $CuCl_2$-based catalyst used by Deacon and Hurter suffered from volatilization of $CuCl_2$ at high temperatures. A breakthrough only at the end of the last century was the development of a ruthenium oxide RuO_2-based catalyst supported on rutile-TiO_2 by Sumitomo Chemical. Although being commercialized, RuO_2-based catalyst faces several challenges: ruthenium is a rare platinum group metal with an annual world production of 20-30 t per year, thus making it susceptible to severe price fluctuations. Furthermore, RuO_2-based catalysts exhibit stability issues due to volatilization at high temperatures which requires a challenging isothermal reactor design.

A recently discussed[6,16,17] and abundant alternative to ruthenium oxide is cerium dioxide. CeO_2 is active and stable at a typical reaction temperature of 700 K and in a wide range of process parameters.[2] Cerium ($6.55 \cdot 10^1$ mg/kg) is much more abundant than ruthenium ($1 \cdot 10^{-3}$ mg/kg) in the earth's crust.[18] In addition, CeO_2-based catalysts allow for running the flow reactor under adiabatic reaction conditions, thereby reducing investment costs.[2,16,19] However, the reaction mechanism of the Deacon process on CeO_2-based catalysts is still elusive. "A more detailed understanding of the catalytic reaction mechanism associated with the process"[10] may be important for a successful optimization of the catalyst. In the case of RuO_2, the reaction mechanism has been successfully resolved using dedicated single-crystalline RuO_2(110) model catalyst systems (cf. **Chapter 3.3**). In

previous studies Amrute et al. proposed a reaction mechanism over defective $CeO_2(111)$-surfaces based on model experiments on powder samples and computational density functional theory DFT+U calculations.[16] Subsequently, CeO_2-based catalysts have been further investigated utilizing model catalysts with a specific morphology (e.g., fibers[20] or nanoparticles[21]), doping[22–24] or the use of a supporting material[25] (cf. **Chapter 4.2**). However, the experimental verification of the proposed reaction mechanism remains. Pioneering experimental surface science studies using dedicated single-crystalline $CeO_2(111)$ thin films[26,27] were conducted in the Over research group by Christian Sack.[28] They formed a foundation for the present thesis (cf. **Chapter 4.4**, **6.5**, and **7.1**). Generally, in surface science, a system, e.g., a catalyst, is investigated under structurally and chemically controlled conditions (e.g., single-crystallinity and ultrahigh vacuum, respectively). Here, the identification of a suitable model system (i.e., $RuO_2(110)$ or $CeO_{2-x}(111)$) and how the catalytic reaction can be investigated under ultra-high vacuum UHV conditions is of vital importance.

For the Deacon process it can be shown that the proposed reaction mechanism (cf. **Chapter 5.1**) can be split in to an HCl-driven "chlorination" and an oxygen-driven "de-chlorination" of the catalyst. (cf. **Chapter 5.2**). The separation of a catalytic reaction in reactor design is known as chemical looping[29] and was already investigated in pilot studies for the Deacon process.[30] In simple terms, the catalyst is cycled between two reactors and alternatingly exposed to the two educts of the catalytic reaction. Transferred to dedicated model studies, in a first step[1] the "chlorination" can be investigated by exposing HCl to reduced $CeO_{2-x}(111)$-surfaces as the fully oxidized $CeO_2(111)$-surface was shown to be inactive.[31] The findings and results from previous work are categorized in this context and complemented with additional experiments (cf. **Chapter 7.1**). In a second step[2] the chlorinated, yet reduced surface acts as model system for the oxygen driven "de-chlorination." The present thesis focuses on the latter step, as the de-chlorination, i.e. the activation of a chlorine atom from an oxygen vacancy, has been proposed to be the most energy-demanding step of the reaction. Furthermore, it is as yet unclear how an oxygen molecule can be activated on a chlorinated surface. For a detailed investigation, the second model system was prepared in a dedicated synchrotron beamtime using X-ray photoelectron spectroscopy XPS and near edge X-ray absorption fine structure NEXAFS. In this way, the surface and bulk properties of the model catalyst surface region could be disentangled. In addition, lab-based XPS, low-energy electron diffraction LEED, temperature programmed desorption TPD and X-ray reflectivity XRR experiments are utilized. In order to use the full strength of the surface science approach, complementary computational DFT+U calculations were carried out in collaboration with M. Veronica Ganduglia-Pirovano and Pablo G. Lustemberg.

2 Methods

The methods used in this work can be classified as a classic surface science approach.[32] Instead of a catalyst applied in a reactor, a suitable model catalyst or system is investigated. In the following the surface science methods (**Figure 2.1**) utilized for the investigation of the CeO_{2-x}(111) thin film model system are briefly explained. In general, for the investigation of a sample a testing probe is required (e.g., photons *hv* of a specific wavelength) and the response of the sample (e.g., in the form of emitted electrons) needs to be quantifiable.[33]

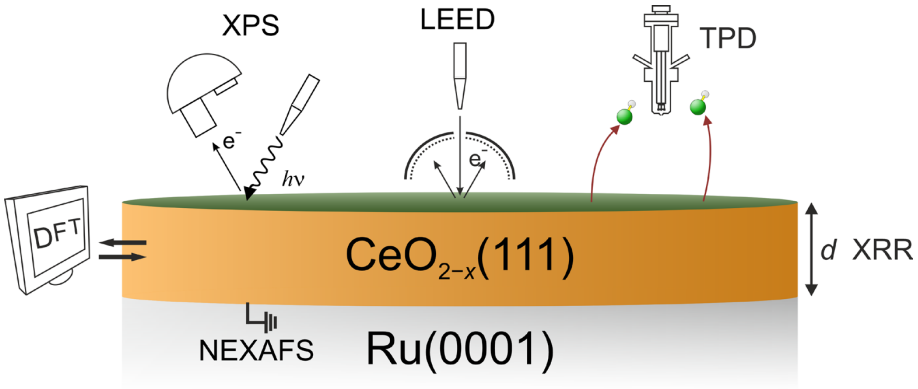

Figure 2.1: Overview of the used methods for investigation of the CeO_{2-x}(111) thin film model catalyst system: X-ray photoelectron spectroscopy XPS, near edge X-ray absorption fine structure NEXAFS, low energy electron diffraction LEED, X-ray reflectivity XRR, temperature programmed desorption and complementary density functional theory DFT+U. Adapted from reference[34].

In the present thesis, spectroscopic techniques like XPS and NEXAFS are used to determine the oxidation state of the ceria thin film at different information depth, as well as the amount of chlorine and the chemical state. Structural characterization is achieved with techniques XRR and LEED in order to determine the thickness of the film and the surface diffraction patterns and order, respectively. TPD is used to analyze possible reaction patterns, e.g. water or chlorine formation depending on the reduction degree *x* of the surface.[35] Due to the model character of the system, it is suited for complementary computational methods, i.e. DFT calculations which are realized in a collaboration in order to verify the interpretations drawn from the experimental studies.

2.1 Surface Science Approach

The investigated system in the present thesis is CeO_{2-x} acting as a heterogeneous catalyst for the Deacon process. A CeO_{2-x}(111) thin film constitutes the model catalyst, with the (111)-facet being the most stable surface,[35] thus ensuring structural control. Control of the chemical environment is ensured by working under UHV conditions, with ambient base pressures below $p_{UHV} < 10^{-10}$ mbar. In this way, the educts HCl and molecular oxygen can be dosed under controlled conditions, with pressures up to $p(HCl) < 5 \times 10^{-8}$ mbar and $p(O_2) < 1 \times 10^{-5}$ mbar, respectively.

Most of the experiments in the present thesis were conducted *in situ*, meaning the sample is characterized at the same place where the experiment was conducted, e.g., before and after an HCl dosing step, without breaking UHV conditions. Especially in heterogeneous

catalysis *operando* studies are highly desirable, i.e., while the reaction or an experiment takes places. However, due to the corrosive nature of HCl and the high pressures needed for oxygen, *operando* measurements are limited for the present model system. *Ex situ* characterization of the sample is not possible as adventitious carbon contaminates the ceria surface,[36,37] except for XRR, in which case the influences of adsorbed carbon contaminations are negligible. In addition, water and oxygen can adsorb *ex situ*. A key advantage of the surface science approach is the good comparability with theoretical calculations. Due to the model character of the present CeO_2 system a computational modelling is possible, enabling a combined experiment and theory approach.[38]

2.2 Interaction of Electrons with Matter

A surface can be defined as "range of a phase region, that differs from the bulk, typically in the range of a few atomic layers".[33] In order to investigate a surface often emitted electrons are measured as response to the incoming X-rays (e.g. XPS and NEXAFS) or electrons (e.g. LEED). The emitted electrons escaping from the surface region or underlying bulk thus determine the surface-sensitivity of the measurement. The escape depth respectively information depth of the electrons is determined by how far an electron can travel, e.g., in a solid before it is absorbed. The intensity decay of the electrons can be described with "an exponential first-order decay law typical for the travel of radiation through matter."[33]

$$I(d) = I_0 \exp\left(\frac{-d}{\lambda(E_{\text{kin}})\cos(\theta)}\right) \tag{2.1}$$

With I_0 being the initial intensity before interaction with the solid, d the travelled distance, $\lambda(E_{\text{kin}})$ the inelastic mean free path IMFP, and θ the angle between the surface normal and the detector (cf. **Figure 2.3**). The inelastic mean free path $\lambda(E_{\text{kin}})$ of electrons in a solid is defined as the distance an electron can travel before its intensity decays to $1/e$ of its initial intensity, with e being Euler's number.[33] The inelastic mean free path $\lambda(E_{\text{kin}})$ is dependent on the kinetic energy E_{kin} of the electron and can be described with the so-called universal curve (cf. **Figure 2.2**).

The shape of the curve can be rationalized as follows:[33] for energies higher than ~50 eV the inelastic mean free path $\lambda(E_{\text{kin}})$ increases directly proportional to the electron's kinetic energy, hence velocity, as the time decreases during which the electron might be absorbed passing through a given thickness of a solid.[33] Around 50 eV, the inelastic mean free path $\lambda(E_{\text{kin}})$ passes through a minimum. Below kinetic energies of 20-30 eV the inelastic mean free path $\lambda(E_{\text{kin}})$ rapidly increases as plasmons cannot be excited anymore which is the dominant energy loss mechanism.[33]

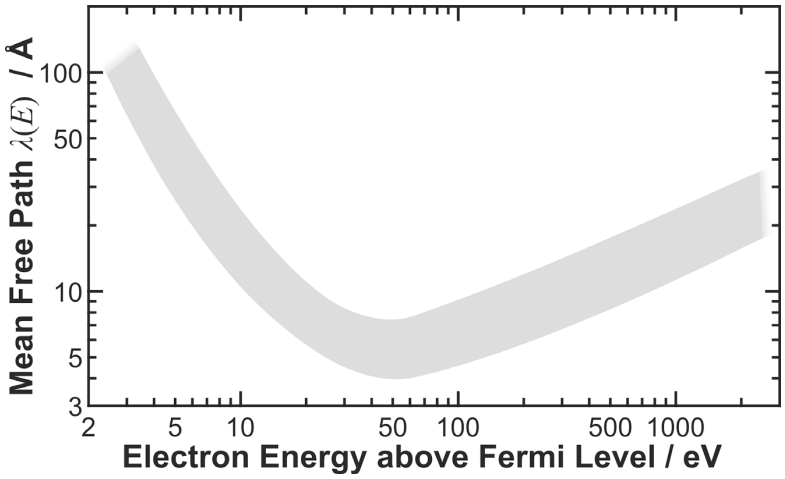

Figure 2.2: Universal curve: the inelastic mean free path $\lambda(E_{kin})$ of an electron in a solid dependent of its kinetic energy.[33] The gray area represents the typically found distribution for different materials.[39] Adapted from reference[39].

Consequently, escaping electrons with kinetic energies between ~50 eV and ~250 eV are the most surface-sensitive, thus suitable for investigating the topmost layers. In the present thesis, surface sensitive electrons are used, in LEED or synchrotron-based XPS. For bulk-sensitive measurements, representing the whole thickness of the film, emitted electrons with either high kinetic energy $E_{kin} > \sim 500$ eV or low kinetic energies $E_{kin} < \sim 20$-30 eV should be detected, which is accomplished in the present thesis via bulk-sensitive XPS or NEXAFS measurements in the total electron yield TEY mode. In addition, for enhanced surface sensitivity the detector angle θ can be adjusted, i.e. by rotating the sample. In this way the effective path length d_{eff} in the solid is increased and a process for energy loss becomes more likely, thus increasing the surface sensitivity.[33]

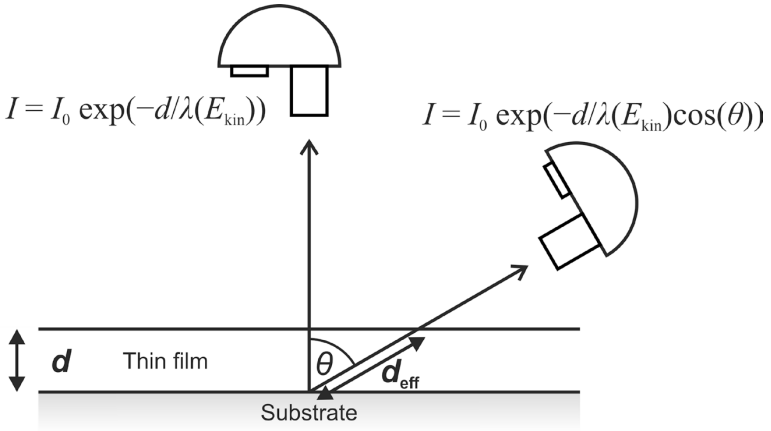

Figure 2.3: Schematic depiction of how going from normal to glancing angles of emission increases the effective path length $(d_{eff}) = d/\cos(\theta)$ from an electron in a solid by variation of the detector angle θ. Adapted from reference[33].

2.3 Generation of X-rays

Essential for the investigation of the sample with XPS, NEXAFS, and also XRR is the generation of X-rays, which "are electromagnetic waves with wavelength λ in the region of an Ångström ($\lambda = 10^{-10}$ m).[40] In the lab, typically X-ray tubes with a fixed wavelength are used, e.g. Mg K_α ($h\nu$ = 1253.6 eV) for XPS. At a synchrotron facility X-rays can be

used in a broad spectrum (e.g. $h\nu = 40 – 1500$ eV at the FlexPES soft X-ray beamline) and techniques like NEXAFS with varied photon energy $E_{h\nu}$ or surface-sensitive XPS can be performed.

2.3.1 Lab-Based Generation of X-rays

In a X-ray tube, electrons are accelerated from a filament towards a cooled metal anode, e.g. made of magnesium ($h\nu$ = 1253.6 eV) or aluminum ($h\nu$ = 1486.6 eV). On the one hand, characteristic X-rays are generated by transitions of electrons between shells (e.g., the K_α transition from the L shell to the K shell, after an electron got removed from the K shell), which is used on the lab-scale for analysis. On the other hand, continuous bremsstrahlung is generated. However, the brilliance of a lab source is approximately a factor of 10^{12} lower[40] compared to a synchrotron source. Hence, for use of X-rays with variable wavelength synchrotron facilities are used instead of the bremsstrahlung of an X-ray tube.

2.3.2 Synchrotron-Based Generation of X-rays

In a synchrotron facility X-rays with variable wavelength and high intensity can be generated. **Figure 2.4** depicts the simplified schematic of the X-ray beamline utilized in the present thesis.

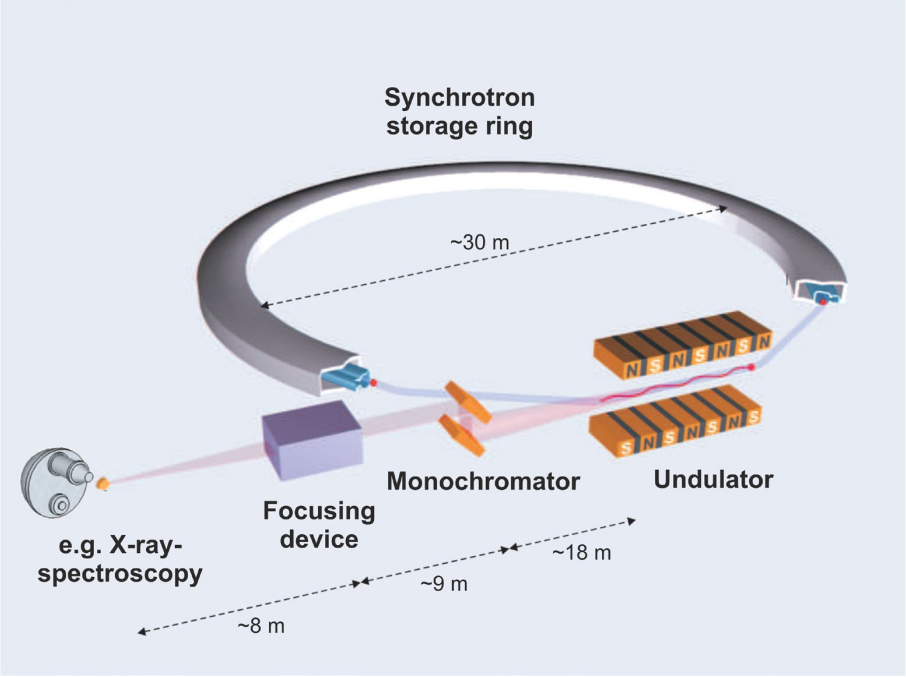

Figure 2.4: Simplified schematic of a synchrotron X-ray beamline. Bunches of electrons circulate (blue) in a storage ring and generate so called "white" X-rays (depicted in red) upon passing of an undulator. The desired X-ray wavelength is adjusted with a monochromator and the now monochromatic beam is focused (focusing device) on the sample in the experimental end station, e.g. for X-ray spectroscopy. Adapted with permission from references[40,41]. © 2011 John Wiley & Sons Ltd.

In principle, bunches of electrons circulate in a storage ring. In case of the FlexPES beamline the 1.5 GeV storage ring has a circumference of 96 m and is designed as a dodecagon with 12 linear sections, for up to 12 beamlines. In the linear sections of the ring an insertion device for the generation of X-rays is placed, which is nowadays typically an

undulator. An undulator consists out of an array of magnets. When an electron passes the array of magnets it is forced to execute small-amplitude oscillations. “At each oscillation X-rays are emitted and, if the amplitude of the oscillations is small, then the different contributions from the passage of a single electron add coherently, and a very intense beam of X-rays results”,[40] called ‘white beam’. To adjust the desired wavelength/energy, the white beam passes a monochromator as a key component of each beamline. Afterwards, depending on the application, the now monochromatic beam can be focused and shaped in a focusing device further downstream and finally reaches the sample for its application in an experiment.

2.4 X-ray Spectroscopy

The X-ray spectroscopy methods used in this work are XPS and NEXAFS. Both techniques are based on the creation of core-holes by absorption of incoming photons *hv*.[42] A core-level electron of an atom can be excited either to a yet bound state (NEXAFS, **Figure 2.5**a) or to the continuum (XPS, **Figure 2.5**b), whereas the latter leads towards ionization. In NEXAFS “the spectroscopy provides information about the empty electronic states above the Fermi level”,[39,42] while in XPS the kinetic energy of the emitted electron is measured and information about the binding energy of the core-level can be obtained.[42] In the present thesis both techniques are used to disentangle surface from bulk properties of the model catalyst, e.g. to determine the degree of oxidation.

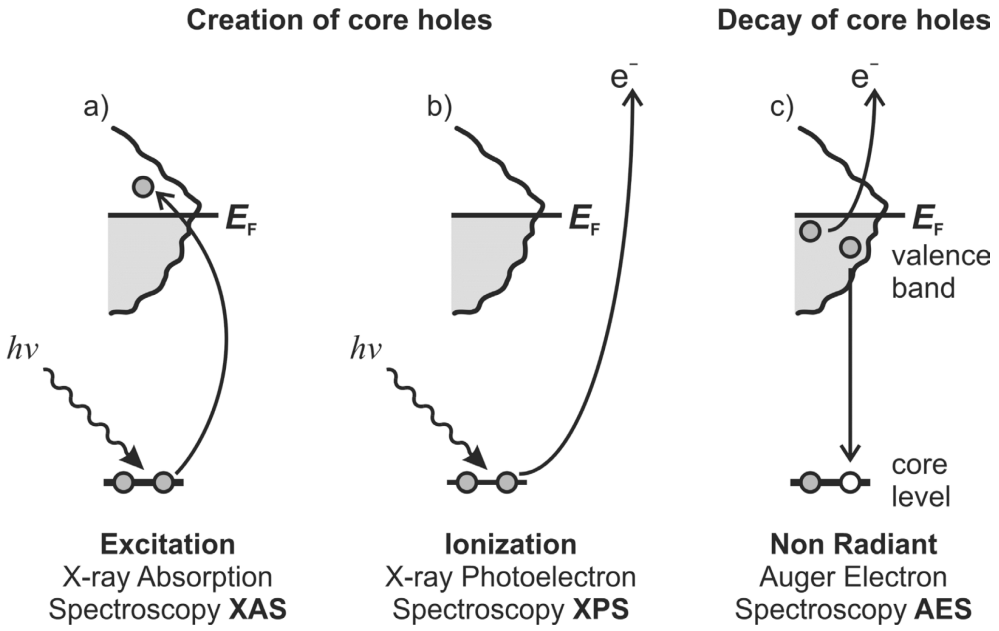

Figure 2.5: Schematic illustration of a) core-level excitation used in X-ray absorption spectroscopy XAS, e.g. NEXAFS, b) ionization used in X-ray photoelectron spectroscopy XPS, and c) non-radiant decay processes used e.g. in Auger electron spectroscopy AES. Adapted with permission from reference[42].

2.4.1 X-ray Photoelectron Spectroscopy - XPS

Basis for X-ray photoelectron spectroscopy is the outer photoelectric effect (Nobel prize 1921, Albert Einstein), meaning that photons *hv* as a probe can induce electron emission as a response. In chemistry XPS is also referred to as electron spectroscopy for chemical

analysis ESCA, for which Kai Siegbahn as developer of the technique was awarded with the Nobel prize in 1981.

For electron emission to occur the energy of the photon $E_{h\nu}$ needs to be larger than the work function ϕ_S (cf. **Figure 2.6**) of the sample.[33] The work function ϕ_S is defined as the minimum energy to remove an electron from the highest occupied level of the solid to the vacuum level E_V.[33] (cf. **Figure 2.6**) The kinetic energy of the emitted electrons E_{kin} can be measured with an analyzer.(cf. **Figure 2.7**) Hence, utilizing a fixed photon energy $E_{h\nu}$ and a given work function ϕ_A of the analyzer being grounded with the sample (cf. **Figure 2.6**), the binding energy E_{BE} of the emitted electron can be determined via the following equation:

$$E_{BE} = E_{h\nu} - (E_{kin} + \phi_A) \tag{2.2}$$

The binding energy E_{BE} is referenced to the Fermi-level E_F of the spectrometer, to which the sample is connected electrically.[33]

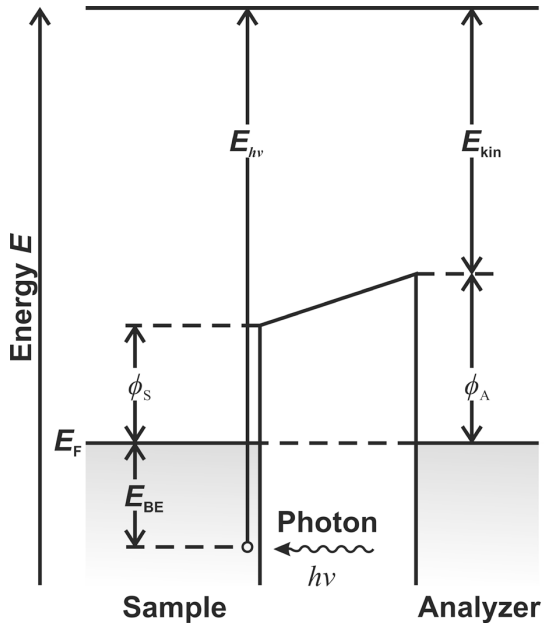

Figure 2.6: Energy-level diagram of photoelectron spectroscopy: A photon of energy $E_{h\nu}$ excites an electron of binding energy E_b (w.r.t. the Fermi level E_F). The measured kinetic energy of the photoelectron E_{kin} is referenced to the electron spectrometer with the work function ϕ_A. Adapted from reference[43].

Emission of an electron can occur from core levels and valence levels from the atoms of a solid. "Core levels are defined as inner quantum shells which do not participate in chemical bonding"[33] while "valence levels are defined as electrons in the more weakly bond partially filled outer quantum shells",[33] which can participate in chemical bonding. Emitted core level electrons can be used for the chemical identification of an element as the binding energy E_{BE} of a core level, e.g. 1 s, is dependent on the charge of the nucleus of the atom/element. E.g., the binding energy of oxygen 1 s ~532eV is greater than for carbon 1 s ~284 eV, cf. **Figure 2.8**.

In addition to the information about the chemical elements, the core level also contains information about the chemical environment. In a first approximation the determined binding energy E_{BE} is the negative orbital energy of the emitted electron (Koopmans'

theorem, $E_{BE} = -\varepsilon$). However, Koopmans' theorem seldom applies as initial (before photoionization) and final (after photoionization) state effects alter the measured kinetic energy E_{kin} and thus the determined binding energy E_{BE}. The binding energy of the core level is influenced by valence levels (initial state effect) as the outer quantum shell has charge density close to the core, hereby influencing the shielding of the core electron from the nucleus. This can be used to probe the chemical environment, e.g. oxidation state or adsorption site on a surface. Furthermore, the determined binding energy ($E_{BE} = -\varepsilon - \varepsilon_{relax} - \varepsilon_{rel} - \varepsilon_{corr}$) can be influenced by, e.g. the remaining electrons, which may relax to minimize their total energy ε_{relax}, relativistic effects ε_{rel} (e.g. spin-orbit splitting), and correlations effect ε_{corr} (e.g. plasmon excitation).

Experimentally the energy of the kinetic electrons E_{kin} is measured via a hemispheric analyzer (cf. **Figure 2.7**). It consists out of two electrically isolated, concentric hemispheres with an applied electric potential difference. The electrostatic field allows only electrons of a specific kinetic energy (pass energy) to get through the analyzer towards the detector, where the signal is recorded. Electrons with a higher kinetic energy (fast electrons) are neutralized at the outer hemisphere, whereas electron with a lower kinetic energy (slow electrons) are attracted to the inner hemisphere. Scanning of the kinetic energy is achieved by a retard plate with a negative potential, which slows down the emitted electrons to the pass energy.[33]

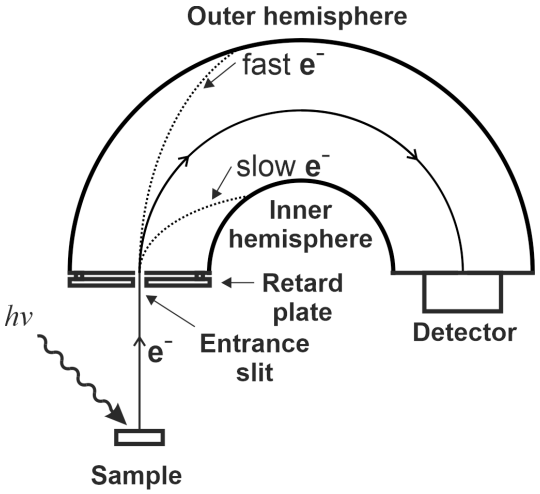

Figure 2.7: Schematic depiction of the electrostatic energy analyzer used in photoelectron spectroscopy, e.g. for the analysis of surfaces. Adapted from reference[33].

As an example the C 1s and O 1s XP spectra of polycarbonate are depicted in **Figure 2.8**. There are four carbon species and two oxygen species visible, which are assigned in **Figure 2.8**b). Especially the carbon atom (4) in the carbonate group (orange) stands out due to the large shift induced by the three surrounding oxygen atoms (initial state effect). Next to the carbonate species in **Figure 2.8**a) a final state effect (5) is visible due to a $\pi \rightarrow \pi^*$ excitation, a so-called "shake-up" event. This lowers the measured kinetic energy E_{kin} and as a result increases the observed binding energy E_{BE}.[44] A comparable typical energy loss event in solid crystals is the excitation of plasmons. The other carbon atoms in **Figure 2.8** are assigned to aromatic carbon atoms (1), aliphatic carbon atoms (2) and aromatic carbon atoms (3) next to an oxygen atom.

From the intensity ratio of the species, also the atomic ratio can be determined, e.g. 2:1 for the oxygen atoms in the carbonate group, marked in black and orange respectively.

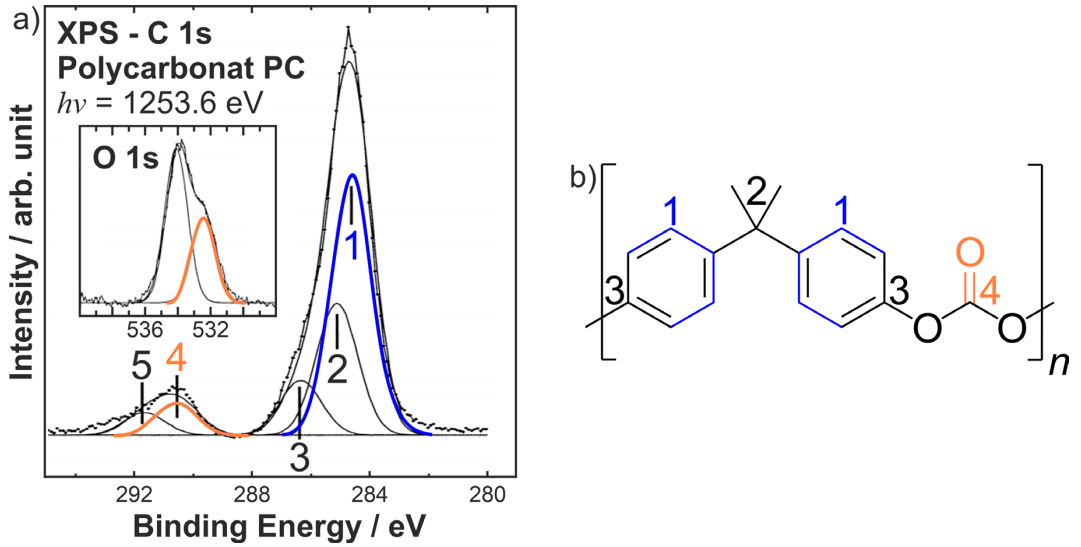

Figure 2.8: a) C 1s and O 1s XP spectra of polycarbonate. The deconvoluted peak are correlated with b) monomeric unit of polycarbonate PC. Adapted with permission from reference[44].

2.4.2 Near-Edge X-ray Adsorption Fine Structure - NEAXFS

Near-edge X-ray absorption fine structure NEXAFS and X-Ray Absorption Near Edge Structure XANES describe the same technique. However, it has become established that the former name is used in the soft X-ray regime ($h\nu$ < ca. 1.5 keV), whereas the latter is used in the hard X-ray regime ($h\nu$ > ca. 3 keV).

In NEXAFS an electron from a core hole is excited into empty states above the Fermi level (cf. **Figure 2.5**b). For excitation in NEXAFS the photon energy $E_{h\nu}$ is scanned by ~30-40 eV around an absorption edge (e.g., the Ce $M_{4,5}$ edge, which corresponds to the Ce 3d core level.). If the sample is a thin foil, the absorption could be directly quantified by the attenuation of the incoming and outgoing X-ray beam. However, for supported thin film samples like in the present thesis the absorption can be measured only indirectly by the decay of the excited electrons. The excited electrons can decay either non-radiant via the emission of an Auger electron into the continuum (cf. **Figure 2.5**c) or radiant via the emission of a photon (X-ray fluorescence). The intensity of the emitted primary Auger electrons is a direct measure of the X-ray absorption process.[45] In principle the created primary Auger electrons can be used for surface-sensitive measurements. However, in NEXAFS also bulk-sensitive measurements are possible by the so-called total electron yield (TEY) mode. In this mode, all electrons emitted from the sample are measured, dominated by the so-called "inelastic tail" of secondary electrons with a kinetic energy E_{kin} < 20 eV, which possess a large IMFP (cf. **Chapter 2.2**) and can escape from deeper layers of the bulk. The secondary electrons originate from cascade-like scattering of the primary Auger electrons.

NEXAFS can generate complex, informative absorption spectra, which make direct interpretation challenging as they are difficult to simulate.[46] Therefore, NEXAFS spectra

are often interpreted by utilizing references (cf. **Chapter 6.6.1**). A detailed description of the underlying processes in NEXAFS can be found in reference[39].

2.5 X-Ray Reflectivity - XRR

X-ray reflectivity XRR is used in the present thesis to determine the thickness *d* of the thin film. In XRR the sample is probed with an X-ray beam of the wavelength λ at small angles θ slightly above the angle for total external reflection. The incident angle α_i and the exit angle α_f with respect to the surface are kept equal $\alpha_i = \alpha_f = \theta$, so-called specular XRR. The intensity of the reflected X-ray beam is measured as a function of the angle θ. Typically, the decadic logarithm of the measured intensity is plotted against the modulus of the wavevector transfer $|q_z|$ perpendicular to the surface. The XRR geometry is depicted in **Figure 2.9**.

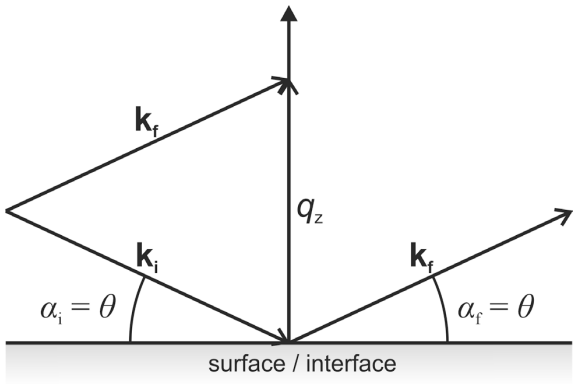

Figure 2.9: Principle of specular XRR: the incident α_i and exit angles α_f are symmetrically raised $\alpha_i = \alpha_f = \Theta$. Therefore, the reciprocal space perpendicular to the surface, along q_z is probed. Adapted from reference[47].

For q_z follows:

$$|q_z| = |k_0|\left[\sin(\alpha_f) + \sin(\alpha_i)\right] = \frac{4\pi}{\lambda}\sin\Theta \tag{2.3}$$

with $|k_0| = |k_f| = |k_i| = \frac{2\pi}{\lambda}$ being the (elastically conserved) wave vector modulus.[47] XRR measurements are sensitive to the electron density profile perpendicular to the surface in a range of ~0.1-100 nm and hence suited for the characterization of thin films.[47] For a thin film grown onto a dissimilar substrate, reflection can occur at the substrate/thin film layer interface and at the thin film layer/air interface. The reflected X-rays can interfere in a constructive and deconstructive manner which gives rise to oscillations in intensity during the measurement. From these so-called Kiessig fringes[48] the average thickness of the film can be determined via

$$d = \frac{2\pi}{\Delta|q_z|} \tag{2.4}$$

with $\Delta|q_z|$ being the the difference between two adjacent maxima (or minima) in intensity. For an extended description of XRR the reader is referred to references[40,47,49].

2.6 Low Energy Electron Diffraction - LEED

Low-energy electron diffraction (LEED) was firstly described by C. Davisson and L.H. Germer in 1927 on a nickel crystal surface. In 1937 C. Davisson was awarded the Nobel prize in Physics shared with G.P. Thomson for the experimental discovery of the diffractions of electrons by crystals and for the discovery of electron waves, respectively.

In principle, a coherent low-energy electron beam is diffracted from a periodically ordered (crystalline) surface. The energy of the low-energy electron used in the present thesis is typically between 40–300 eV. The wavelength of the electrons can be estimated from the modified de Broglie equation

$$\lambda = \sqrt{\frac{h^2}{2m_e E}} \tag{2.5}$$

to be around 1.93–0.70 Å, with wavelength λ, Planck constant h, energy of the electron E and its mass m_e. For comparison, the trilayer distance in $CeO_2(111)$ is ~1.56 Å. The wavelength of the electron is the same order of magnitude as the wavelength of interatomic distances which is why they can interact and may undergo diffraction if the atoms in the surface are arranged periodically (crystalline).

The electron beam can be described as wave front with the wave vector $\vec{k}_0 = \frac{2\pi}{\lambda}$ and each atom at the surface as scattering center. After elastic scattering each scattering center is source of a spherical wave, which can be approximated as a plane wave in the far field towards the detector. Due to constructive and destructive interference discrete maxima of the diffracted electron beams with the wave vector $\vec{k}_g$ can be observed on a fluorescence screen which acts as a detector. There are two conditions which need to be fulfilled to observe a diffraction maximum, which can be visualized with the Ewald sphere (cf. **Figure 2.10**):

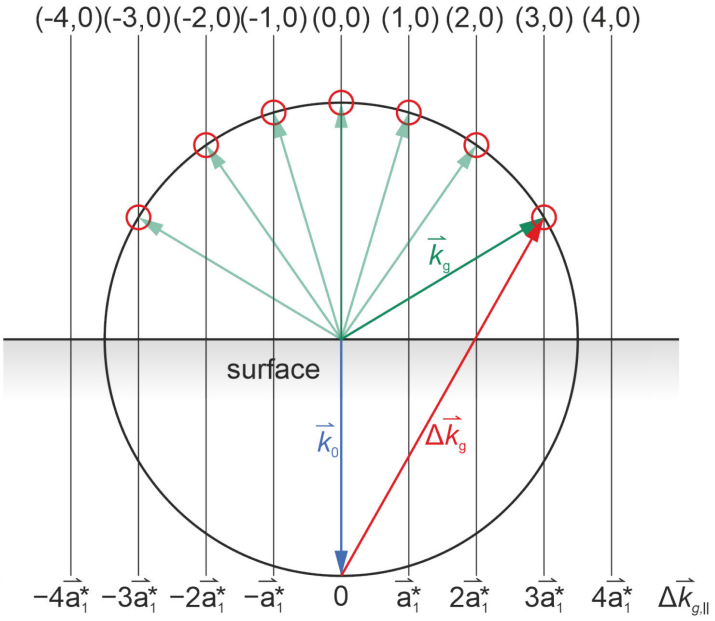

Figure 2.10: Two-dimensional Ewald sphere construction perpendicular to the surface for low-energy electron diffraction.

Energy conservation:

$$|\vec{k}_0| = |\vec{k}_g| \tag{2.6}$$

The magnitude of the incident wave vector of an electron $|\vec{k}_0|$ must be equal the magnitude of the wave vector of a scattered electron $|\vec{k}_g|$. In the Ewald sphere the energy conservation is depicted by a sphere (or in two dimensions, a circle) with the radius $|\vec{k}_0|$ at the origin of $\vec{k}_0$.

Momentum conservation:

$$\Delta\vec{k}_0 = \vec{k}_g - \vec{k}_0 = h\vec{a}_1^* + k\vec{a}_2^* + x\vec{a}_3^* = \vec{g} = (h,k); h,k \in \mathbb{Z}, x \in \mathbb{R} \tag{2.7}$$

Secondly, momentum conservation must be fulfilled: the momentum transfer $\Delta\vec{k}_g$ must be a multiple of the reciprocal lattice vector $\vec{g}$. In the Ewald construction $\vec{g}$ is depicted by rods which are integers of the vectors $\vec{a}_1^*$ and $\vec{a}_2^*$. In a figurative sense, a diffraction maximum is observed when the Ewald sphere intersects the so-called forest of rods.

In a LEED pattern the following information is contained: on the one hand, the two-dimensional periodicity of the surface unit cell can be derived from the arrangement of the reflections as well as the formation of superstructures (e.g. $(\sqrt{3} \times \sqrt{3})$R30°). On the other hand, the information of the geometry of the surface is contained in the intensity change of the reflexes, if several LEED images are considered with a variation in energy (LEED-IV, LEED fingerprinting).

2.7 Temperature Programmed Desorption - TPD

Another classical lab-based method for the investigation of (adsorbed molecules on) surfaces is temperature programmed desorption TPD, also termed thermal desorption spectroscopy TDS. The surface is investigated by applying a temperature ramp to the sample. As a response, the desorption rate of ions or molecules is probed with a mass spectrometer and the count rate/intensity is typically measured as a function of the temperature.[33] The temperature ramp can be described via

$$T(t) = T_0 + \beta t \tag{2.8}$$

with temperature T, time t, initial sample temperature T_0 and the constant heating rate β (typically between 1 and 100 K/s, in the present thesis 4 K/s). If an adsorbate A is adsorbed on a surface B, in a first approximation a desorption maximum at T_p corresponding to the maximum desorption rate of A is observed upon annealing, which is a convolution of two factors: as the temperature rises, thermal energy becomes available to break adsorbate-surface bonds and the desorption peak starts to evolve in an Arrhenius dependency: $k_d = A \exp\left(-\frac{E_d}{RT}\right)$, with the rate constant k_d, the activation energy E_d, the pre-exponential factor A (typically assumed $A \approx 10^{-13}$ s^{-1}) and the universal gas constant R. However, the desorption is limited by the amount of adsorbate on the surface, which decreases simultaneously. The observed desorption peak is shown as convolution of these factors in **Figure 2.11**.

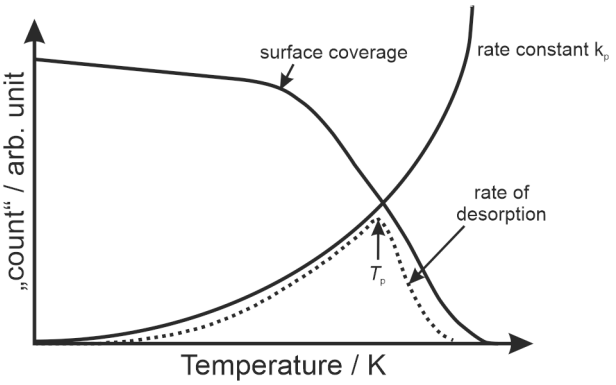

Figure 2.11: The dotted line indicates the rate of desorption as a convolution of, the changes in surface coverage and rate constant k_p, as a function of temperature T respectively. Adapted from reference[33].

In theory, from the desorption peak of an experimental series with increasing surface coverage the following information can be derived, i) activation energy for desorption, ii) lateral adatom interaction and iii) relative surface coverage.[33] In the present thesis, TPD is used qualitatively, i.e. to monitor the desorption temperature of HCl or H_2O, as coverage-dependent measurements for the investigated system are non-trivial (cf. **Chapter 7.1**, *TPD Results*). The description of coverage-dependent measurements and the determination of reaction order can be found in references[33,43].

2.8 Density Functional Theory - DFT

The model character of the investigated $CeO_{2-x}(111)$ thin film is well suited for complementary density-functional theory DFT calculations. These were performed in a collaboration by M. Veronica Ganduglia-Pirovano and Pablo G. Lustemberg.[1,2] The following section focuses on how the surface of the model catalyst can be modeled *in silico*. Additionally, the principle behind the energy diagrams shown in the present thesis is exemplified. An extensive description of DFT can be found in reference[50].

In general, DFT is a computational method to determine the ground state of the electronic structure of a system, e.g. atoms, molecules, but also complex systems like catalysts, by quantum mechanical modeling.[50] Instead of treating each electron in the system individually, in DFT the so-called electron density is used, which reduces a $3N$-dimensional problem, with N being the number of electrons in a system, i.e. $N = 666$ in **Figure 2.12**, to a three-dimensional one. The ground state-energy of a system is a unique functional of the electron density (first Kohn-Sham theorem). It is obtained by a recursive, iterative optimization process minimizing the total energy (second Kohn-Sham theorem).

Periodic boundary conditions (PBC) are a fundamental concept in density functional theory (DFT) used to model single crystalline periodic materials such as solid crystals. These conditions are essential as they enable the simulation of an infinite number of repetitions of the system in all directions of space. Under periodic boundary conditions, it is assumed that the system repeats infinitely in all directions, implying that the physical properties of the system are invariant under translations in the crystal lattice. This means that the properties of the system within a unit cell extend throughout the crystal periodically.

Practically the description of a surface, e.g. stoichiometric $CeO_2(111)$, is realized with a so-called three-dimensional slab−supercell approach[51] First, the system is described by a

defined supercell, e.g. the $(\sqrt{3} \times \sqrt{3})$R30°-$CeO_2$(111) supercell, which defines the vectors *a* and *b* depicted in **Figure 2.12**. The length of vector *c* is determined by the width of the surface and the vacuum region. These three vectors: *a*, *b* and *c* are the ones that repeat infinitely. It is crucial to include a vacuum region for precise surface simulations. The vacuum space must be chosen sufficiently large, so that the top of one slab does not interact with the bottom of the next slab.[50]

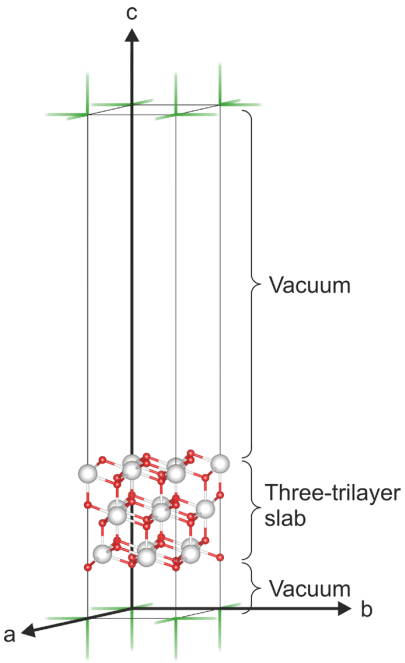

Figure 2.12: Exemplified supercell of CeO_2(111) ($(\sqrt{3} \times \sqrt{3})$R30° with three trilayer)[1] that defines the solid surface when the periodic boundary condition in applied all three directions (*a,b,c*) Adapted from reference[50].

The full power of DFT comes into effect by comparing the minimized total energies of two systems, i.e. an "investigated system" with a questioned quantity to a "reference system". It is essential that the number and sort of atoms in the compared systems are the same. In this manner binding energies, adsorption sites, or defect configurations etc. can be determined and compared to findings from other techniques (e.g. TPD, LEED).

For instance, the dissociative adsorption energy of one HCl molecule on the $(\sqrt{3} \times \sqrt{3})$R30° CeO_2(111) surface[31] ($CeO_2(111) + HCl_{gas} \rightarrow (H^*+Cl^*)_{ads}/CeO_2(111)$) can be calculated as

$$\underbrace{[E_{ads}(H^*+Cl^*)]}_{\text{adsorption energy}} = \underbrace{E[(H^*+Cl^*)_{ads}/CeO_2(111)]}_{\text{"investigated system"}} - \underbrace{E[CeO_2(111)] - E[HCl_{gas}]}_{\text{reference system}} \qquad (2.9)$$

$[E_{ads}(H^*+Cl^*)]$ is the dissociative adsorption energy of HCl on the CeO_2(111) surface to be determined. $E[(H^*+Cl^*)_{ads}/CeO_2(111)]$ is the total energy of an H atom and a Cl atom adsorbed on the CeO_2(111) surface (−225.76 eV), the "investigated system." $E[CeO_2(111)]$ and $E[HCl_{gas}]$ are the total energies of the pristine CeO_2(111) surface with

a ($\sqrt{3} \times \sqrt{3}$)R30° supercell (−218.59 eV, cf. **Figure 2.12**) and one HCl molecule in the gas phase (−6.08 eV), respectively, which form together the "reference system". In this manner [E_{ads}(H*+Cl*)] = −1.09 eV can be calculated, which predicts an exothermic adsorption of H*+Cl*, as observed experimentally[31] (cf. **Chapter 4.4**). In a corresponding energy diagram, the system of the pristine CeO_2(111) surface with HCl in the gas phase ("reference system") would be referenced to 0.0 eV, whereas the system with adsorbed H*+Cl* ("investigated system") would be referenced to −1.09 eV. The "investigated system" can be the "reference system" for another question, e.g. the formation energy for a defect.

In addition to its utility in identifying stable ground state configurations, DFT plays a crucial role in elucidating reaction mechanisms between chemical reactants and products. One employed technique for this purpose is the Nudged Elastic Band (NEB) method.[50] The NEB method offers the possibility to compute transition states and activation energies, which allows deeper insights into the kinetics of chemical reactions. This allows to predict reaction rates and identify rate-limiting steps. In this way reaction pathways can be investigated, thus complementing findings from an experiment.

3 Deacon Process

The Deacon process is the heterogeneously catalyzed oxidation of hydrogen chloride HCl with molecular oxygen O_2 to yield the desired product chlorine Cl_2, and water H_2O as a byproduct.

$$\overset{+I\ -I}{4\,HCl} + \overset{0}{O_2} \rightarrow \overset{0}{2\,Cl_2} + \overset{+I\ -II}{2\,H_2O} \quad \Delta_r H = -114\ \text{kJ/mol} \quad (1.1)$$

Originally, the motivation for the catalytic oxidation of HCl was the production of sodium sulfate ($2\,NaCl + H_2SO_4 \rightarrow Na_2SO_4 + 2\,HCl$) as an educt for the historic LeBlanc process ($Na_2SO_4 + CaCO_3 + 2\,C \rightarrow Na_2CO_3 + CaS + CO_2$) to obtain the basic chemical sodium carbonate Na_2CO_3, e.g. for soap or glass manufacturing. During the production of Na_2SO_4 HCl is released, which made the development of the Deacon process necessary as HCl is a toxic and corrosive gas. Nowadays, the historic LeBlanc process is replaced by the Solvay process, but the issue of HCl as a waste product persists (cf. **Chapter 1**). Conventionally, excess HCl is nowadays recycled in HCl electrolysis as neutralizing is unattractive.[7] By use of an oxygen-depolarized cathode[11] (Bayer-UhdeNora) the energy consumption could be lowered by 30% in comparison to the diaphragm electrolysis process.

An even more sustainable way to cope with this waste problem is to recover molecular chlorine from HCl by the Deacon process:[2] The energy consumption by the Deacon Process with RuO_2/TiO_2 is only 15% in contrast to optimized ODC electrolysis.[52] Additionally, instead of electricity as in electrolysis, heat is necessary, which is often abundant as reaction heat in manufacturing sites.[53] Another motivation for the recycling of chlorine is that the conventional production of via chlor-alkali electrolysis, is "one of the most energy-intensive and costly processes in the chemical industry".[7] Calculated for the year 2000, around 1% of the world electric energy 15.1 PWh[54] was converted in the chlor-alkali process: At that time the estimated production capacity was 45 Mt/a with an energy demand of 0.15 PWh.[55] Due to their toxicity, reactivity, and corrosivity, chlorine, HCl and chlorine-containing compounds like phosgene are commonly produced and used on the same site to minimize transport paths. Hence, a catalytic recycling on-site is desirable to enable a circular economy for chlorine. Also new developments for the safer storage of chlorine like the usage of trichlorides[4] $[Cl_3]^-$ would still make recycling of HCl necessary.

3.1 General Considerations

"In general, the Deacon reaction can be broken down into two separate processes."[2,10,12,56] Here, the simplified catalytic cycle for the original catalyst ($CuCl_2$/pumice) used by Henry Deacon and Ferdinand Hurter[13] is shown. First, HCl reacts with cupric oxide CuO to cupric chloride $CuCl_2$, during which water is formed as product. This chlorination process is exothermic:[10]

$$4\,HCl + 2\,CuO \rightarrow 2\,CuCl_2 + 2\,H_2O \quad \Delta_r H = -239{,}4\ \text{kJ/mol}^{10} \quad (3.1)$$

In the second step, the $CuCl_2$ reacts with molecular oxygen to recover CuO, thereby releasing the desired Cl_2 and closing the catalytic cycle. Within this endothermic process the chloride becomes oxidized to Cl_2, while the molecular oxygen is reduced.

$$2\ CuCl_2 + O_2 \rightarrow 2\ CuO + 2\ Cl_2 \qquad \Delta_r H = +125{,}5\ \text{kJ/mol}^{10} \quad (3.2)$$

In total the Deacon process is a slightly exothermic reaction $\Delta_r H = -114$ kJ/mol (**Equation 1.1**). From a thermodynamic point of view, a low reaction temperature is feasible to shift the equilibrium to the product side.[12] But "running the reaction at low temperatures, however, requires both very active and very stable catalyst materials."[53] Unfortunately, the Deacon process is a challenging reaction and the search for a suitable catalyst is subject of research for more than 150 years by now.[14,15]

The original catalyst, CuO dispersed on pumice, suffered from volatility of the formed $CuCl_2$ during the typical reaction temperature of 673-720 K, which lead to a loss of the active phase.[12] In the last century several other commercialized developments[55] like the Shell Process in the 1960s ($CuCl_2$-KCl on SiO_2, fluidized bed), the KEL-Chlorine process by Kellogg in the 1970s (nitrosylsulfuric acid $NOHSO_4$ in sulfuric acid), and the Mitsui MT process (Cr_2O_3 on SiO_2, fluidized bed) in the 1980s took place. Despite other attempts trying to optimize the original Cu-based catalyst[6,17] these catalyst showed either activity (low pass single conversion in the reactor), stability (active phase volatilization), environmental (e.g. Cr-based), or corrosivity issues.[7,55] Only in the late 1990s a stable and active catalyst was discovered by Sumitomo Chemical[9] based on RuO_2-covered rutile TiO_2, of which the reaction mechanism has been successfully elucidated.[57]

3.2 Deacon Process over RuO_2

A breakthrough at the end of the 20th century was the use of RuO_2 supported on rutile-TiO_2 by Sumitomo.[9,52,58] In the 2000s another similar RuO_2-based catalyst supported on cassiterite-SnO_2 was developed by Bayer.[7] An example of the successful implementation of a RuO_2-based catalyst, is the Deacon II plant of Covestro in Shanghai with an annual production capacity of 160 kt/a Cl_2, which started operation recently in 2021. A corresponding figure can be found in reference[59]. Here, 98% of the used HCl originate from the production of isocyanites for PU production (cf. **Figure 1.1**).[60] RuO_2/rutile-TiO_2 is a stable and active catalyst, typically running at temperatures of 620 K. The reaction mechanism of the HCl oxidation over the predominantly exposed (110) surface has been elucidated previously and is summarized in the following. An extended description can be found in references[12,57,61].

3.2.1 Reaction Mechanism

For the Deacon process over ruthenium(IV) oxide the RuO_2(110) surface is an appropriate model catalyst, as the (110) orientation is by far the most stable surface orientation, which is likely most prevailing on RuO_2 powders or e.g. rutile-type supported catalysts.[62] In the rutile structure (cf. **Figure 3.1**a) the Ru atom (blue) is bound to six oxygen atoms (green) forming a slightly distorted octahedron. The oxygen atoms in turn are surrounded by three ruthenium atoms in a planar sp^2-configuration. The bulk-truncated RuO_2(110) surface

exposes two kinds of undercoordinated atoms: oxygen in a bridge position (O_{br}, dark green) coordinated to only two Ru atoms underneath with one perpendicular dangling bond, and 1f-cus-Ru atoms (1f-cus: one-fold coordinatively unsaturated site, red), coordinated to only five oxygen atoms, i.e. with an oxygen atom missing in on-top position.[62] Under HCl oxidation conditions the O_{br} atoms are mostly replaced by chlorine atoms (Cl_{br}, gray). Hereby the surface is self-stabilized against further chemical reduction, explaining the stability of RuO_2 in the Deacon process.[62]

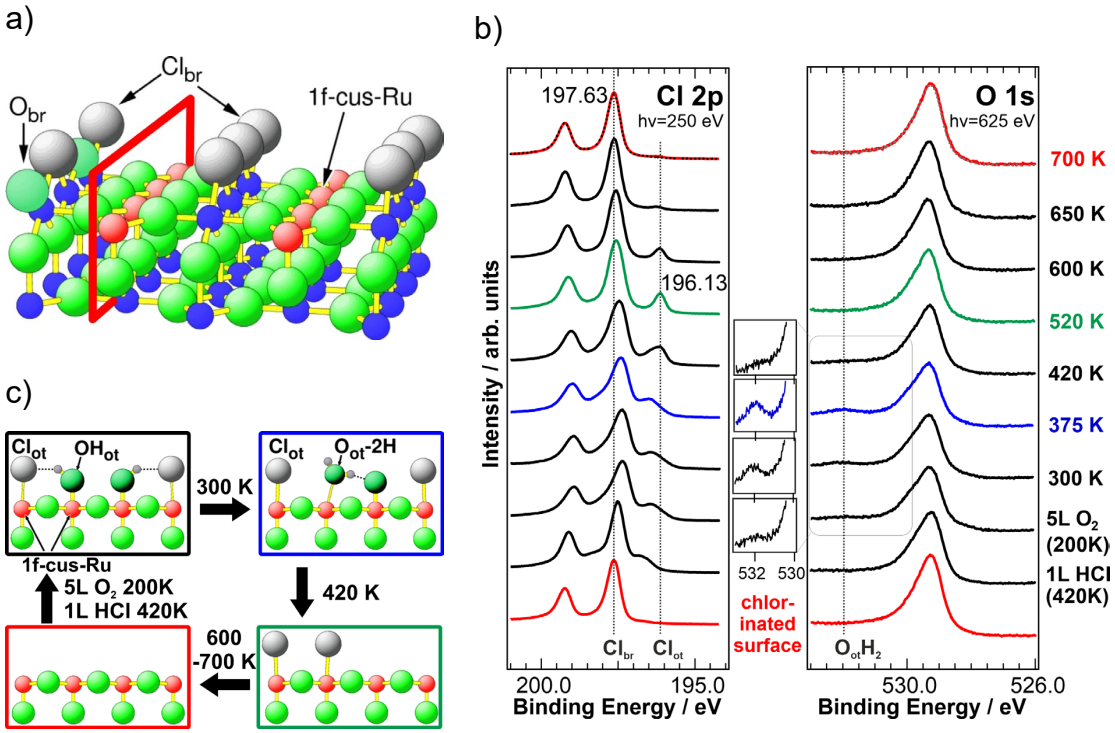

Figure 3.1: Reaction mechanism of the HCl oxidation (Deacon process) on $RuO_2(110)$: a) chlorinated $RuO_2(110)$ surface with Cl (gray) residing in bridge positions (Cl_{br}). In a first approximation the reaction is taking place along the one-fold coordinatively unsaturated site of Ru (1f-cus-Ru) highlighted with a red frame. b) Synchrotron-based XP spectra of Cl 2p and O 1s within *ex situ* measurements of the catalytic cycle, c) Depicted mechanism along the (1f-cus-Ru) rows. The color frames are associated with the corresponding XP spectra. Adapted with permission from reference[62].

In a first approximation the catalytic cycle takes place along the 1f-cus-Ru sites, highlighted in **Figure 3.1**a) with a red frame. This slice along the 1f-cus-Ru sites is the starting point for the catalytic cycle. In **Figure 3.1**b) the Cl 2p and O 1s spectra of the catalytic cycle are depicted. Upon HCl (1 L, 420 K) and O_2 (5L, 200 K) adsorption a shoulder becomes visible in the Cl 2p XP spectra assigned to Cl_{ot} forming a hydrogen bond to a neighboring HO_{ot} group (**Figure 3.1**c), black frame). After annealing to 375 K water $O_{ot}H_2$ forms on the surface (**Figure 3.1**c), blue frame). Upon subsequent annealing water is removed from the surface leaving only Cl_{ot} on the surface, identified by a transition of the shoulder into a sharp peak at 196.13 eV (**Figure 3.1**c), green frame). Further annealing up to 700 K leads to desorption of Cl_2 thereby restoring the starting point of the surface (**Figure 3.1**c), red frame). The reaction can be described as a quasi-one-dimensional Langmuir-Hinshelwood reaction along the 1f-cus-Ru sites. However, it was shown in kinetic Monte-Carlo KMC simulations that the OH groups can interact across the bridge rows, thereby influencing the kinetics. A detailed description can be found in a

publication and corresponding reviews[12,57,61]. Based on the mechanism it has been shown that the hydrogen transfer in water formation is the rate determining step.[57]

Although RuO_2 is a stable and active catalyst it faces several challenges: ruthenium Ru is a rare platinum group metal, with a low abundancy of $1 \cdot 10^{-3}$ mg/kg (cf. Au $4 \cdot 10^{-3}$ mg/kg or Pt $5 \cdot 10^{-3}$ mg/kg)[18] in the earth crust. The annual world production of 20-30 t per year as side product of copper, nickel, or platinum refinement, makes it susceptible toward high price fluctuations. Averaged per year, between 2016 and 2021 the price for Ruthenium fluctuated within $1,350 and $18,500 per kg.[63] Also, the construction and operation of the reactor is challenging as the Deacon process over RuO_2 is typically run under isothermal conditions. Another issue is the formation of local hotspots in the catalyst bed leading to the formation of volatile RuO_4 at elevated temperatures and thus loss of active catalyst material.

Therefore, the search for a suitable catalyst for the Deacon Process is still an ongoing research subject. There are several reports on stabilizing the original Cu-based catalyst, e.g. Cu-K-La/γ-Al_2O_3 by Feng et al.,[64] Cu-K-Sm/γ-Al_2O_3 by Sun et al.[65] or Cu/Ce composite oxide by Tang et al..[66] Amongst other developments, e.g. using Mn,[67] the Deacon reaction was investigated over $CuCrO_2$ (delafossite)[68], U_3O_8, or IrO_2.[17] The latter developments however bear concerns considering toxicity (i.e. Cr^{6+}) or price (Ir). A promising and viable alternative in terms of abundance, stability, and reasonable activity is cerium dioxide.[6]

4 Cerium Oxide CeO_{2-x}

Cerium Ce is a so-called “light rare-earth” element with the atomic number 58 in the group of the lanthanides, with a [Xe] $4f^1 5d^1 6s^2$ electron configuration. Despite the misleading name from times of its discovery in rare minerals, cerium is quite abundant with $6.65 \cdot 10^1$ mg/kg in the earth crust, which is comparable to copper Cu ($6.0 \cdot 10^1$ mg/kg) or zinc Zn ($7.0 \cdot 10^1$ mg/kg).[18] Upon air exposure it tarnishes quickly at the surface due to oxidation. Averaged per year, between 2016 and 2021 the price for the typical trading form ceria is within \$1.57 to \$2.15 per kg,[69] thus being only a fraction compared to Ru (cf. **Chapter 3.3.1**).

4.1 Cerium Oxide CeO_{2-x}

Cerium oxide CeO_{2-x} is a prototype of a reducible oxide[2,35,70,71] as Ce possesses two stable oxidation states: Ce(IV) and Ce(III). In the lab, cerium(IV) oxide CeO_2 appears as a colorless, yellowish solid whereas upon reduction towards cerium(III) oxide Ce_2O_3 the appearance changes depending on the degree of reduction towards a blue and finally black color. Key property of CeO_{2-x} and derived materials is the redox chemistry between Ce^{4+} and Ce^{3+} and the concomitant facile formation of oxygen vacancies V_O while maintaining structural integrity. At elevated temperature oxygen can be removed, e.g. as O_2, from the crystal lattice, thereby reducing four Ce^{4+} cations to Ce^{3+} and yielding two oxygen vacancies V_O. The process is reversible, hence under oxidizing conditions oxygen can be incorporated into the reduced lattice until all oxygen vacancies are “re-filled" and Ce^{3+} cations are oxidized to Ce^{4+}:

$$4\ Ce^{4+} + 2\ O^{2-} \rightleftharpoons 4\ Ce^{3+} + 2\ V_O + O_2 \qquad (4.1)$$

The reaction can also be expressed in Kröger-Vink notation by:[72]

$$4\ Ce_{Ce}^{\times} + 2\ O_o^{\times} \rightleftharpoons Ce_{Ce}^{'} + 2\ V_o^{\bullet\bullet} + O_2 \qquad (4.2)$$

This property is often referred to as the oxygen storage capacity OSC. Key example for the utilization of the OSC in catalysis is the application of CeO_{2-x} as a supporting carrier material for the actual active component (e.g. Pt or Pd) in catalytic converters of combustion engines. Under “rich” exhaust conditions oxygen is removed from CeO_{2-x}, while under “lean” conditions oxygen in incorporated. Apart from broad application in catalysis, e.g. in the water-gas shift reaction, water splitting, steam reforming, or in solid oxide fuel cells, ceria is often used as a polishing agent.[17,70] Recently, it has caught attention for the Deacon process where it can serve as viable catalyst without any additional active component.[16]

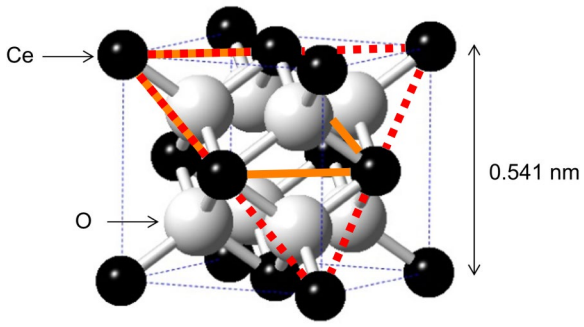

Figure 4.1: Cubic *fcc*-unit cell of cerium dioxide CeO_2. Cerium cations are depicted in black and oxygen anions in gray, respectively, drawn with an ionic radius of 50%. The red dashed triangle indicates the (111) surface plane and the orange rhombus the corresponding surface unit cell (cf. **Figure 4.2**). Adapted with permission form reference[35].

The fully oxidized cerium(IV) oxide CeO_2 crystalizes in the fluorite structure derived from CaF_2, with the space group *Fm3m*. The cerium cations are arranged in a face-centered cubic *fcc*-unit cell (**Figure 4.1**, black), where all tetrahedral sides are occupied by oxygen anions (**Figure 4.1**, gray). The arrangement of the oxygen anions can be described as a simple cubic arrangement embedded inside the *fcc* unit cell. As result, every cerium cation is coordinated by eight equivalent nearest neighboring oxygen anions, whereas each oxygen anion is tetrahedrally coordinated by four cerium cations. The lattice constant of the *fcc*-unit cell is $a = 0.541134(12)$ nm.[35,73] The fully reduced cerium(III) sesquioxide a-Ce_2O_3 (A-type) crystallizes in a hexagonal structure.[35] Between these two limits the structure of CeO_{2-x} with $(0 \leq x < 0.5)$ can be described based on the fluorite lattice of fully oxidized CeO_2. Upon reduction Ce retains near *fcc*-like positions[35] and depending on x and the temperature the oxygen vacancies are either randomly distributed, or form ordered structures, e.g. *ι*-Ce_7O_{12} (rhombohedral iota-phase). A detailed description of the phase diagram can be found in a review by Adachi et al.[74] A limiting structure for fluorite-based cubic c-Ce_2O_3 (C-type) is bixbyite (Mn_2O_3), space group *Ia3*. Here, the Ce cations are coordinated to six O anions and the unit cell consists of 32 Ce atoms and 48 O atoms (cf. **Figure 4.5**). In the present thesis the reduction degree x was kept between $(0 \leq x < 0.4)$ in order to prevent a transition[75] from cubic c-Ce_2O_3 (C-type) to hexagonal a-Ce_2O_3 (A-type). During reduction from Ce^{4+} to Ce^{3+} the ionic radius increases from $r_{Ce(IV)} = 0.097$ nm to $r_{Ce(III)} = 0.114$ nm. For comparison, the ionic radii of oxygen O^{2-} and chloride are $r_O = 0.138$ nm and $r_{Cl} = 0.181$ nm, respectively.[76]

4.2 Deacon Process over CeO_{2-x}

The Deacon process over ceria has been investigated in several studies under real catalysis conditions, setting the boundary conditions for model studies and complementary DFT calculations. The first studies mentioning CeO_2[77,78] or Ce-containing compounds[79] as potential catalyst materials for the Deacon process can be found in the patent literature, while the first scientific investigation was published by Amrute et al..[16,80] They showed that CeO_2 powder samples are stable over a wide range of process parameters. Bulk chlorination is not observed in O_2-rich feeds ($HCl:O_2 \geq 4:3$) whereas under stoichiometric or sub-stochiometric feeds ($HCl:O_2 \leq 4:1$) the bulk is chlorinated. The formed $CeCl_3 \cdot 6\ H_2O$

(as revealed by X-ray diffraction XRD) is inactive but stable with respect to volatilization. Original activity levels can be restored upon re-exposure to O_2-rich feeds.[16] In a follow up study, Farra et al. investigated the chlorination and reoxidation/reactivation *operando* with prompt-gamma activation analysis (PGAA)[81] and corroborated the previous findings. Interestingly, they found that high oxygen over-stoichiometries can regenerate the active surface while chlorine is still present in the subsurface. Furthermore, they investigated cerium oxychloride CeOCl and found it to be unstable in the HCl oxidation, as in an O_2-rich feed CeO_2 is formed.[82] In another study they found that oxygen exhibits a positive reaction order in the Deacon process.[83]

There are several approaches reported in the literature to improve the performance of ceria-based catalysts. One approach is the usage of dopants: e.g. Hf- and Zr-doped catalysts revealed an increased activity, while trivalent dopants were found to be detrimental[17,22,24]. Another possibility is the use of a supporting material. Here, CeO_2/ZrO_2[19,84–86] is a suitable candidate, which was already tested in a pilot plant.[19] Also for CeO_2/ZrO_2 systems a re-activation of the catalyst in oxygen after deactivation under "harsh" conditions ($HCl:O_2 = 3:1$) is observed.[25] The Deacon process over ceria-based catalysts runs typically at a "high" temperature of 700 K under adiabatic conditions, which simplifies the reactor design. This makes it also suitable for a combination with the conventional RuO_2 catalyst at 620 K in a reactor cascade**,** decreasing the investment cost by more than half.[6]

Although the Deacon process over ceria is promising and the activity and stability could be improved by doping or the use of supports, the reaction mechanism is still elusive (cf. **Chapter 5**). Here, a detailed understanding on the same level of the reaction mechanism over RuO_2 (cf. **Chapter 3.3**) is the aim. Model studies were conducted on a variety of systems, like polycrystalline samples with a specific morphology, e.g. fibers,[20] porous samples,[87] or shape-controlled particles exposing a preferred facet orientation.[21,71] While the previous model systems can be investigated under real catalytic conditions, i.e. ambient pressures, single-crystalline thin film systems under UHV conditions[28,31] bear the advantage of comparably low structural complexity and high purity, which makes it possible to elucidate the microscopic processes involved in the HCl oxidation over CeO_2 surfaces.[1] Furthermore, a direct comparison with computational modeling, e.g. DFT calculations is possible. First model studies for the HCl oxidation over CeO_{2-x}(111)/Ru(0001) thin films were conducted by Christian Sack[28] and formed the basis for the present work.

4.3 CeO_{2-x}(111) Surface

In surface science or model catalysis often low-index faces are investigated to ensure structurally controlled conditions (cf. **Chapter 2.1**). In case of CeO_2 the (111), (110), and (100) surfaces are the most discussed in literature. The stability of these three surfaces is in the order (111) > (110) > (100).[35] The surface investigated the most in the literature and also in the present thesis is the (111) surface due to its stability and because it is most likely to be exposed in real powder samples.[88] For model studies under ambient pressure conditions it is also possible to prepare nano powders via hydrothermal synthesis,

exposing the (100) surface in form of cubes, the (111) surface in form of octahedra, and the (110) surface in the form of rods, while the latter can show faceting to (111).[21,71]

4.3.1 Stoichiometric CeO_2(111)

The CeO_2 (111) surface can be derived from the cubic unit cell of stoichiometric CeO_2, by constructing a plane which intercepts all three axes in the unit cell dimension (cf. **Figure 4.1**, red dashes). The extended (111) surface is depicted in **Figure 4.2**, with the (1 × 1) surface unit cell depicted in orange.

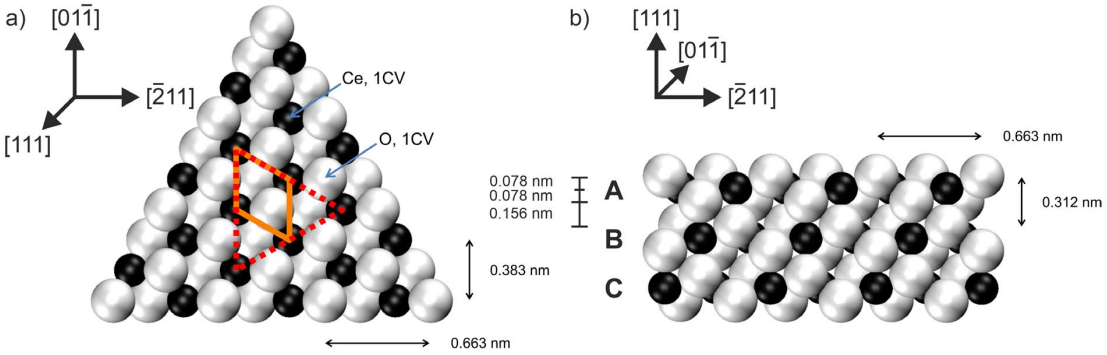

Figure 4.2: a) Schematic top view of the stoichiometric CeO_2(111) surface, with the (1 × 1) surface unit cell in orange. b) Side view along the (01$\bar{1}$) direction of the CeO_2(111) surface showing the ABC stacking of the O-Ce-O trilayer. Cerium cations depicted in black and oxygen anions in gray. Adapted with permission from reference[35].

The CeO_2(111) surface can be described by O-Ce-O trilayers, where a layer of cerium atoms is wrapped between two layers of oxygen atoms. In the topmost trilayer the oxygen atoms are called surface and subsurface oxygen atoms, respectively. The cerium atoms and the surface oxygens atoms are exposing one dangling bond each. The distance between two cerium respectively two oxygen atoms is $a_{\parallel}$ = 0.3826 nm, corresponding to the lattice constant of the (1 × 1) surface unit cell. One O-Ce-O trilayer has a thickness of 0.156 nm which also corresponds to the distance between two O-Ce-O layers, resulting in a step height of 0.312 nm. Three O-Ce-O trilayers are stacked in an ABC order, leading to a lattice constant of $a_{\perp}$ = 0.936 nm normal to the surface (**Figure 4.2**b). The CeO_2(111) surface can be categorized as a Tasker Type 2 surface,[89] that means it has no net dipole moment perpendicular to the surface, although each O-Ce-O trilayer is intrinsically charged.[35]

Experimentally there are several ways to prepare the CeO_2(111) surface.[35]For instance, a polished single crystal can be used.[90] However, due to the low electronic conductivity of stoichiometric CeO_2 techniques like LEED or scanning tunneling microscopy STM are challenging. An alternative approach is the preparation of ceria thin films supported on an electronically conductive substrate, which was also employed in the present thesis. Thin films can be prepared in multiple ways, for example by the deposition of Ce-containing organic or inorganic precursors, e.g. metal-organic chemical vapor deposition MOCVD,[35] direct deposition from a CeO_2 target, e.g. pulsed laser deposition PLD,[91] molecular beam epitaxy MBE,[92] or, most commonly via oxidation of evaporated Ce metal,

physical vapor deposition PVD. For an extended overview the reader is referred to a review by Mullins et al..[35] In the present thesis the $CeO_2(111)$ surface is prepared via PVD, which is an UHV-compatible technique allowing for the preparation of confined homogeneous thin films. Typically, $CeO_2(111)$ thin films are prepared on *hcp*(0001) or *fcc*(111) single crystal metal surfaces, e.g. Pd(111),[93] Pt(111),[94,95] Ni(111),[27] Rh(111),[96] Ru(0001),[97] Au(111),[98] or Cu(111).[99] The growth of cerium oxide on Ru(0001) was thoroughly studied by the research group of Flege et al.[100,101] Islands are initially formed as equilateral triangles, which corresponds to a Volmer-Weber growth. Closed films can be prepared via deposition of Ce at comparably low temperatures of 700 K in oxygen (in situ oxidation, **Figure 4.3**a) followed by a post-oxidation ranging from ~1000 K[97] to 1450 K,[28] with higher temperatures improving crystallinity. Closed thin films are reported for a film thickness of 5-6 O-Ce-O trilayers,[28,97] and yet expose domain boundaries (**Figure 4.3**c) and defects (**Figure 4.3**d).

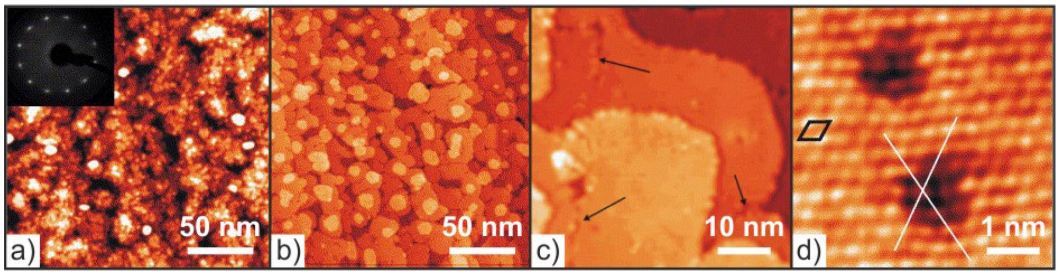

Figure 4.3: Scanning tunneling microscopy STM images from Lu et al. of a 6 O-Ce-O trilayer $CeO_2(111)$ thin film a) as grown at 700 K in $p(O_2) = 10^{-7}$ mbar (in situ oxidation), b) after annealing to 980 K in $p(O_2) = 4 \cdot 10^{-7}$ mbar (post-oxidation). c) Domain boundaries (arrows) on terraces. d) Atomically resolved surface with the unit cell indicated in black. The bright protrusions are assigned to the Ce atoms. In addition, defects are visible as lowered areas. Adapted with permission from reference[97].

The surface lattice constant of $CeO_2(111)$ $a_{\parallel} = 0.3826$ nm has a mismatch ratio with that of Ru(0001) $a_{\parallel} = 0.2704$ nm of 1.41. However, it could be shown that the (111) thin film shows a good comparability towards bulk $CeO_2(111)$.[27,28,75] In addition, Siegel et al.[91] prepared a 300 nm thick bulk-like $CeO_2(111)$ film on Yttria-stabilized zirconia YSZ(111). The LEED-IV analysis indicated a good comparability to the investigated 5-8 nm thick thin film systems on Ru(0001).[28] The LEED-IV studies[28,91] revealed that the topmost surface oxygen layer is expanded by 6-8 pm with respect to the underlying cerium layer, while the cerium layer is contracted by 2-4 pm with respect to the underlying subsurface oxygen layer. (cf. **Figure 4.2**b)

4.3.2 Reduced $CeO_{2-x}(111)$

A key property of $CeO_{2-x}(111)$ is the redox chemistry of Ce^{4+} and Ce^{3+} accompanied by the formation of oxygen vacancies V_O. Hence, in model catalysis the reduced $CeO_{2-x}(111)$ surfaces are of particular interest. The restructuring of $CeO_{2-x}(111)$ upon reduction is already quite complex itself: depending on the degree of reduction x, with $0 < x < 0.5$, $CeO_{2-x}(111)$ thin films stabilize a variety of ordered reconstructions with well-defined oxygen vacancy V_O concentrations. In literature, several reconstructions of the pristine $CeO_{2-x}(111)$ surface are reported, e.g. $(\sqrt{7} \times \sqrt{7})R19.1°$, $(\sqrt{7} \times 3)R19.1°$, $(\sqrt{3} \times \sqrt{3})R30°$, (3×3), (4×4) (C-type Ce_2O_3), and a-(1×1). [75,90,102–105] These surfaces,

in particular the location of V_O, were studied with non-contact atomic force microscopy NC-AFM and complementary DFT+U calculations by Olbrich et al. (cf. **Figure 4.4**).[90,106] Previously the ($\sqrt{7} \times \sqrt{7}$)R19.1°, (3 × 3), and (4 × 4) were prepared by Duchoň et al. on Cu(111) (cf. **Figure 4.4**)[103] and Ru(0001)[104] and studied by means of LEED and XPS. With XPS the reduction degree x was determined to be ($\sqrt{7} \times \sqrt{7}$)R19.1°: 70% ($x \approx 0.35$), (3 × 3): 50% ($x \approx 0.25$), and (4 × 4): 5% ($x \approx 0.03$). In **Figure 4.4** the LEED patterns, corresponding NC-AFM images, and DFT+U structures are shown. In addition, the crystal structures of C-type Ce_2O_3 (cf. 4 × 4) and Ce_7O_{12} (cf. ($\sqrt{7} \times \sqrt{7}$)R19.1°) were refined with neutron diffraction data by Kümmele et al..[107] These findings were used in the DFT+U optimization by Olbrich et al..[90]

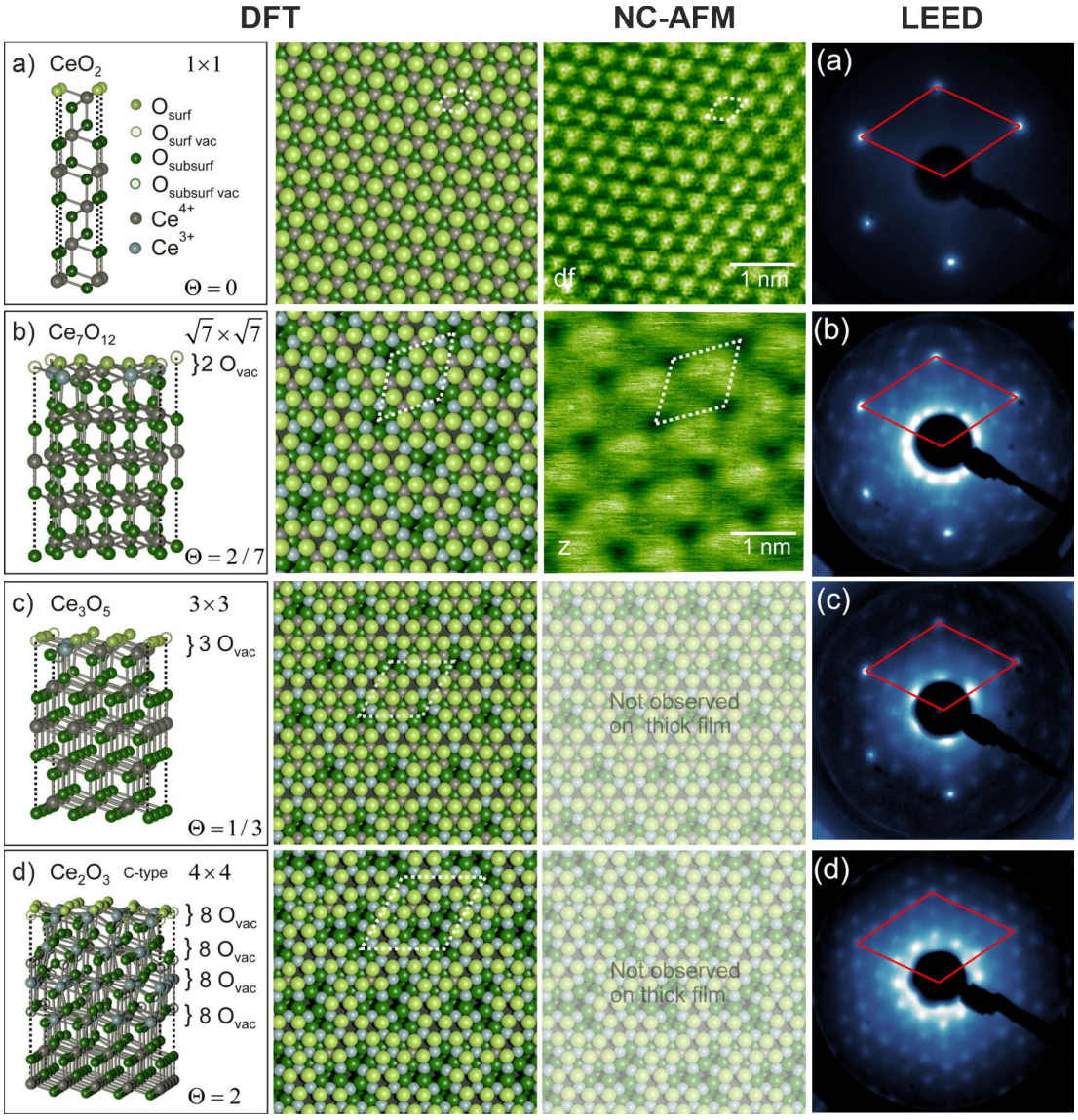

Figure 4.4: Comparison of the a) stoichiometric CeO_2(111) surface and the reduced CeO_{2-x}(111) surfaces exposing several reconstructions b) ($\sqrt{7} \times \sqrt{7}$)R19.1°, c) (3 × 3), and d) (4 × 4). These were investigated by Olbrich et al. with DFT+U calculations and NC-AFM measurements and by Duchoň et al. with LEED and XPS. Adapted with permission from references[90,103].

Experimentally the CeO_{2-x}(111) film can be reduced by several methods:[28,35] thermal heating under UHV conditions,[75,95] dosing of a reducing agent (e.g. methanol),[108] or soft sputtering with a low acceleration voltage and kinetic energy.[109] A reproducible way

developed by Stetsovych et al.[102] and used by Duchoň et al.[103] is the deposition of metallic cerium onto a preformed CeO_2(111) thin film at room temperature. Upon annealing to 700-900 K the topmost cerium metal film is re-oxidized by the underlying CeO_2 (cf. **Figure 4.5**a+b). Depending on the amount of metallic Ce and the thickness of the underlying CeO_2 film, the reduction degree at the CeO_{2-x}(111) surface can be adjusted between $0 < x < 0.5$. (cf. **Chapter 6**). In the same publication Duchoň et al. described that the degree of reduction *x* of the film is not homogeneous perpendicular to the surface. Instead, a gradient is formed with a higher degree of reduction respectively a higher concentration of oxygen vacancy towards the surface (cf. **Figure 4.5**c). Upon reduction an increase in the surface lattice constant of +3.5% was determined via LEED, in agreement with experiments on bulk samples.[73] Due to the reconstruction depending on the degree of reduction *x*, the LEED pattern can also be used for an estimation of the degree of reduction of the surface after cross-calibration with XPS.

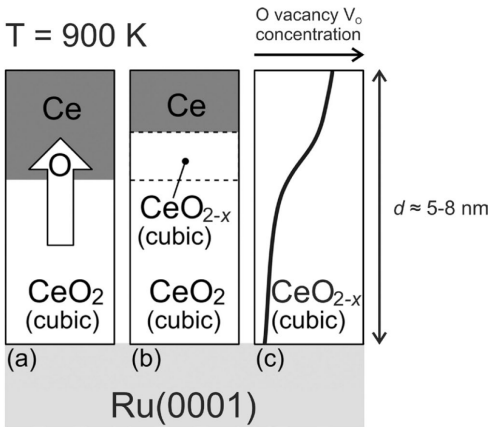

Figure 4.5: Preparation of reduced CeO_{2-x}(111) thin films by deposition of Ce metal on CeO_2(111) at room temperature. a) Upon annealing to 900 K the Ce metal becomes b) oxidized by the underlying CeO_2. c) After a final annealing step, a gradient in the degree of reduction *x* respectively the oxygen vacancy V_O concentration is observed. Adapted with permission from reference[103].

4.4 Interaction of HCl with Stoichiometric CeO_2(111)

The interaction of HCl with the stoichiometric CeO_2(111)/Ru(0001) surface was investigated previously in a combined experiment (XPS, LEED, STM, TPD) and theory (DFT+U) approach.[31] It was found via LEED that a $(\sqrt{3} \times \sqrt{3})$R30° superstructure is formed at room temperature upon exposure of HCl (**Figure 4.6**a), which could also be observed and calculated with STM measurements and DFT+U calculations, respectively (**Figure 4.6**b).

Complementary DFT+U calculations showed that HCl adsorbs in a dissociative acid-base reaction forming a Cl_{top} species on top of a cerium atom, while hydrogen binds to a neighboring surface oxygen site forming a hydroxyl group. The adsorption energy is calculated to be −1.15 eV (cf. **Chapter 2.8**) with an additional acid-base stabilization of ~0.4 eV. The calculated adsorption energy is in broad agreement with the experimentally determined value of -0.89 ± 0.15 eV in surface coverage-dependent TPD measurements.

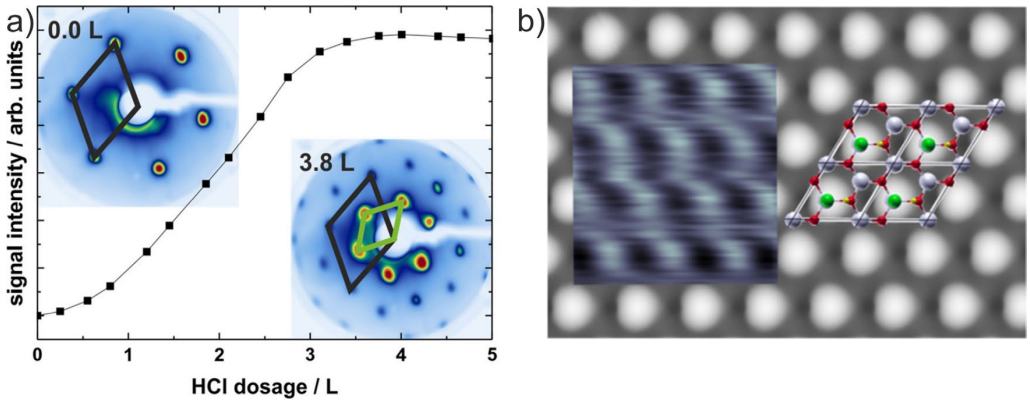

Figure 4.6: a) LEED patterns (49 eV) before and after exposure of 3.8 L HCl to $CeO_2(111)$ at 300 K. The (1 × 1) unit cell is shown in black and the $(\sqrt{3} \times \sqrt{3})$R30°-H+Cl unit cell in green. The graph shows the integrated intensity of the (2/3, 2/3) superstructure diffraction spot as a function of HCl exposure.[31] b) DFT simulations of empty-state STM images (0−1.8 eV) of the (3 3) 30 × R ° − Cl + H surface compared to a small section of an atomically resolved STM image of the $CeO_2(111)$ $(\sqrt{3} \times \sqrt{3})$R30°-H+Cl structure after exposing the $CeO_2(111)$ surface to 5 L of HCl at 300 K. The calculated structure is superimposed where H and Cl species and the outermost O and Ce ions are depicted as yellow, green, red, and gray spheres, respectively. Adapted with permission from reference[28].

The Cl_{ot} species is mobile as it possesses a low activation barrier for hopping between two cerium atoms of ~0.6 eV, which agrees with the $(\sqrt{3} \times \sqrt{3})$R30°-H+Cl superstructure formation at room temperature. In contrast, hydrogen is practically immobile on $CeO_2(111)$ at room temperature with a binding energy of 1.8 eV.[110] Upon annealing to 800 K solely HCl and neither water nor hydrogen are detected in TPD. This finding could be explained with complementary DFT+U calculations of the energy profile (**Figure 4.7**c) showing that HCl recombination and desorption is favored over Cl-Cl association and Cl_2 desorption.

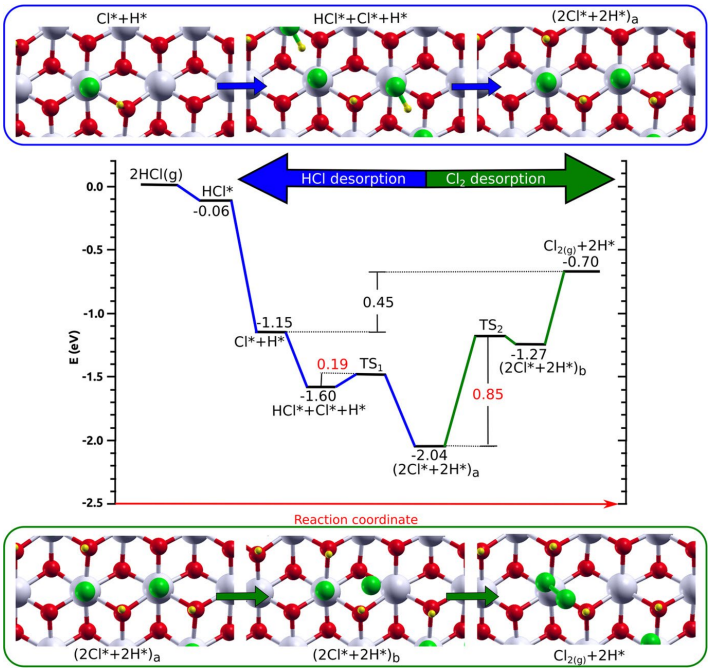

Figure 4.7: "Energy profile for HCl interaction on the stoichiometric $CeO_2(111)$ surface. The two paths for Cl* removal from the surface are shown in blue for the Cl* association with H* (HCl desorption) and in green for association with Cl* (Cl_2 desorption). The involved surface structures are depicted as top views of ball and stick model (green: Cl, gray: Ce, red: O, yellow: H)" Adapted with permission from reference[31].

In the context of the stoichiometric $CeO_2(111)$ surface an additional experiment addressing the influence of oxygen on the $(\sqrt{3} \times \sqrt{3})$R30°-H+Cl superstructure is depicted.

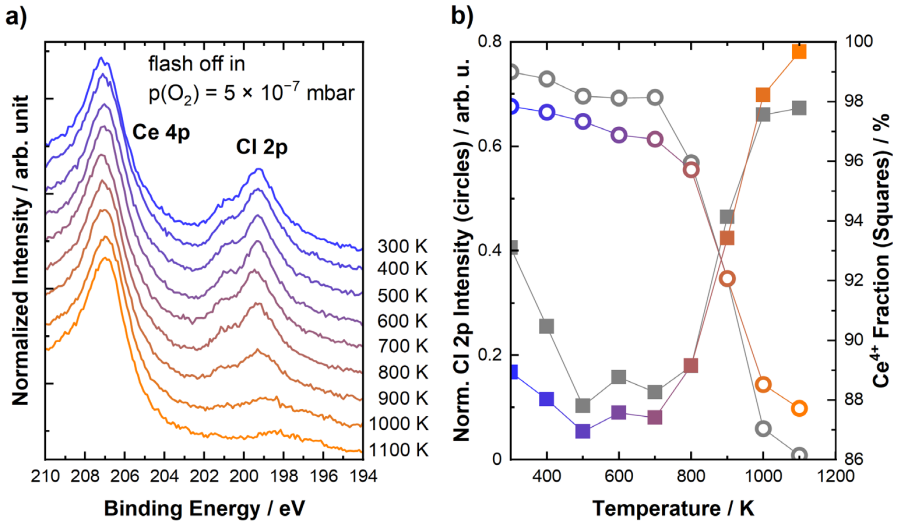

Figure 4.8: a) Cl 2p lab-based XP spectra of a $(\sqrt{3} \times \sqrt{3})$R30°-H+Cl superstructure as a function of temperature upon stepwise annealing in oxygen $p(O_2) = 5 \times 10^{-7}$ mbar. b) normalized Cl2p intensity (circles) and Ce^{4+} fraction (squares) determined from Ce 3d spectra as a function of temperature. In gray, the corresponding annealing experiment[31] under ultra-high vacuum conditions is shown. Unpublished data by Christian Sack.

In the presence of an oxygen atmosphere $p(O_2) = 5 \times 10^{-7}$ mbar the $(\sqrt{3} \times \sqrt{3})$R30°-H+Cl superstructure was stepwise annealed while the Cl 2p and the Ce 3d XP spectra were measured *in situ between each* annealing step (**Figure 4.8**a). From the quantification of the data (**Figure 4.8**b) it can be seen, that in comparison to annealing under UHV-conditions the Cl 2p intensity and the Ce^{4+} fraction follow the same trend.

Hence, it was concluded that the stoichiometric surface is inactive in the Deacon process, and a Langmuir-Hinshelwood reaction mechanism at the surface is likely to be excluded. The stoichiometric surface being non active is also in agreement with the proposed reaction mechanism in literature, where the surface is defective and exposes oxygen vacancies.

5 Keynote: Proposed Reaction Mechanism over Defective $CeO_2(111)$

Amrute et al. proposed a reaction pathway for the HCl oxidation over defective single crystalline $CeO_2(111)$, based on experiments on ceria powder-catalysts.[16,111] The energies of the reaction intermediates were predicted using density functional theory (DFT) calculations (cf. **Chapter 2.8**).[2] In this chapter preliminary considerations are carried out based on the proposed reaction pathway, where open questions reside and how these can be investigated utilizing dedicated model experiments.

5.1 Proposed Reaction Mechanism

The proposed reaction pathway is depicted in **Figure 5.1**. For each step the in the calculation the corresponding molecules in the gas phase (cf. **Chapter 2.8**) are depicted, on the left for the educt side, i.e. HCl and ½ O_2, and on the right for the product side, i.e. H_2O and Cl_2.

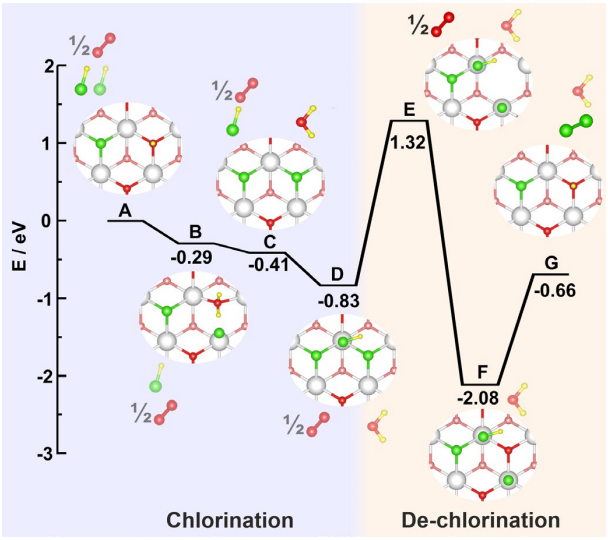

Figure 5.1: Proposed reaction pathway for the HCl oxidation over the single-crystalline $CeO_2(111)$ surface (top view), re-arranged and based on Amrute et al..[16] Only the outermost O–Ce–O trilayer is depicted. For each step the educts and products in the gas phase are depicted on the left and right, respectively. Color code: Ce^{4+} cations are white spheres, the O surface (subsurface) atoms are red (light red), Cl atoms are green, and H atoms are yellow. Adapted with permission from references[2,16].

The catalytically active phase was modelled with the chlorinated $CeO_2(111)$-(2 × 2) surface, where chlorine resides in an oxygen vacancy position (Cl_{vac}) and one surface lattice O site is occupied by hydrogen forming a hydroxyl OH group (**A**). The catalytic cycle[16] starts with the dissociative adsorption of one HCl (acid-base reaction), where chlorine resides in a Ce on-top position (Cl_{top}) and the H atom is transferred to the OH surface group (**B**). The Cl_{top} species displaces the formed H_2O molecule and fills the nascent surface oxygen vacancy ($V_{O,S}$), thus becoming a second Cl_{vac}, while water desorbs at a typical reaction temperature of 700 K (**C**). A second HCl molecule dissociates on the surface and forms a Cl_{top} species (**D**). The most critical but also innovative step in the proposed

reaction pathway is the displacement of Cl_{vac} to an on-top position Cl_{top}, a reaction step that is endothermic by +2.15 eV (**E**). The activation of Cl_{vac} leaves an oxygen vacancy behind that is filled by dissociative adsorption of ½ O_2 from the gas phase, a process that is exothermic by −3.4 eV (**F**). Last, the two Cl_{top} species recombine, leading to the desired product Cl_2 and closing the catalytic cycle (**G**).[2] In general, the proposed mechanism can be categorized as a Mars-van Krevelen mechanism,[16,21,86,111,112] where oxygen atoms are removed from the lattice (here as water **C**) and the formed vacancy V_O is refilled by oxygen from the gas phase (**F**).

5.2 Thought Experiment: Chemical Looping in Model Catalysis

In a thought experiment the separation of the Deacon process into an exothermic chlorination process and an endothermic oxidative de-chlorination process (cf. **Chapter 3.2**) can be transferred to the proposed mechanism as followed: The first steps (**A**, **B**, **C**, **D**) can be summarized as "chlorination" of the surface (light blue background, $\Delta_r H = -0.83$ eV), while the latter steps (**E**, **F**, **G**) of the reaction path in **Figure 5.1** can be considered as oxidative "de-chlorination" (light orange background, $\Delta_r H = +0.17$ eV).[2] During chlorination (light blue background), oxygen acts as a "spectator species" in the gas phase, while during oxidative de-chlorination (light orange background) water act as a "spectator species." The overall calculated reaction enthalpy $\Delta_r H = -63{,}7$ kJ/mol is in reasonable agreement with the reported value in **Chapter 3.1** ($\Delta_r H = -114$ kJ/mol), taking into account that in the proposed reaction mechanism only ½ O_2 is considered.[10]

Chlorination:

(**A**) 2 HCl + $CeO_{2-x}Cl_{vac}$-OH → (**D**) CeO_{2-x}-2 Cl_{vac}-HCl_{ads} + H_2O $\Delta_r H = -0.83$ eV

De-chlorination:

(**D**) CeO_{2-x}-2 $Cl_{vac,2}$-HCl_{ads} + ½ O_2 → (**G**) $CeO_{2-x}Cl_{vac}$-OH + Cl_2 $\Delta_r H = +0.17$ eV

Overall reaction:

(**A**) 2 HCl +½ O_2 → (**G**) Cl_2+ H_2O $\Delta_r H = -0.66$ eV ($\Delta_r H = -63{,}7$ kJ/mol)

In order to transfer the thought experiment to dedicated model catalyst experiments the concept of chemical looping is utilized,[29,113] which is used in technical reactor design. A chemical looping reactor consists out of two stages or reactors with a fluidized bed, between which the catalyst is cycled and acts as a carrier. An advantage of chemical looping is that "chemical equilibrium limitations can be overcome".[29] Transferred to the Deacon process a simplified chemical looping reactor is illustrated in **Figure 5.2**.

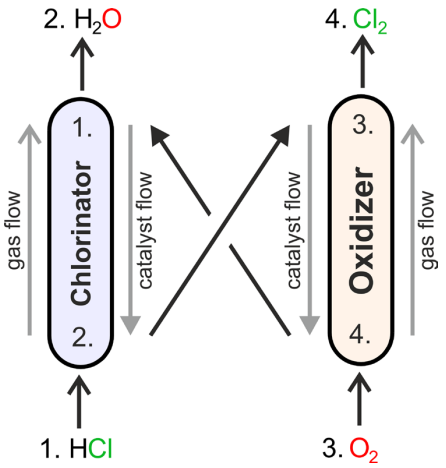

Figure 5.2: Schematic depiction of a simplified two-stage cyclic fluidized bed reactor used in the thought experiment for chemical looping in the Deacon process. Adapted from references[30,58].

The cycle starts at (**1.**), where the catalyst runs in counterflow through the "chlorinator" and is exposed to the HCl feed. At a typical process temperature of 700 K, the catalyst is chlorinated and water H_2O (**2.**) forms. Subsequently, the now chlorinated catalyst is transferred to the "oxidizer" where the chlorinated surface is exposed to the oxygen feed (**3.**) in counterflow upon which the desired chlorine (**4.**) forms. This chemical looping "two-stage cyclic fluidized bed process" concept has been realized for the Deacon process,[30,114] although not reaching "commercial viability"[58] due to corrosion issues.[7] Additionally, the idea was developed further by Han et al..[7,115] It shall be noted that under real conditions[30,115] the operation of a reactor *in operando* is dynamic[116] and more complex than the exemplary depiction in **Figure 5.2**. For example, the gas inlet of O_2 and HCl can be varied at each fluidized bed and be adjusted to the operation conditions.[30,58] For an extended description it is referred to the original publication from Mortensen et al.[30] Nevertheless, this conceptual separation forms the basis for dedicated model studies in order to answer open questions regarding the reaction mechanism. The chlorination and de-chlorination of the CeO_{2-x}(111) surface can be investigated separately under well controlled chemical and structural conditions:

5.2.1 Chlorination

The reaction mechanism is proposed for a "defective stoichiometric CeO_2(111) surface".[16] Previous experiments showed that the fully oxidized surface is inactive (cf. **Chapter 4.4**), and that cerium is far more reduced[21,81] under real conditions. This raises the question how HCl interacts with reduced CeO_{2-x}(111) surfaces of different degrees of reduction. Furthermore, in the reaction mechanism two chlorine species Cl, one in a Ce on top position Cl_{top} (e.g. **Figure 5.1**, B) and one in an oxygen vacancy Cl_{vac} (e.g. **Figure 5.1**, C) are proposed.[16,117–120] While the former has been described on the stoichiometric surface[31] (cf. **Chapter 4.4**), the latter needs to be identified experimentally. Finally, the question arises, if the product water H_2O can be observed during chlorination and if its formation is dependent on the degree of reduction x. Quite a few of the experiments and results of the "chlorination" have been published previously in a shared publication and were conducted during the doctoral thesis of Christian Sack.[28] In this work they are embedded and cited in the context of the chemical looping experiment and

complemented by additional DFT calculations and synchrotron- as well as lab-based experiments.

5.2.2 De-Chlorination

During de-chlorination the proposed reaction pathway in **Figure 5.1** remains elusive in two critical points: First, the activation step $Cl_{vac} \rightarrow Cl_{top}$ is highly endothermic (cf. **Figure 5.1**, E) and therefore would only be possible, if it can be coupled with the exothermic adsorption process of ½ O_2 gas. The second point concerns the replenishment of a surface oxygen vacancy by ½ O_2 gas (cf. **Figure 5.1**, F), which is not an elementary step. Instead, a full O_2 gas molecule (cf. **Equation 1.1**) has to be adsorbed.[2] How is this possible on the chlorinated surface and where does then the other half of the O_2 molecule remain on the surface?[2] Finally the question arises if chlorine formation can be observed? Overall, the questions can be summarized as experimental investigation of the present proposed reaction mechanism and if a possible bottleneck can be identified. The experiments and results of the "de-chlorination" have been published previously.[2]

6 Experimental Setup

In the following section the experimental setup and equipment to investigate the previously discussed "chlorination" and "de-chlorination" over dedicated CeO_{2-x}(111) model catalyst thin films in the Deacon process is described. Following the equipment, the preparation of the CeO_{2-x}(111)/Ru(0001) is explained. Finally, it is shown how the degree of reduction x of the CeO_{2-x}(111) thin film is determined via XPS and NEXAFS in a linear combination approach. The thickness of the films is determined by XRR.

6.1 FlexPES Beamline - EA01 End Station

The Surface and Materials Science SMS branch (EA01 end station) of the FlexPES beamline[41] at the 1.5 GeV storage ring of MAX IV can be divided into three chambers (cf. **Figure 6.1**): first, the experimental chamber with the incoming beam (beam in) from the storage ring and the detectors for XPS (DA30-L(W)) and NEXAFS (MCP detector). Second, the main preparation chamber above the experimental chamber, with a vertical automatized manipulator (VACGEN Omniax) for sample adjustment in and between the upper main preparation chamber and the lower experimental chamber. Third, a secondary preparation chamber is located next to the main preparation chamber with an additional vertical automatized manipulator (PREVAC). The cerium electron beam evaporator of the Over research group (EFM 3, Focus GmbH) is mounted in a horizontal position on the secondary preparation chamber, to ensure a comparable sample-evaporator distance (cf. **Chapter 6.5**). Basis for sample manipulation are flag-type sample holders. Samples can be loaded into the main preparation chamber via a load-lock attached to the main chamber and can be stored within two sample garages.

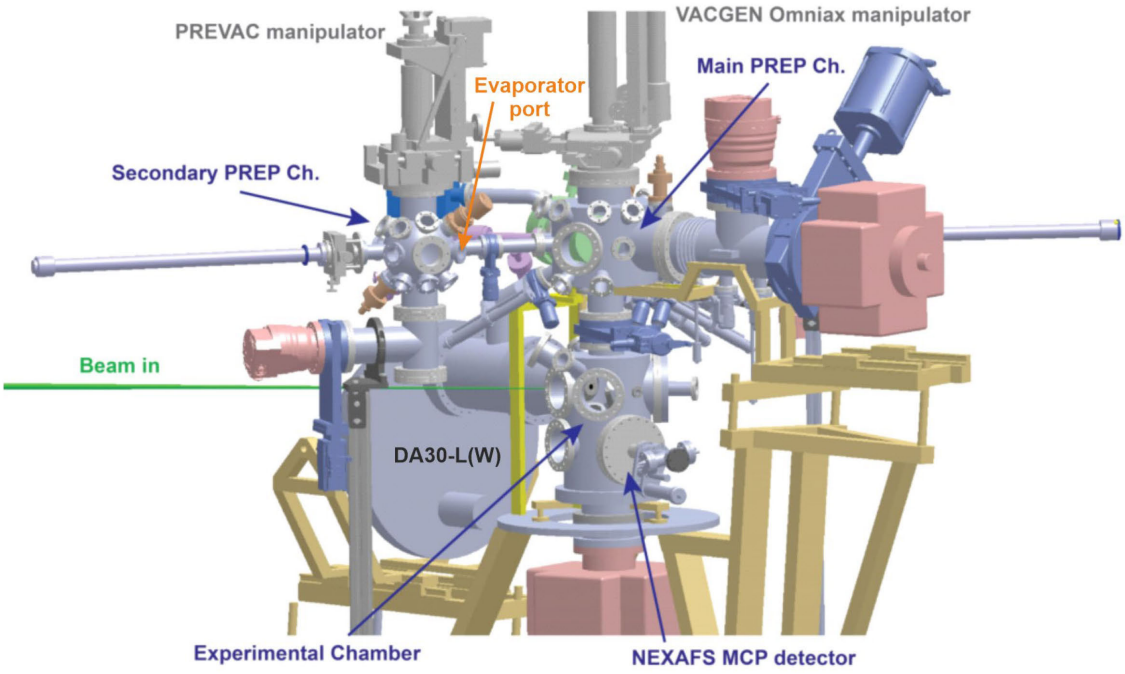

Figure 6.1: Side view of the EA01 end station at the Surface & Material Science branch of the FlexPES beamline, located at the 1.5 GeV storage ring of MAX IV in Lund, Sweden. Adapted from reference[121].

On the manipulator the sample is heated via a tungsten filament behind the sample holder. For higher temperatures ($T >$ ca. 1000 K) the heating mode can be switched to electron beam heating. Cooling of the sample is achieved by compressed air (optional: liquid N_2) passing through the manipulator. Temperature measurement is achieved by a K-type thermocouple spot-welded to the side of the sample and connected to the manipulator with flexible contact springs. Oxygen is dosed through a manifold attached to a main preparation chamber and can be dosed in the experimental chamber up to pressures of $p(O_2)= 5 \cdot 10^{-8}$ mbar. In the main preparation chamber larger oxygen doses (> 30 L) can be applied in a reasonable amount of time ($t \leq 360$ s) with pressures up to $p(O_2) = 5\ 10^{-6}$ mbar. HCl (Air Liquide, 2.8) is stored in a custom-made 10 ml cylinder on a separated manifold attached behind a mounting port of the main chamber. Hydrogen chloride is dosed in the main preparation chamber as well with pressures up to $5 \cdot 10^{-8}$ mbar via the background pressure, to protect the chamber from corrosion. These pressure requirements exclude *operando* measurements and the data for XPS and NEXAFS are acquired in the experimental chamber *in situ*.

XP spectra of Ce 4d, Cl 2p, and O 1s are measured at two photon energies, (Ce 4d: $h\nu$ = 250 eV/850 eV; Cl 2p: $h\nu$ = 250 eV/850 eV; O 1s: $h\nu$ = 580 eV/ 1180 eV) which allow for probing near-surface and bulk-like properties. Bulk-like properties are probed by photoelectrons with kinetic energy of E_{kin} = 650 eV, while near-surface properties are probed by photoelectron of E_{kin} = 50–130 eV kinetic energy, close to the minimum of the universal curve of inelastic mean free path of electrons (cf. **Chapter 2.2**).[122] The energy of the Ce 4d is chosen to be $h\nu$ = 250 eV as a compromise between achieving high surface sensitivity and avoiding the Cooper minimum[123] at $h\nu$ = 175 eV[124] with its low cross-section.[2] XP spectra of Ce 4d are used instead of Ce 3d to have sufficient flux at higher kinetic energies of E_{kin} = 650 eV. The slit-width of the beam is set to 50 µm and the pass energy E_{pass} of the detector is set to E_{pass} = 50 eV, except for Cl 2p ($h\nu$ = 250 eV, E_{pass} = 10 eV) and O 1s ($h\nu$ = 580 eV, E_{pass} = 20 eV). The spectra are calibrated via the Fermi level E_F of gold foil mounted next to the sample. From the Ce 4d spectra at $h\nu$ = 250 eV the near-surface fraction of Ce^{3+}/Ce^{4+} and therefore the near-surface reduction degree x (Ce^{3+} fraction) can be determined (cf. **Chapter 6.5.4**).[2] NEXAFS data of the Ce $M_{4,5}$ edge (Ce 3d) are recorded in total electron yield (TEY) mode. Here the signal is dominated by low energy electrons with $E_{kin} \lesssim 20$ eV, the so-called "inelastic tail".[39] As the average escape depth of these photoelectrons is larger[122] (cf. **Chapter 2.2**) than the thickness of the CeO_{2-x}(111) film, the Ce^{3+}/Ce^{4+} fraction of the bulk and therefore the bulk reduction degree x (Ce^{3+} fraction) can be determined.[2] The combination of XPS and NEXAFS allows for disentangling surface form bulk properties of the CeO_{2-x}(111) thin film. Beam-induced damages of the studied layers are not encountered, as routinely checked during the synchrotron beamtime (cf. **Chapter 2.3**). Additionally, the defocused synchrotron beam spot[2] 1 mm × 0.4 mm is moved between each measuring point over the homogeneous sample.[2]

6.2 XPS Chamber

XP spectra can be acquired in the lab of the Justus-Liebig-University JLU in a dedicated UHV system[31] as well. Here, a non-monochromatic Al/Mg dual anode X-ray source

(Omnivac) with an operating photon energy of 1253.6 eV (Mg Kα) and a Leybold EA 200 analyzer are used. As complementary method the chamber is equipped with a qualitative LEED system (Specs ErLEED 1000-A). CeO_{2-x}(111) thin films on Ru(0001) can be prepared with the cerium electron beam evaporator (EFM 3, Focus GmbH) mounted in an upward-pointing angle of ~45°. The Ru(0001) is mounted via clamped w-shaped tungsten wires to the manipulator of the chamber. Temperature control up to T = 1450 K is achieved by a K-type thermocouple spot-welded to the back of the sample. In addition to O_2 (Linde, 5.0) and Ar (Linde, 5.0), atomic oxygen O can be dosed via a thermal cracker (Oxford Applied Research: TC50 – Universal Thermal Cracker, cf. **Chapter 6.4.2**).

HCl (Air Liquide, 2.8) and Cl_2 (Linde, 5.0) can be dosed in a shutter-separated "mounting cell", which is pumped individually. Furthermore, the cell can be opened to move the manipulator out of the chamber for mounting the sample. In addition, the electron beam evaporator can be attached at the mounting port of the cell in a vertical, straight position for melting down fresh cerium in the crucible (cf. **Chapter 6.5.1**). A detailed description of the UHV system can be found in reference[125].

6.3 LEED Chamber

A second UHV system[126,127] at the JLU is equipped with LEED, using a video-LEED (Specs ErLEED 1000-A) system, and TPD. As mass spectrometer a high sensitivity ion-counting system (Hiden Analytical HAL 301/3F) is used. The cerium electron beam evaporator (EMF 3, Focus GmbH) is mounted in a horizontal position. Before mounting on the LEED chamber, the cerium was molten in the XPS chamber in a straight position to prevent cerium from segregation out of the crucible.

The sample is spot-welded with w-shaped tungsten wires to the tantalum bars of the manipulator. Temperature control from T = 110 K (liquid N_2) up to T = 1550 K is achieved by a K-type thermocouple. A detailed description of the UHV system can be found in reference.[28]

6.4 Specific Instruments

The following two instruments are essential for the preparation of the cerium sample as well as for the generation of atomic oxygen O.

6.4.1 Cerium Evaporator

The cerium oxide thin films in the present thesis are prepared via physical vapor deposition. Key tool for the deposition of cerium is an electron beam evaporator (EFM 3, Focus GmbH, **Figure 6.2**). In the core of the evaporator a hollow cooling shroud (a) (copper) resides which is cooled with water (b) inside the walls. In the center of the cylinder a crucible (c) or rod can be placed from behind with an high-voltage (HV) insulated feedthrough (d). Electron beam heating is achieved with a filament (e) residing at the end of the copper cylinder around the opening. In front of the latter a flux monitor (f) and a shutter (g) are placed for control of the evaporation process. Not shown is the combined quadripolar feedthrough for the filament (e) and thermocouple attached to the cooling shroud.

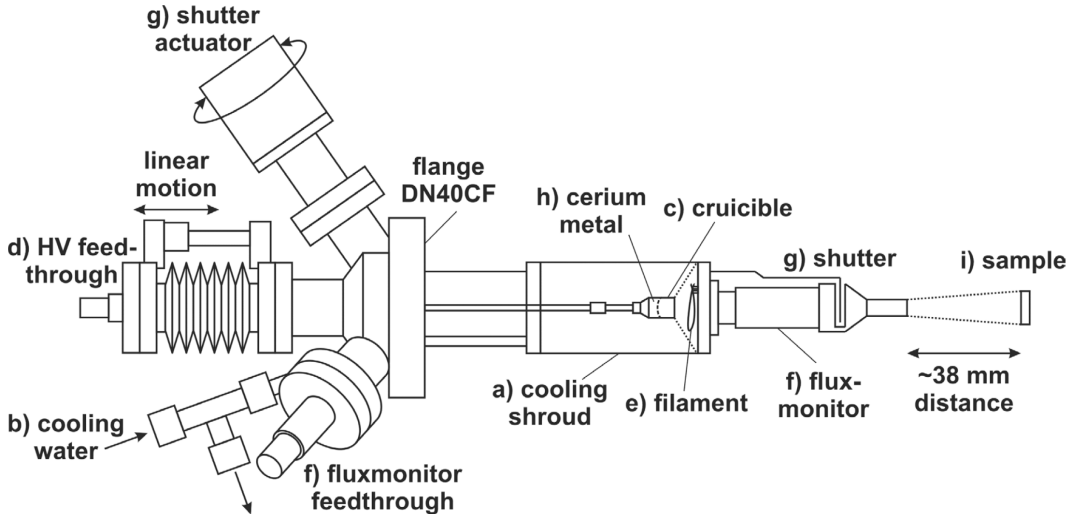

Figure 6.2: Semitechnical drawing of the used evaporator for physical vapor deposition (EFM 3, Focus GmbH). Adapted from reference[128].

For the evaporation of cerium (h), a molybdenum crucible (8 mm diameter, capacity of 250 mm³) is used, as cerium becomes liquid under evaporation conditions (melting point T_{Ce} = 1068 K). Prior to first usage the empty Mo crucible needs to be degassed under UHV conditions via electron beam heating, until upon further increasing the heating power does not increase the pressure anymore and, in addition, $p < 1 \cdot 10^{-10}$ mbar and the flux remains close to zero. Afterwards the crucible is filled with a stripe of cerium metal (ca. (6 × 6 × 1) mm³, ca. 25 mg, HMW Hauner GmbH, 99.9%). The stripe needs to be cleaned in a nonpolar, aprotic solvent[28] (e.g. *n*-heptane or *n*-hexane) as cerium metal is stored under protective paraffin oil due to its reactivity (cf. lithium or sodium). Rough oil and other residuals can be removed with a clean spatula.

A common issue observed during the evaporation is segregation of cerium out of the crucible. In order to ensure a homogeneous, reproducible thin film preparation at all three UHV systems initially the cerium is melted down in a vertical straight position in the "mounting" cell at the XPS chamber (cf. **Chapter 6.2**). The process can be followed through a window. Another measure to ensure comparable preparation between the three used UHV systems is that the evaporator sample (i) distance, is kept at an optimized value of ~38 mm, adjusted via the *z*-drive. After each mounting of the evaporator the melted down cerium needs to be degassed again. Over time cerium segregates out of the crucible and the filling process needs to be repeated. For the evaporation of cerium at the EA01 end station (Surface and Material Science branch) at the FlexPES beamline[41] at MAX IV in Lund, Sweden the evaporator with the crucible containing the molten in cerium was transported under protective Ar gas.

6.4.2 Thermal Oxygen Cracker

For the generation of atomic oxygen O an Oxford Research Systems TC-50 thermal cracker is employed at the XPS chamber. Similarly to the electron beam evaporator an iridium capillary is annealed via electron beam heating to temperatures up to 1250 K.[129] By a leak valve O_2 (Linde, 5.0) can be dosed through the heated capillary into the UHV chamber. The chemical bond of oxygen is cracked thermally, generating reactive atomic

oxygen. However, when passing the capillary not all molecules are cracked. The amount of dosed atomic oxygen can be determined via the parental loss method:[129] a specific pressure, e.g. $p(O_2) = 1 \cdot 10^{-8}$ mbar, is adjusted with the leak valve of the cracker, while the capillary is not heated. Simultaneously the pressure is monitored via a mass spectrometer (MS) at the specific mass/charge ratio (m/z) of oxygen ($m/z = 32$). Given the assumption that atomic species react directly with any surface inside the chamber the cracking efficiency C.E. can be calculated[129] from the MS signal when the capillary is non heated (m/z_{32}^{off}) and heated (m/z_{32}^{on}) via

$$C.E. = \frac{(m/z_{32}^{off} - m/z_{32}^{on}) \cdot 100}{m/z_{32}^{off}} \tag{6.1}$$

Due to the reactivity of the atomic oxygen, the sample needs to be positioned directly in front of the capillary during dosing.

6.5 Preparation of the CeO_{2-x}(111)/Ru(0001) Thin Film Model System

In the following section the preparation of the stoichiometric and reduced CeO_{2-x}(111) thin films used in the present thesis is described, followed by a brief characterization.

6.5.1 Stoichiometric CeO_2(111)/Ru(0001) Thin Films

Starting point for all experiments shown are CeO_2(111) thin films grown onto disk-shaped Ru(0001) single crystals (MaTecK GmbH, ⌀ 7 or 8 mm) via physical vapor deposition (PVD). Cerium (Goodfellow, 99.9%; HMW Hauner GmbH, 99.9%) is deposited from a well-outgassed electron beam evaporator (EFM 3, Focus GmbH, $U = 800$ V, $P = 40–50$ W, Flux = 2.0 µA, deposition time $t_{dep} = 50–120$ min).[2] *In situ* oxidation is achieved with a background O_2 atmosphere of $p(O_2) = 5 \cdot 10^{-8}$ mbar at a temperature of $T = 700$ K during evaporation. For post-oxidation the sample is annealed to $T = 1000$ K in $p(O_2) = 10^{-6}$ mbar for 15 min. A quick annealing step by flashing to $T = 1200$ K and subsequent cooling to room temperature in O_2 is added to improve the crystallinity of the CeO_2(111) film (cf. **Figure 4.3**).[28] Higher flashing temperatures are avoided in order to prevent cracking of the film. After deposition the LEED pattern is counterchecked for Ru(0001) substrate-related diffraction spots. If needed the deposition time t_{dep} is adjusted, and the oxidation steps are repeated. The preparation process is adapted from that of Mullins et al.[27] and Hasegawa et al.[26] Similar preparation procedures were reported in the literature.[75,94,97,100,102,130,131]

For the experiments at the EA01 (Surface and Material Science branch) at the FlexPES beamline[41] at MAX IV in Lund, Sweden two stoichiometric CeO_2(111)-Ru(0001) thin film samples were prepared in the XPS and the LEED chamber at the JLU. After transfer to the main preparation chamber of the EA01 end station the post-oxidation step (annealing for $t = 15$ min in $p(O_2) = 10^{-6}$ mbar at $T = 1000$ K, followed by flashing to $T = 1200$ K) is repeated to remove adventitious carbon contamination[36,37] from the atmosphere during sample transfer.

For re-preparation of the $CeO_2(111)$ thin film in the home lab, the Ru single crystal is cleaned with two consecutive sputter (T = room temperature, t = 30 min, $p(Ar) = 10^{-5}$ mbar, U = 1.5 keV, I_{em} = 18 mA) and annealing (T = 1300 K, t = 5 min, $p(O_2) = 10^{-6}$ mbar) cycles. The purity of the clean Ru(0001)-(2×1)O or Ru(0001)-(2×2)O surface is checked via the LEED pattern and XPS measurements.

6.5.2 Reduced $CeO_{2-x}(111)$/Ru(0001) Thin Films

Upon reduction of the $CeO_{2-x}(111)$ thin film the surface reveals several well-ordered reconstructions, e.g. $(\sqrt{7} \times \sqrt{7})R19.1°$, (3 × 3), and (4 × 4) depending on the reduction degree x ranging from $x = 0$ ($CeO_2(111)$) to $x = 0.5$ (fully reduced $Ce_2O_3(111)$) (cf. **Chapter 4.3.2**). The reduced $CeO_{2-x}(111)$ films are prepared by evaporation of Ce metal under UHV conditions at room temperature onto the stoichiometric $CeO_2(111)$ thin film. The formation of the reconstructions depends on the previous deposition time t_{dep} and the thickness of the underlying $CeO_2(111)$ film. In the present thesis the following dependencies were found: $t_{(\sqrt{7} \times \sqrt{7})R19.1} \approx 0.1 \cdot t_{dep}$, $t_{(3 \times 3)} \approx 0.18 \cdot t_{dep}$ and $t_{(4 \times 4)} \approx 0.29 \cdot t_{dep}$. After deposition the sample is annealed to T = 900 K for t = 15 min, and finally flashed to T = 1100 K under UHV conditions.[102–104,131]

6.6 Characterization of the $CeO_{2-x}(111)$/Ru(0001) Thin Film Model System

The preparation and characterization of $CeO_{2-x}(111)$ thin films has been described previously in the doctoral thesis of Christian Sack[28] and in the literature.[35,103] The preparation of $CeO_{2-x}(111)$ thin films on Ru(0001) was established in the Over research group within the doctoral thesis of Christian Sack.[28] The pristine film was investigated with STM, LEED, and XPS. It was shown by LEED that the crystallinity of the film could be improved upon annealing to temperatures above 1200 K to 1300K-1400 K. In STM it was observed that the terrace width increases from ~20 nm (1000 K) to ~50 nm at 1400 K. The thickness of the films was determined by the damping of the Ru 3d signal to ~23 O-Ce-O trilayers (71 Å). LEED-IV analysis of the pristine film was in good agreement with findings from Siegel et al. (cf. **Chapter 4.3.1**)

6.6.1 Determination of Film Thickness

The thickness d of the $CeO_{2-x}(111)$/Ru(0001) thin film is determined via XRR (PANalytical X'Pert PRO MRD, Cu K_α). In **Figure 6.3** the measurements of two samples are shown. The orange line shows the XRR measurement of the stoichiometric $CeO_2(111)$ film. From the minima and maxima in intensity (Kiessig fringes, cf. **Chapter 2.5**) the average thickness can be determined to d_{ox} = 5.7 nm, which corresponds to 18 O–Ce–O trilayers.[1] The blue line shows the measurement of the reduced and subsequently re-oxidized sample after the beamtime. Under the assumption that the re-oxidized film has the same thickness as the previously reduced film, a value of d_{reox} = 7.5 nm or 24 O−Ce−O trilayers (cf. **Figure 6.3**) is determined. The determined thickness agrees well with the previously[28] measured one, where the film thickness was determined by the dampening of the Ru 3d signal of the supporting Ru(0001) single crystal. Compared to XPS, XRR

has the advantage that the thickness is determined directly. A disadvantage is, however, that the measurement is *ex situ*.

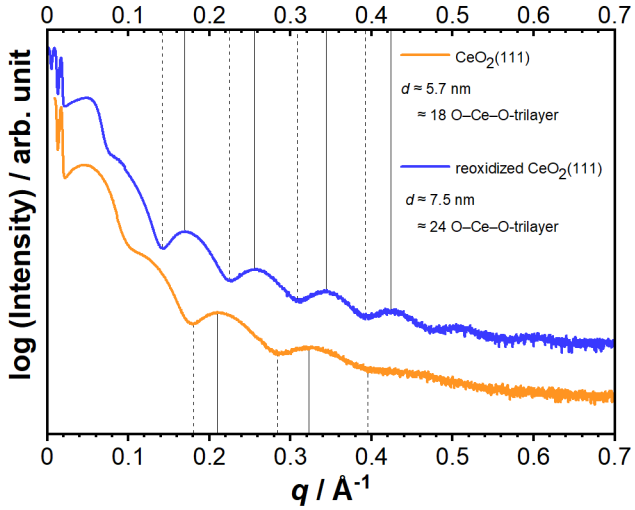

Figure 6.3: XRR measurements of a stoichiometric fully oxidized CeO_2(111) thin film (orange) with a thickness of d ≈ 5.7 nm grown in the LEED chamber. In blue the XRR measurement of a second CeO_{2-x}(111) thin film is shown, which was grown under similar conditions as the LEED film but in the XPS chamber and afterwards reduced and re-oxidized during the beamtime. The thickness ratio d_{reox}/d_{ox} = 1.32 is in reasonable agreement with the deposition times t_{dep} in **Chapter 6.5.2** considering the preparation at two different chambers. Adapter from references[1,2].

6.6.2 Determination Reduction Degree

The reduction degree *x* of the CeO_{2-x}(111) thin films can be determined with X-ray spectroscopy techniques, like XPS (Ce 3d and Ce 4d) and NEXAFS (Ce $M_{4,5}$ edge). Ceria yields complex spectra, for example the XP spectra of Ce 3d depicted in **Figure 7.4** or Ce 4d depicted in **Figure 6.5**. The XP Ce 3d spectra for fully oxidized CeO_2(111)/Ce^{4+} and fully reduced Ce(III) oxide/Ce^{3+} contain six and four peaks, respectively. For the 3d core level two peak might be expected due to spin-orbit splitting. The additional peaks (two for Ce^{3+} and four for Ce^{4+}) result from so-called "shakedown" states. Here electrons can be transferred from the O 2p level to the Ce 4f level in the excited state.[35,132,133] Ce 4d spectra are even more complex than Ce 3d spectra as in addition to spin-orbit splitting and shake-down effects due to a coupling of an unpaired electron in the Ce 4d final state with an electron in the Ce 4f level.[35,134,135]

For quantification of the reduction degree *x* a linear combination approach[35] is used instead of a deconvolution. As example in **Figure 6.4** and **Figure 6.5** the freshly reduced CeO_{2-x}(111) surface is measured at the FlexPES beamline once with bulk-sensitive NEXAFS (**Figure 6.4**) and once with surface-sensitive XPS (Ce 4d) (**Figure 6.5**). For comparison the measured references are shown in gray for the fully oxidized surface (CeO_2) and in black for the fully reduced surface (Ce_2O_3). The fully oxidized surface corresponds to the stochiometric freshly oxidized film. The fully reduced Ce_2O_3 films is prepared in-situ by depositing (U = 800 V, P = 40-50 W, Flux = 2.0 µA, deposition time t_{dep} = 30 min) metallic Ce on Ir(111) under UHV conditions and annealing the film to 1250 K. The residual water pressure in the UHV chamber is sufficient to oxidize the Ce

film to Ce_2O_3. The corresponding spectra of CeO_2 and Ce_2O_3 (XPS-Ce 4d, NEXAFS Ce $M_{4,5}$ edge) agree well with those reported in the literature.[2,35,136–139]

All NEXAFS spectra including the reference spectra are normalized by the energy-dependent flux and the integral intensity in the range from 865.5 eV to 918.5 eV (**Figure 6.4**).

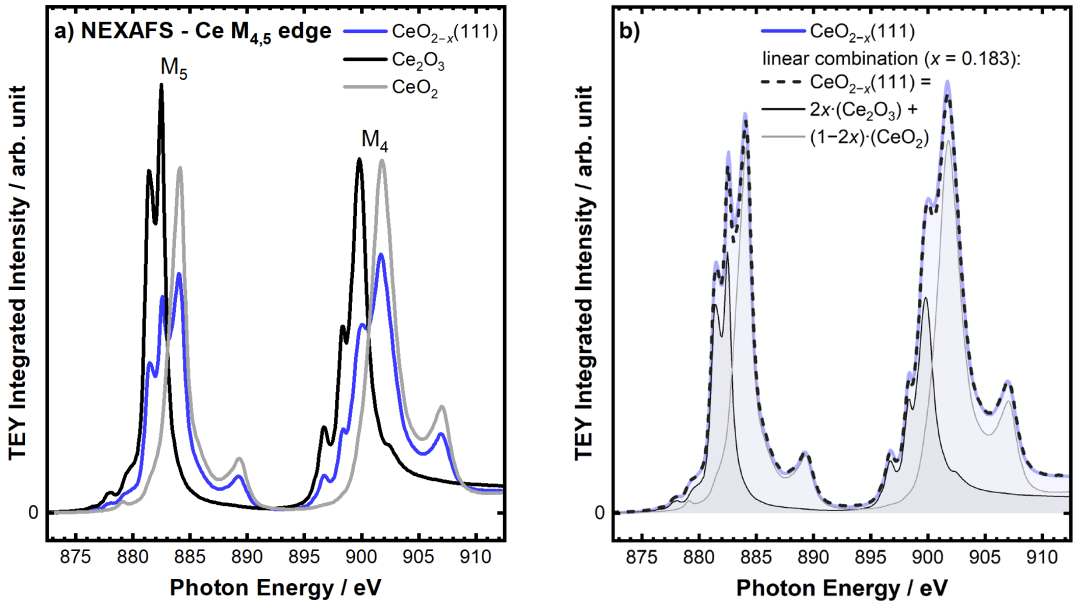

Figure 6.4: a) Bulk-sensitive NEXAFS Ce $M_{4,5}$ edge (Ce 3d) spectra measured in total electron yield (TEY) mode of partly reduced, pristine $CeO_{2-x}(111)$ (blue), fully reduced reference Ce_2O_3 (black) and fully oxidized reference $CeO_2(111)$ (gray). b) Procedure of linear combination for NEXAFS exemplified for pristine $CeO_{2-x}(111)$: $NEXAFS(CeO_{2-x}(111)) = 2x \cdot NEXAFS(Ce_2O_3) + (1\text{-}2x) \cdot NEXAFS(CeO_2)$, with $x = 0.18$ (37% Ce^{3+} fraction). Adapted from reference[2].

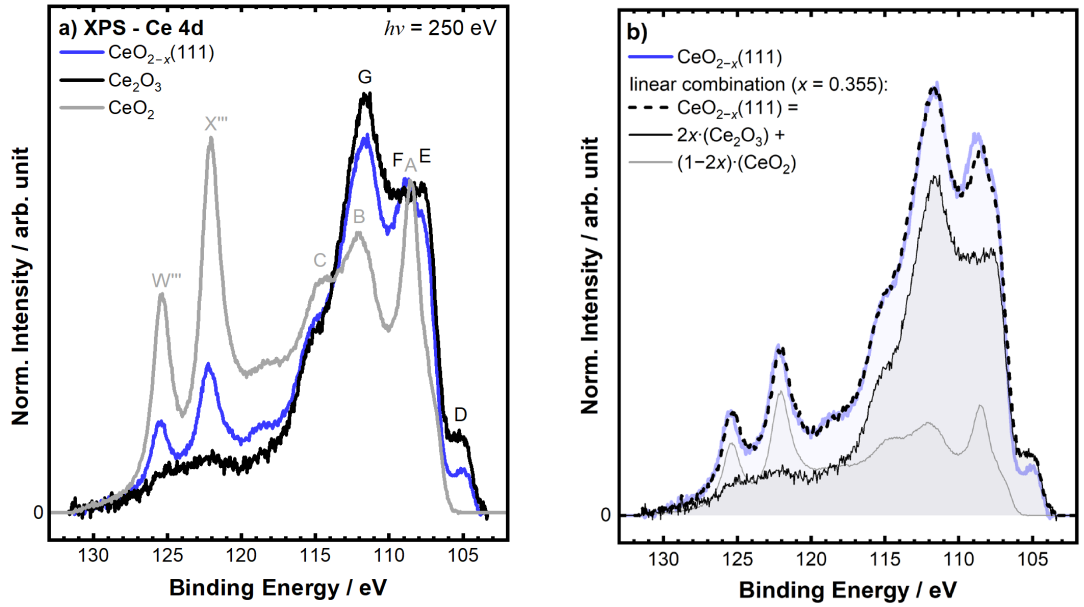

Figure 6.5: Surface-sensitive Ce 4d XP spectra ($h\nu = 250$ eV) of partly reduced, pristine $CeO_{2-x}(111)$ (blue), chlorinated Cl_{vac}- $CeO_{2-x}(111)$ (orange), fully reduced reference Ce_2O_3 (black) and fully oxidized reference $CeO_2(111)$ (gray). b) Procedure of linear combination for XPS exemplified for pristine $CeO_{2-x}(111)$: $XPS(CeO_{2-x}(111)) = (1\text{-}2x) \cdot XPS(CeO_2) + 2x \cdot XPS(Ce_2O_3)$, with $x = 0.35$ (71% Ce^{3+} fraction). Adapted from reference[2].

The bulk reduction degree x and corresponding Ce^{3+} fraction ($2x \cdot 100\%$) of $CeO_{2-x}(111)$ is derived from the Ce $M_{4,5}$ edge NEXAFS spectrum (TEY yield) by fitting the NEXAFS spectrum of $CeO_{2-x}(111)$ as a linear combination of the reference spectra of the fully oxidized $CeO_2(111)$ film (0% Ce^{3+}) and a fully reduced Ce_2O_3 film (100% Ce^{3+}): $(1-2x) \cdot$ NEXAFS(CeO_2) + $2x \cdot$ NEXAFS(Ce_2O_3)." The surface reduction degree x is derived from the Ce 4d XP spectrum in a similar manner. The procedure of linear combination is summarized in **Figure 6.4**, resulting in a bulk Ce^{3+} fraction of 37% (x = 0.183) that is in between those of (3 × 3) and ($\sqrt{7} \times \sqrt{7}$)R19.1°. Accordingly, in LEED a faint (3 × 3) is visible (cf. **Figure 7.1**). For comparison the reduction degree at the surface is much higher 71% (x = 0.355) in agreement with the reported gradient in the literature.[2,103] In a similar manner the reduction degree of the lab XPS spectra of Ce 3d can be determined (cf. **Figure 7.4**, Appendix **Figure 10.2**).

7 Results: HCl Oxidation on CeO_{2-x}(111) Thin Films

This chapter is divided into a "chlorinator" part and an "oxidizer" part, in the same way as the in the thought experiment of the chemical looping reactor (cf. **Chapter 5.2**, **Figure 5.2**). First, the results from the "chlorinator" will be discussed (**Chapter 7.1**). These can be further separated into the investigation of the chlorination of the surfaces upon HCl exposure (**Chapter 7.1.1**) and water formation (**Chapter 7.1.2**) upon annealing. Second, the results from the "oxidizer" are shown (**Chapter 7.2**). These can be separated into the re-oxidation of the surface upon O_2 exposure (**Chapter 7.2.1**) and a de-chlorination of the surface (**Chapter 7.2.2**).

7.1 "Chlorinator": Chlorination of the Model Catalyst

The chlorination of the surface and concomitant water formation mimics the steps (**A-D**) in **Figure 5.1** and is performed by exposing reduced CeO_{2-x}(111) surfaces to HCl at room temperature and annealing to the process temperature afterwards. This is investigated via lab-based LEED (fingerprinting), XPS, and TPD experiments.[28] These are complemented by DFT+U calculations and synchrotron-based XPS measurements.

7.1.1 Chlorination

LEED Fingerprinting Results

First, various ordered CeO_{2-x}(111) surfaces were prepared at the LEED chamber forming well-ordered $(\sqrt{7} \times \sqrt{7})$R19.1°, (3 × 3), and (4 × 4) reconstructions with distinct degree of reduction, i.e. x = 0.21, 0.29, and 0.40, respectively, which are close to the corresponding values of x = 2/7, 0.33, and 0.5, reported in the literature[103,105]. The superstructures are evidenced by LEED patterns with low background intensity and sharp LEED reflections (cf. **Figure 7.1**a).[2] Saturating these reduced ordered CeO_{2-x}(111) films with 15 L HCl at room temperature led in all cases (i.e., $(\sqrt{7} \times \sqrt{7})$R19.1°, (3 × 3), or (4 × 4)) to the development of a blurry (1 × 1) structure, while the former reconstruction of the pristine CeO_{2-x}(111) disappeared (cf. **Figure 7.1**b). Room temperature was chosen for HCl dosing in order to protect the equipment. Upon annealing to 700 K, the typical reaction temperature of the Deacon process, a $(\sqrt{3} \times \sqrt{3})$R30° became visible in all cases, whose ordering could be improved by an annealing step to 900 K (cf. **Figure 7.1**c).

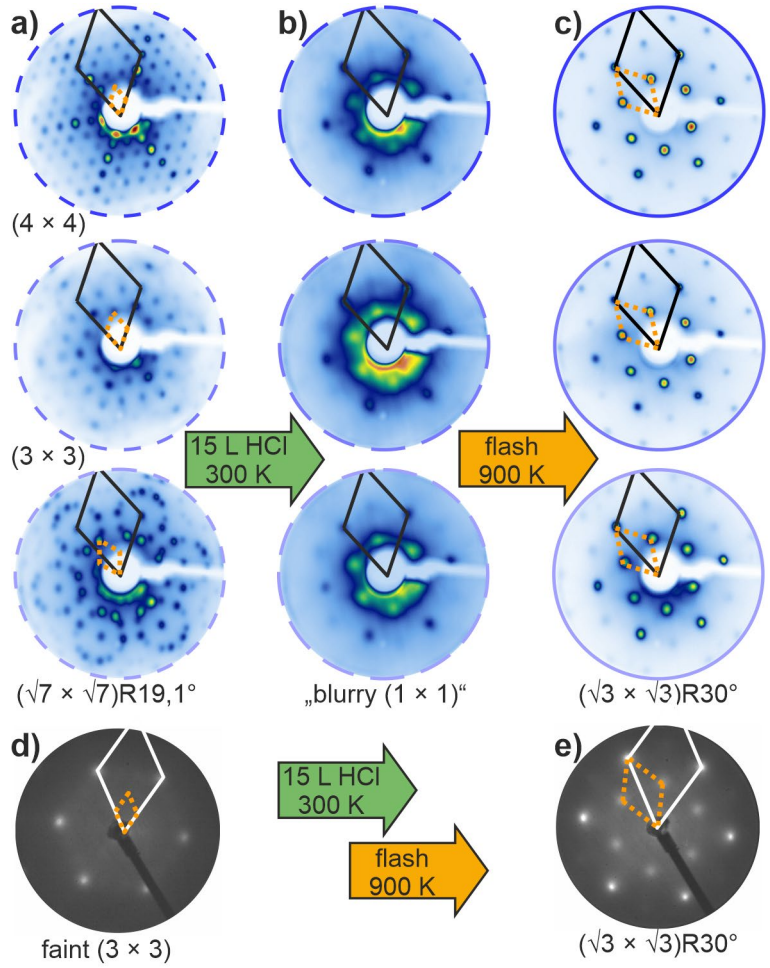

Figure 7.1: LEED patterns taken at 47 eV of various reduced ordered phases of CeO_{2-x}(111) a) before, b) after saturation with HCl at 300 K, and c) after subsequent annealing to 900 K under UHV conditions. In all cases the final structure is a (√3 × √3)R30°-Cl_{vac} superstructure. The (1 × 1) unit cell (black) and the unit cells of the superstructures (orange) are indicated.[1] For comparison the d) LEED pattern of the reduced CeO_{2-x}(111) surface at the FlexPES beamline revealing a faint (3 × 3) reconstruction (energy = 67 eV) with x = 0.18 (37% Ce^{3+} fraction, cf. **Chapter 6.6.2**) and e) exposing a (√3 × √3)R30°-Cl_{vac} superstructure (energy = 46 eV) after exposure to 15 L HCl at room temperature and subsequent flashing to T = 1000 K. Adapted from references[1,2,28].

Among the various starting structures of reduced CeO_{2-x}(111), the best-ordered ($\sqrt{3}$ × $\sqrt{3}$)R30° Cl-overlayer structure was accomplished when saturating the CeO_{2-x}(111)-(4 × 4) or CeO_{2-x}(111)-(3 × 3) surfaces with HCl at room temperature and subsequent annealing to 900 K. In the following, the various ($\sqrt{3}$ × $\sqrt{3}$)R30° overlayer superstructures based on reduced CeO_{2-x}(111) will be referred to as $\sqrt{3}$Cl-(√7 × √7)R19.1°, $\sqrt{3}$Cl-(3 × 3), or $\sqrt{3}$Cl-(4 × 4), in order to emphasize the initial reconstruction of the reduced CeO_{2-x}(111) surfaces.[1]

For comparison a reduced CeO_{2-x}(111) thin film (cf. **Chapter 6.5.2**) was prepared at the FlexPES beamline revealing a faint (3 × 3) reconstruction (cf. **Figure 7.1**d). After exposure to 15 L HCl at room temperature and subsequent flashing to T = 1000 K,[2] a ($\sqrt{3}$ × $\sqrt{3}$)R30° LEED pattern is revealed as well (cf. **Figure 7.1**e). The faintness (3 × 3) of the reconstruction could result from the time between preparation and LEED

measurement due to the high reactivity of the reduced surfaces. Therefore, the surface was annealed to 700 K in UHV for reactivation, prior to HCl dosing.

Besides the periodicity of the overlayer superstructure, LEED is able to provide information about the local adsorption geometry of the chlorine species.[1] In order to compare and distinguish the four lab based ($\sqrt{3} \times \sqrt{3}$)R30° overlayer superstructures based on reduced CeO_{2-x}(111) (cf. **Figure 7.1**) and stoichiometric CeO_2(111) (cf. **Figure 4.6**a), so-called lab-based LEED-IV (intensity versus voltage) curves were recorded (cf. **Figure 7.2**). Here the kinetic energy of the electrons and hence the diffraction conditions can be varied and the intensity of the diffracted beams can be measured. These LEED-IV curves contain, very similar to the X-ray diffraction intensities, detailed information on the local Cl-adsorption geometry and the variations in the CeO_{2-x}(111) substrate structure. In principle, this information can be retrieved from computing theoretical LEED-IV data within the multiple scattering approach that is based on a given model structure.[140] However, experimental LEED-IV curves can also be used alone in a semi-quantitative way, by comparing experimental LEED-IV data sets from different preparations, according to which similar LEED-IV curves of fractional order beams indicate a similar local adsorption geometry. This method was coined LEED fingerprinting technique.[1,141]

Restricted to LEED-IV curves of fractional order beams, mainly information on the Cl-induced surface structure with ($\sqrt{3} \times \sqrt{3}$)R30° symmetry is gained. As shown in **Figure 7.1**b the LEED-IV curves of the fractional order beams do not vary very much among the various preparations on the reduced CeO_{2-x}(111) surfaces so that the local coordination structure of chlorine species is inferred to be identical in all cases.

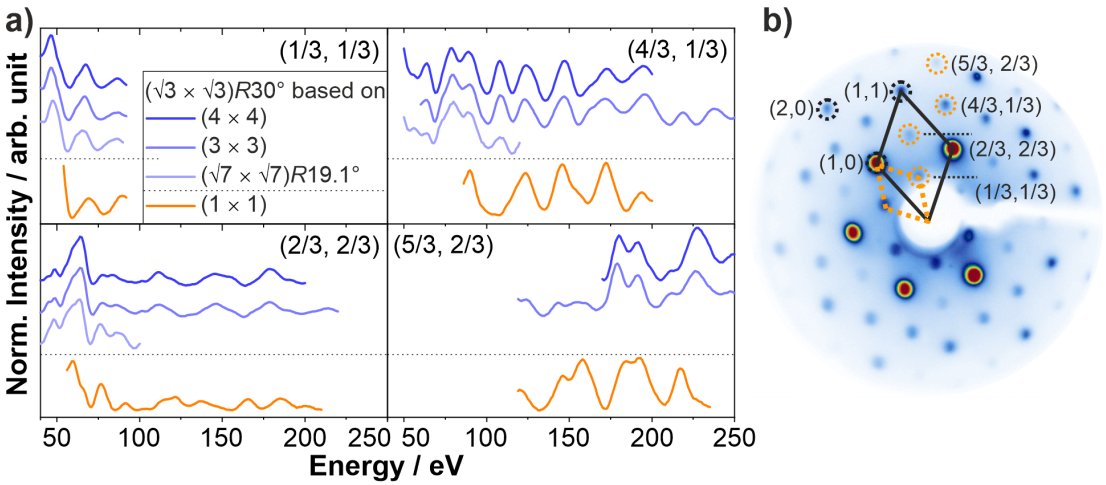

Figure 7.2: a) LEED-IV curves (fractional order beams) of ($\sqrt{3} \times \sqrt{3}$)R30° superstructures, prepared from various reduced ordered phases of CeO_{2-x}(111) (($\sqrt{7} \times \sqrt{7}$)R19.1°, (3 × 3), or (4 × 4)) after saturation with HCl at 300 K and subsequent annealing to 900 K under UHV conditions. For comparison, LEED-IV curves (orange) of the stoichiometric CeO_2(111)-(1 × 1) are shown that is exposed to 15 L HCl at room temperature, forming a ($\sqrt{3} \times \sqrt{3}$)R30°-Cl+H phase.[31] b) Example of a ($\sqrt{3} \times \sqrt{3}$)R30° LEED pattern at 90 eV. Integer and fractional order beams, the corresponding unit cells for the CeO_{2-x}(111) substrate (black) and $\sqrt{3}\times\sqrt{3}$)R30°-superstructure (orange) are indicated.[1] Adapted with permission from references[1,28].

The comparison among the various sets of LEED-IV curves can also be quantified by the Pendry R_P-factor (cf. **Table 7.1**). R_P-factors[142] of 0 and 1 signifies ideal agreement or full disagreement, respectively. A R_P-factor of < 0.25 is considered as a good agreement

between LEED-IV data, while a R_P-factor > 0.5 indicates poor agreement. The fractional order LEED-IV curves of the stoichiometric, oxidized, and $CeO_2(111)$-$(\sqrt{3} \times \sqrt{3})R30°$-Cl+H surface (cf. **Chapter 4.4**), i.e. $\sqrt{3}$Cl-(1 × 1), are very different from those of the reduced $CeO_{2-x}(111)$-$(\sqrt{3} \times \sqrt{3})R30°$-Cl surfaces, i.e. $\sqrt{3}$ Cl-$(\sqrt{7} \times \sqrt{7})R19.1°$, $\sqrt{3}$Cl-(3 × 3), or $\sqrt{3}$Cl-(4 × 4), (cf. Appendix, **Table 10.2** and **Table 10.1**), implying that also the adsorption geometry of chlorine species must be different in these two systems.[1]

Table 7.1: Quantitative comparison of fractional order beams via the R_P-factor: The three HCl-induced lab-based $(\sqrt{3} \times \sqrt{3})R30°$ surface structures, i.e. $\sqrt{3}$Cl-$(\sqrt{7} \times \sqrt{7})R19.1°$, $\sqrt{3}$Cl-(3 × 3), and $\sqrt{3}$Cl-(4 × 4), on differently reduced $CeO_{2-x}(111)$ surfaces are in good agreement among each other (green background color). In contrast, the $(\sqrt{3} \times \sqrt{3})R30°$-Cl+H surface structure on the stoichiometric oxidized $CeO_2(111)$ surface, $\sqrt{3}$Cl-(1 × 1), shows a poor agreement with the $(\sqrt{3} \times \sqrt{3})R30°$ surface structures formed on the reduced surfaces (red). Here, the example of the $\sqrt{3}$Cl-(3 × 3) is shown (cf. Appendix, **Table 10.1**). The first two columns indicate which experimental surface structures are compared through the indicated IV curves (cf. **Figure 7.2**) of the structures in the first row. Adapted with permission from references[1,28].

Comparison of **HCl**-induced $(\sqrt{3} \times \sqrt{3})R30°$ based on		(1/3, 1/3)	(2/3, 2/3)	(4/3, 1/3)	(5/3, 2/3)	**Average ⌀**
$(\sqrt{7} \times \sqrt{7})R19.1°$	vs. (3 × 3)	0.19	0.21	0.14	-	**0.18**
$(\sqrt{7} \times \sqrt{7})R19.1°$	vs. (4 × 4)	0.25	0.37	0.30	-	**0.31**
(3 × 3)	vs. (4 × 4)	0.08	0.11	0.09	0.19	**0.11**
(1 × 1)	vs. (3 × 3)	0.44	0.95	0.43	0.74	**0.71**

For comparison, $(\sqrt{3} \times \sqrt{3})R30°$ structures were prepared in the LEED chamber by exposing the various reduced $CeO_{2-x}(111)$ surfaces to Cl_2, and recording sets of LEED-IV curves (cf. Appendix, **Figure 10.1**). Both preparation methods (Cl_2 and HCl exposure) lead to virtually identical LEED-IV curves of fractional order beams (cf. Appendix, **Table 10.2** and **Table 10.3**) associated with an identical local adsorption geometry of Cl. Adsorption of Cl_2 on the stoichiometric-oxidized $CeO_2(111)$ surface is endothermic and, therefore, experimentally not observed.[1]

DFT+U calculations,[31,119,143] showed that Cl adsorbs on-top of Ce sites on the stoichiometric $CeO_2(111)$ surface (cf. **Chapter 4.4**). Additional DFT+U calculations (vide infra) for Cl adsorption on the reduced $CeO_{2-x}(111)$ surfaces indicate that chlorine preferentially adsorbs in surface oxygen vacancies, $V_{O,s}$. Combining this with the above LEED fingerprinting results, it can be concluded that chlorine adsorbs in surface oxygen vacancies, independent of the actual degree of reduction x of $CeO_{2-x}(111)$ for $0.4 \gtrsim x \gtrsim 0.2$. In the following, the $(\sqrt{3} \times \sqrt{3})R30°$ overlayer superstructures based on reduced $CeO_{2-x}(111)$ will be referred to as $(\sqrt{3} \times \sqrt{3})R30°$-$Cl_{vac}$.

The LEED-IV fingerprinting approach can also be applied to the integer order beams (cf. Appendix, **Figure 10.1**). Here the differences among the various sets of experimental LEED-IV data of the reduced $CeO_{2-x}(111)$ surfaces are substantial, as quantified by R_P-factors exceeding $R_P > 0.58$ (cf. Appendix, **Table 10.4**). These results indicate that the structures of the reduced surface reconstructions are different, in agreement with the degree of reduction x of the $CeO_{2-x}(111)$ surfaces.[1]

Characterization of the Cl_{vac} Species

Flashing the $\sqrt{3}$Cl-(4 × 4) overlayer to 1500 K in UHV lead to reversible transformation from the $\sqrt{3}$Cl-(4 × 4) to the pristine CeO_{2-x}(111)-(4 × 4) phase. Upon heating to 1500 K, chlorine desorbs completely from the surface. In order to restore the original (4 × 4) reconstruction, oxygen vacancies V_O reversibly migrate from the surface to the near-surface region or vice versa (cf. discussion **Chapter 7.1.1**). Additionally, oxygen may desorb at these high temperatures resulting in an improved surface ordering.[1]

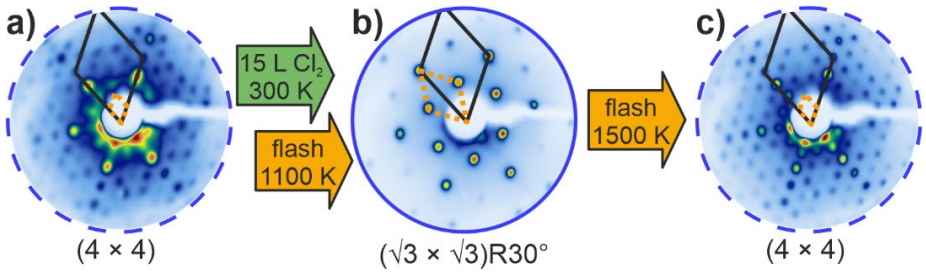

Figure 7.3: LEED pattern at 47 eV of the CeO_{2-x}(111)-(4 × 4) phase a) before and b) after exposure to 15 L HCl at 300 K and subsequent annealing to 1100 K under UHV conditions. c) Finally the surface is annealed to 1500 K to recover reversibly the CeO_{2-x}(111)-(4 × 4) phase. Adapted with permission from references[1,28].

XPS and NEXAFS Results

In the lab the degree of reduction x of the various ordered CeO_{2-x}(111) surfaces can be derived from the intensity of Ce^{4+}- and Ce^{3+}-related features in the Ce 3d XP spectra (cf. **Figure 7.4**) of fully reduced Ce_2O_3(111) and stoichiometric CeO_2(111) via a linear combination approach[35,144] (cf. **Chapter 6.6.2** and Appendix, **Figure 10.2**). The Ce^{3+} fraction of CeO_{2-x}(111) on Ru(0001) turns out to be: ($\sqrt{7}$ × $\sqrt{7}$)R19.1°: 41% (x = 0.21), (3 × 3): 58% (x = 0.29), or (4 × 4): 79% (x = 0.40) which is in reasonable agreement with a previous study[31] of such CeO_{2-x}(111) layers on Cu(111) [($\sqrt{7}$ × $\sqrt{7}$)R19.1°: 28%, (3 × 3): 52%, or (4 × 4): 95%]. The agreement with literature is not fully quantitative since the observed surface reconstructions are stable within ± 5-10% of x.[1] In addition, the film thickness and the resulting probing depth needs to be considered (cf. **Figure 4.5**). For comparison, the reduced film at the FlexPES beamline revealed a faint (3 × 3) reconstruction, for which a Ce^{3+} fraction between 52% and 58% is expected. However, the bulk-sensitive NEXAFS measurement yielded a Ce^{3+} fraction of 37% and the surface-sensitive Ce 4d XPS measurement a fraction of 71%, utilizing the linear combination of CeO_2(111) and Ce_2O_3 reference spectra (cf. **Figure 6.5**). While NEXAFS probes the whole film, the Ce 4d spectra probe the topmost surface only. In between these boundaries the probing depth of lab-based XPS is located. Hence, the measured lab-based data are in good agreement with the averaged (54%) Ce^{3+} fraction as determined by NEXAFS and surface-sensitive XPS. This gradient of the Ce^{3+} fraction is also consistent with recent studies from the Matolín research group.[103] (cf. **Figure 4.5**) Ce 4d XP spectra and NEXAFS Ce $M_{4,5}$ edge spectra of CeO_{2-x}(111) and Cl_{vac}-CeO_{2-x}(111) including the reference spectra of Ce^{4+} and Ce^{3+} are summarized in (**Figure 6.4**, **Figure 6.5** and Appendix, **Figure 10.4**, **Figure 10.5**).

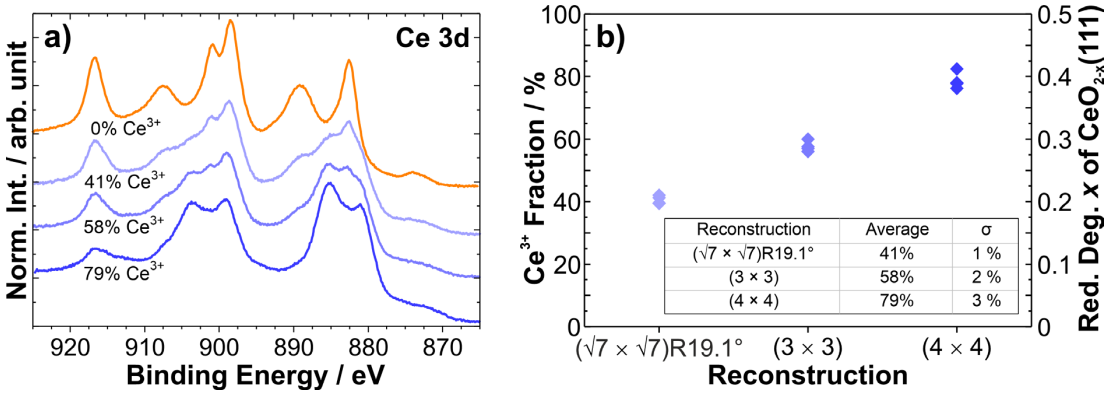

Figure 7.4: Ce 3d XP spectra (a) of various ordered $CeO_{2-x}(111)$ structures from which the Ce^{3+} fraction can be quantified (b) via linear combination (cf. **Figure 10.2**). Adapted with permission from references[1,28].

In order to quantify the coverage of the chlorine overlayer, lab-based Cl 2p XP spectra for the variously prepared $(\sqrt{3} \times \sqrt{3})$R30°-$Cl_{vac}$ overlayers on differently reduced $CeO_{2-x}(111)$ surfaces were taken (cf. **Figure 7.5**), after annealing to 700 K. The Cl 2p doublet is slightly shifted to higher binding energy (by ΔE_{BE} ~0.4eV), in comparison with the stoichiometric $CeO_2(111)$-$(\sqrt{3} \times \sqrt{3})$R30°-Cl+H. This may point to a site change of chlorine species: the Cl 2p spectral features on $CeO_2(111)$ are observed at 199.1eV/200.7eV (for Cl_{top})[31] and 199.7eV/201.3eV for $CeO_{2-x}(111)$.[28] However, this shift in binding energy is substantially smaller than that found on $RuO_2(110)$: Cl_{top} (196.1eV/197.6) and Cl_{br} (197.6/199.2).[62,145,146] The high-energy component of Cl_{top} on $CeO_2(111)$ is 2-3eV shifted to higher binding energies if compared to Cl_{top} on $RuO_2(110)$[1] (cf. **Figure 3.1**b).

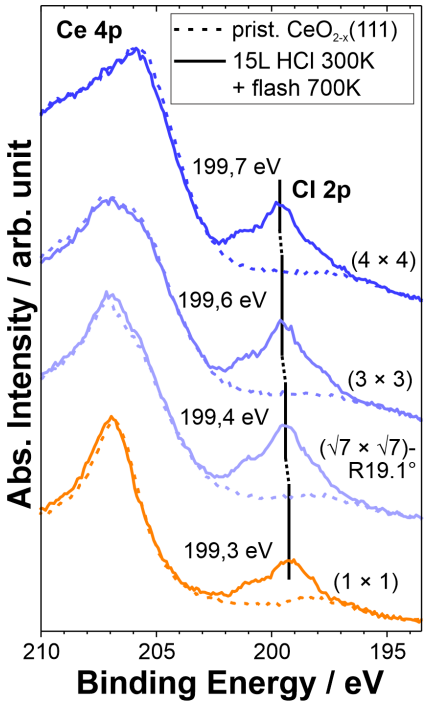

Figure 7.5: Cl 2p and Ce 4p XP spectra of stoichiometric $CeO_2(111)$ and various reduced phases of $CeO_{2-x}(111)$ after exposure to 15 L HCl at 300 K (saturation) and flash to 700 K. Adapted with permission from references[1,28].

From the invariance of the Cl 2p spectra in **Figure 7.5** for all $(\sqrt{3} \times \sqrt{3})$R30°-$Cl_{vac}$ phases, starting from $CeO_{2-x}(111)$-$(\sqrt{7} \times \sqrt{7})$R19.1°, -(3 × 3) or -(4 × 4), the Cl coverage

is inferred to be independent of the surface vacancy concentration of the pristine surfaces. This observation is not reconciled with island formation, but instead points towards a uniform, covering $(\sqrt{3} \times \sqrt{3})$R30°-$Cl_{vac}$ overlayer. If Cl adsorbs only in surface oxygen vacancy positions $V_{O,s}$ then the surface vacancy concentration after HCl saturation needs to be independent of the reduction degree x. Therefore, it is concluded that oxygen vacancies need to migrate from the near-surface region towards the surface in order to provide the same $V_{O,s}$ vacancy concentration to stabilize the fully covering $(\sqrt{3} \times \sqrt{3})$R30°-$Cl_{vac}$ surface structure (cf. discussion).[1]

TPD Results

Temperature programmed desorption (**Figure 7.6**) indicates the adsorption energy of Cl being sensitively dependent on the degree of reduction x of CeO_{2-x}(111), shifting the maximum desorption from 1175 K (weakly reduced: $(\sqrt{7} \times \sqrt{7})$R19.1°) to 1320 K (strongly reduced: (4 × 4)). Surface coverage-dependent measurements series are challenging due to the high desorption temperatures, leading to high repetitive thermal load of the holding tungsten wires resulting into contact loss of the latter. Instead, by Cl 2p XP spectra the Cl coverage can be followed as a function of the temperature (cf. Appendix, **Figure 10.3**a). Also, here it is evident, that the temperature-induced removal of surface Cl depends on the degree of reduction x of the CeO_{2-x}(111) surface.[1]

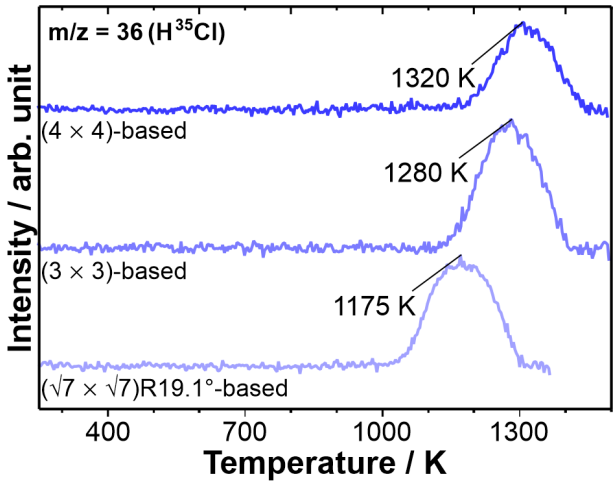

Figure 7.6: Temperature programmed desorption at 4 K/s of a) chlorine desorbing from HCl-saturated, reduced CeO_{2-x}(111) surfaces (cf. **Figure 7.5**). Adapted with permission from references[1,28].

DFT+U Results

Complementary DFT+U calculations indicate that Cl preferentially adsorbs in the surface oxygen vacancies, $V_{O,s}$, on the reduced CeO_{2-x}(111) surfaces: The adsorption of one Cl atom on the stoichiometric CeO_2(111) surface is endothermic with an adsorption energy of +0.35 eV, whereas if adsorbed on a reduced CeO_{2-x}(111)-$(\sqrt{3}\times\sqrt{3})$R30° surface with one $V_{O,s}$, the adsorption is strongly exothermic with an energy of −2.64 eV (see **Figure 7.7**a and b).

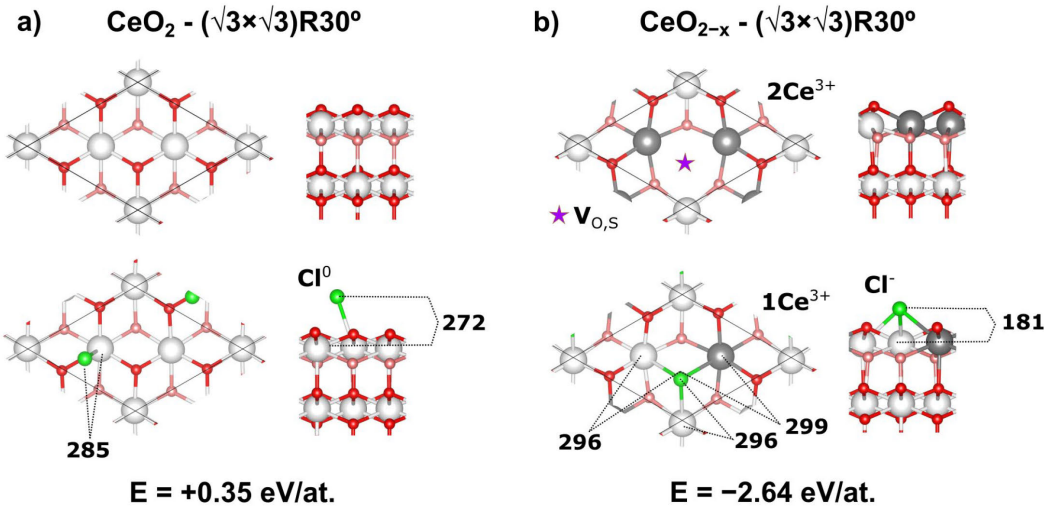

Figure 7.7: Top and side views of pristine surfaces and with one adsorbed Cl atom. a) Stoichiometric oxidized CeO_2(111)-(√3×√3)R30° surface, b) reduced CeO_{2-x}(111)-(√3×√3)R30° surface with one surface oxygen vacancy, $V_{O,s}$. Distances are given in pm and adsorption energies in eV per Cl atom (w.r.t. ½ Cl_2). Color code: Ce^{4+} and (Ce^{3+}) ions are white (gray), the oxygen surface (subsurface) ions are red (light red) and Cl atoms are green. Adapted with permission from reference[1].

The number of Ce^{3+} cations provides information regarding the oxidation state of the adsorbed Cl atom. On CeO_2(111), Cl adsorbs slightly displaced on a Ce top site as Cl^0 (no Ce^{3+} available). On CeO_{2-x}(111)-(√3×√3)R30° with one $V_{O,s}$ and two Ce^{3+}, chlorine adsorbs on a $V_{O,s}$ site as Cl^-, since Cl takes an electron from one adjacent Ce^{3+} to form Ce^{4+} due to its electronegativity. The different oxidation states of chlorine might also explain why the Cl 2p doublet (cf. **Figure 7.5**) has virtually no shift in binding energy (ΔE_{BE} ~0.4eV) between adsorption on-top Ce^{4+} (Cl_{top} for CeO_2(111)) and in an oxygen vacancy (Cl_{vac} for CeO_{2-x}(111)). The shift due to the different oxidation state and adsorption site partly compensates.[1]

The Cl 2p spectra (cf. **Figure 7.5**) indicate that the three reduced ceria phases ($(\sqrt{7} \times \sqrt{7})$R19.1°, (3 × 3), and (4 × 4)) exhibit the same Cl coverage. However, the TPD results show (cf. **Figure 7.6**) that Cl is more strongly adsorbed in case of the (4 × 4) phase with a higher concentration of near-surface vacancies compared to the other two phases ((3 × 3) and ($\sqrt{7} \times \sqrt{7}$)R19.1°). In order to rationalize these experimental results, the adsorption energy per Cl atom is calculated for a concentration of Cl_{vac} species of $\Theta \approx 1/3$ for each phase. The Cl coverage is defined as the ratio of the number of Cl atoms to the number of Ce atoms in the topmost trilayer. The specific Cl concentration values $\Theta((\sqrt{7} \times \sqrt{7})$R19.1°-Cl) = 2/7 ≈ 0.29, Θ((3 × 3)-Cl) = 3/9 = 0.33, and Θ((4 × 4)-Cl) = 5/16 ≈ 0.31 ensure to describe the experimental conditions and reduce possible coverage effects in the calculation of the adsorption energy of Cl species on the reduced ceria phases.

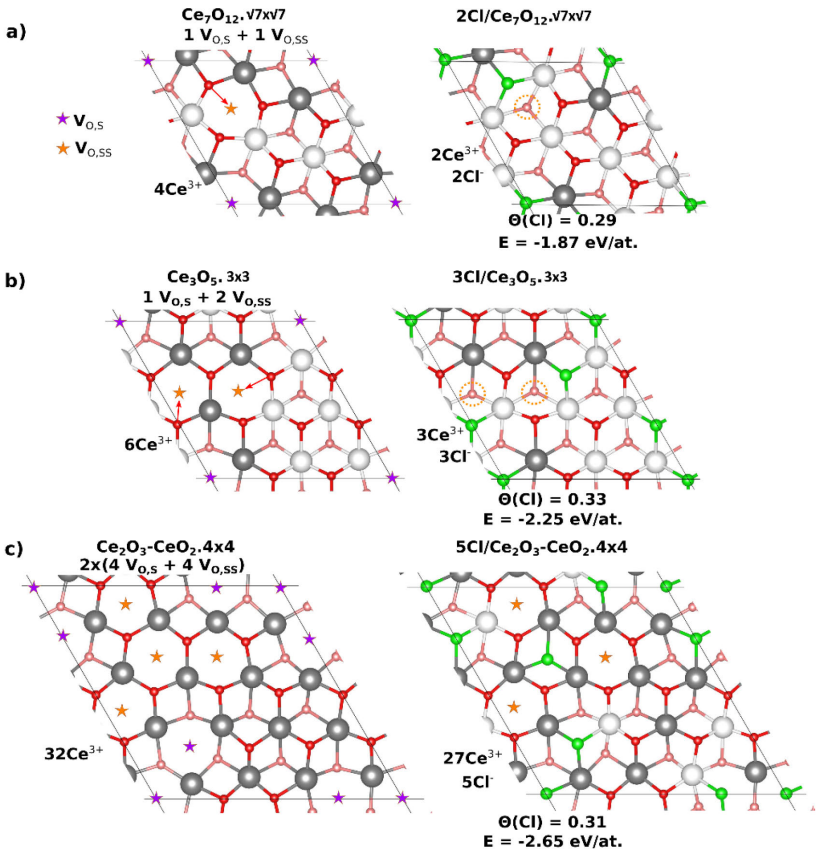

Figure 7.8: Top views of pristine reduced CeO_{2-x}(111) surface reconstructions and with adsorbed Cl atoms. a) CeO_{2-x}(111)-(√7 × √7)R19.1°, b) CeO_{2-x}(111)-(3 × 3), and c) CeO_{2-x}(111)-(4 × 4). The violet (orange) stars indicate the position of the $V_{O,S}$ ($V_{O,SS}$) oxygen vacancies. In a), b) and c) 2, 3 and 5 Cl atoms are adsorbed, with a coverage of Θ = 0.29, 0.33 and 0.31, respectively. The red arrows (left) indicate the surface oxygen that moves filling the subsurface vacancy (orange dotted circle, right), after adsorbing Cl. Averaged adsorption energies are in eV per Cl atom (w.r.t. ½ Cl_2). Color code as in Figure 7.7. Adapted with permission from reference[1].

The calculated adsorption energies indicate the same trend as observed in the TPD experiments, i.e., the binding of Cl species increases as surface reduction increases (cf. **Figure 7.6**), i.e., |E((√7 × √7)R19.1°-Cl)| = 1.87 eV/at. < |E((3 × 3)-Cl)| = 2.25 eV/at. < |E((4 × 4)-Cl)| = 2.65 eV/at (see **Figure 7.8 a-c**). Geometrically, it is observed that the average Cl^- distance to the plane of the Ce atoms of the first trilayer decreases by 91 pm with respect to Cl^0 species on the stoichiometric CeO_2(111)-(√3 × √3)R30° surface.

The structures in **Figure 7.8** show that Cl preferentially adsorbs in the oxygen surface vacancies, $V_{O,S}$, as Cl^-. Due to the interaction of Cl with the surfaces, the spontaneous mobility of some surface oxygen atoms is observed in case of the (√7 × √7)R19.1° and (3 × 3) phases, which fill subsurface oxygen vacant sites $V_{O,SS}$. For the reduced (√7 × √7)R19.1° reconstruction, the initial adsorption of 2 Cl atoms in one surface vacancy $V_{O,S}$ and one subsurface vacancy $V_{O,SS}$ results in the adsorption of Cl species in 2 $V_{O,S}$, whereas the (3 × 3) reconstruction, which initially adsorbs 3 Cl atoms in one surface vacancy $V_{O,S}$ and two subsurface vacancies $V_{O,SS}$, ends up with Cl species filling 3 $V_{O,S}$. This effect is not observed in the (4 × 4) phase, where 5 Cl atoms are adsorbed, since the structure (cf. Figure 4.4b) has two fully reduced ceria trilayers, Ce_2O_3, which hinders the mobility of oxygen atoms.[1]

Discussion

Adsorption Geometry and Adsorption Strength of Chlorine on Reduced $CeO_{2-x}(111)$

DFT+U calculations indicate that chlorine adsorbs in surface oxygen vacancies of $CeO_{2-x}(111)$ with a high adsorption energy. The 3.0 eV higher adsorption energy of Cl_{vac} on $CeO_{2-x}(111)$ compared to Cl_{top} on the stoichiometric $CeO_2(111)$ surface is reconciled with the temperature programmed desorption and temperature-dependent Cl 2p XPS experiments (**Figure 7.6**). LEED fingerprinting indicates that the chlorine adsorption site on the reduced $CeO_{2-x}(111)$ surfaces is independent of the oxygen vacancy concentration of the corresponding pristine surfaces. Although the local adsorption geometry for Cl_{vac} is identical for the three considered ordered $CeO_{2-x}(111)$ surfaces (cf. **Figure 7.2**), the adsorption of chlorine is stronger the higher the degree of reduction x is. This is evidenced by additional Cl_2 TPD (cf. **Figure 10.3**) and corroborated by DFT+U calculations (cf. **Figure 7.8**). Altogether, chlorine adsorbs in surface oxygen vacancies on the reduced $CeO_{2-x}(111)$ surfaces, while the binding strength depends on the degree of reduction x, which involves not only surface vacancies but also those in deeper oxygen layers.

The most important result of the chlorination step is that the interaction of $CeO_{2-x}(111)$ surfaces with HCl from the gas phase requires exchanges of electrons and of oxygen vacancies in the near-surface region to finally adsorb Cl on the surface. By LEED fingerprinting (**Figure 7.1**) and Cl 2p XPS (**Figure 7.5**), it is shown that the surface coverage of Cl_{vac} on all of the reduced $CeO_2(111)$ surface reconstructions is not affected by the actual oxygen deficiency x of the $CeO_{2-x}(111)$ systems. Therefore, after saturation of HCl adsorption and annealing to 900 K, the surface concentration of oxygen vacancies in the $(\sqrt{3} \times \sqrt{3})R30°$-$Cl_{vac}$ overlayer needs to be identical and independent of the degree of reduction x of $CeO_{2-x}(111)$. The reduced surface reconstructions (4 × 4), (3 × 3), and $(\sqrt{7} \times \sqrt{7})R19.1°$ are determined by the arrangement of the oxygen vacancies[106] with different surface vacancy concentrations, being not commensurate with the $(\sqrt{3} \times \sqrt{3})R30°$ periodicity. The concentration of the oxygen vacancies in the various ordered $CeO_{2-x}(111)$ surfaces was previously estimated by Stetsovych et al. and Duchoň et al..[102,103] From these values collected in **Table 7.2** it is obvious that the surface vacancy concentration, $V_{O,s}$, is too small to allow for the formation of a $(\sqrt{3} \times \sqrt{3})R30°$-$Cl_{vac}$, even if only a Cl_{vac} coverage of $\Theta = 1/3$ is considered. Therefore, oxygen vacancies need to migrate from the subsurface oxygen layer, $V_{O,ss}$, of the topmost O-Ce-O trilayer (or deeper layers) to the topmost oxygen layer.

Table 7.2: Concentrations of oxygen vacancies per nm^2 for the various ordered $CeO_{2-x}(111)$ reconstructions from experiments[102,103] and theory[90,105] (given in parenthesis). Values for the topmost layer and the topmost trilayer are compared to those for the $(\sqrt{3} \times \sqrt{3})R30°$-$Cl_{vac}$ surface. Adapted with permission from references[1,28].

Unit cell	(4 × 4)	(3 × 3)	$(\sqrt{7} \times \sqrt{7})R19.1°$	**$(\sqrt{3} \times \sqrt{3})R30°$-$Cl_{vac}$**
$\#V_{O,s}/nm^2$ topmost layer	1.90 (1.92)	1.70 (0.86)	1.10 (1.10)	2.56
$\#V_{O,s}+V_{O,ss}/nm^2$ topmost trilayer	3.84 (3.84)	2.56 (2.56)	2.19 (2.20)	2.56

The diffusion process of oxygen vacancies is kinetically possible (cf. **Chapter 7.2**). According to previous ab-initio molecular dynamics (AIMD) studies[147] the mobility of oxygen vacancies in reduced CeO_{2-x}(111) is very low at room temperature. Diffusion of V_O within the topmost O-Ce-O trilayer is predicted to set in already at a temperature of 500 K. However, in molecular dynamics simulations[147] for the temperature range of 500-900 K the vacancy never left the topmost O-Ce-O trilayer towards deeper layers.

Microscopic Reaction Steps and Reactivity Patterns

The adsorption of HCl on CeO_{2-x}(111) proceeds via an acid-base reaction[31,117], $HCl(g) + V_O + O^{-II} \rightarrow Cl^-_{vac} + O^{-II}H^+$, that can be written in the Kröger-Vink notation:[72] $HCl(g) + V_{O,s}^{\bullet\bullet} + O_{O,s}^{x} \rightarrow Cl_{O,s}^{\bullet} + OH_{O,s}^{\bullet}$. To a first approximation the oxidations state of Ce is not affected by the acid-base adsorption reaction of HCl. The energy for dissociative HCl adsorption on (4 × 4) is exothermic by 2.70 eV[45], that is close to previously calculated adsorption energy of 2.85 eV[16] and is 1.5 eV higher than that on the stoichiometric CeO_2(111) surface,[31] making this chlorine species practically inactive for the evolution of Cl_2.[16]

As interim result it can be summarized that upon chlorination of the reduced surface with HCl and subsequent annealing Cl resides strongly bound in oxygen vacancies at the surface and forms a well-defined $(\sqrt{3} \times \sqrt{3})$R30°-$Cl_{vac}$ superstructure enabled by the reversible migration of oxygen vacancies. As second step of the chlorinator the water formation upon annealing will be investigated.

7.1.2 Water Formation

TPD Results

When the reduced CeO_{2-x}(111) surfaces with various reconstructions (cf. **Figure 7.1**), i.e. $(\sqrt{7} \times \sqrt{7})$R19.1°, (3 × 3), and (4 × 4), are saturated with HCl at room temperature, hydrogen desorbs upon annealing at about 620 K from the surface in the form of water or H_2 (cf. **Figure 7.9**) so that only chlorine remains on the surface. There is a systematic variation of water and H_2 formation as a function of the degree of reduction x of CeO_{2-x}(111). The more reduced the CeO_{2-x}(111) surfaces are, the less water desorbs from the surface and instead the more H_2 evolves. As expected from the constant Cl 2p signal in **Figure 7.5**, the sum of the water and H_2 desorption signals in TPD in **Figure 7.9**b are invariant for each preparation.

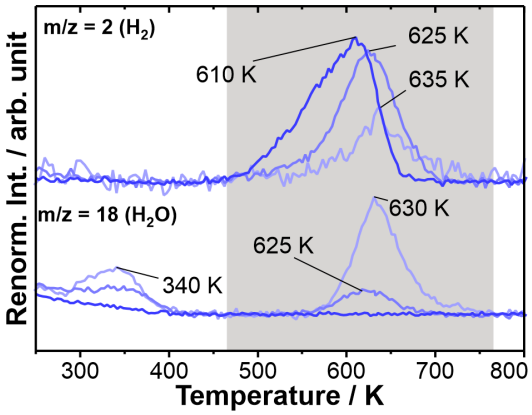

Figure 7.9: Temperature programmed desorption at 4 K/s of H_2 and water desorbing from HCl-saturated, reduced CeO_{2-x}(111) surfaces (cf. **Figure 7.6**). Adapted with permission from references[1,28].

XPS Results

For comparison the synchrotron-based Cl 2p and O 1s XP spectra of the CeO_{2-x}(111) sample at the FlexPES beamline are shown (**Figure 7.10**), after exposure to 15 L HCl and subsequent stepwise annealing to 1000 K. The shoulders at lower binding energy of the Cl 2p doublet at 198.6 eV/200.2 eV are assigned to chlorine still forming a hydrogen bond.[145] These shoulders disappear upon annealing to 1000 K, leaving only a single Cl component on the surface. Concomitant with the decline of the shoulder in Cl 2p, also the OH species[148] in the O 1s spectrum (cf. **Figure 7.10**b) disappear. This in agreement with previous lab-based XPS measurements[28] and also in reasonable agreement with the TPD spectra in **Figure 7.9**, considering the multiple annealing of the sample during the synchrotron-based measurements. The O 1s spectrum of fully chlorinated Cl_{vac}-CeO_{2-x}(111) is shifted by 0.39 eV when compared to that of the stoichiometric CeO_2(111) (cf. **Figure 10.8**).

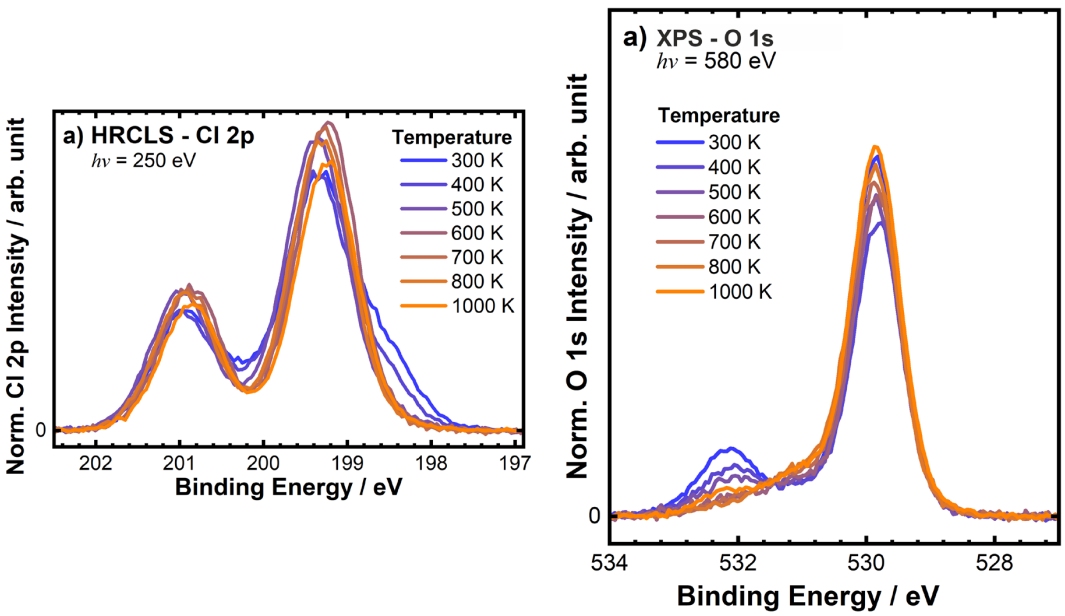

Figure 7.10: Surface-sensitive a) Cl 2p and b) O 1s XP spectra of CeO_{2-x}(111) when exposed to 15 L HCl at room temperature and subsequently annealed to 1000 K in steps of 100 K and 200 K to remove hydrogen. Adapted with permission from reference[2].

DFT Results

Furthermore, the experimental results of hydrogen TPD indicate that H_2 desorption is facilitated from surfaces with a higher degree of reduction x (shift form 635 K to 610 K, cf. **Figure 7.9**). The DFT+U calculations shown in figure **Figure 7.11** a-c support these results, since for a similar H coverage, an increase in the binding of H species is found as the surface degree of reduction x decreases : $|E((4 \times 4)\text{-H})| = 0.48$ eV/at < $|E((3 \times 3)\text{-H})| = 0.77$ eV/at < $|E((\sqrt{7} \times \sqrt{7})\text{R19.1°-H})| = 0.91$ eV/at.; this trend is opposite to that found for Cl species.

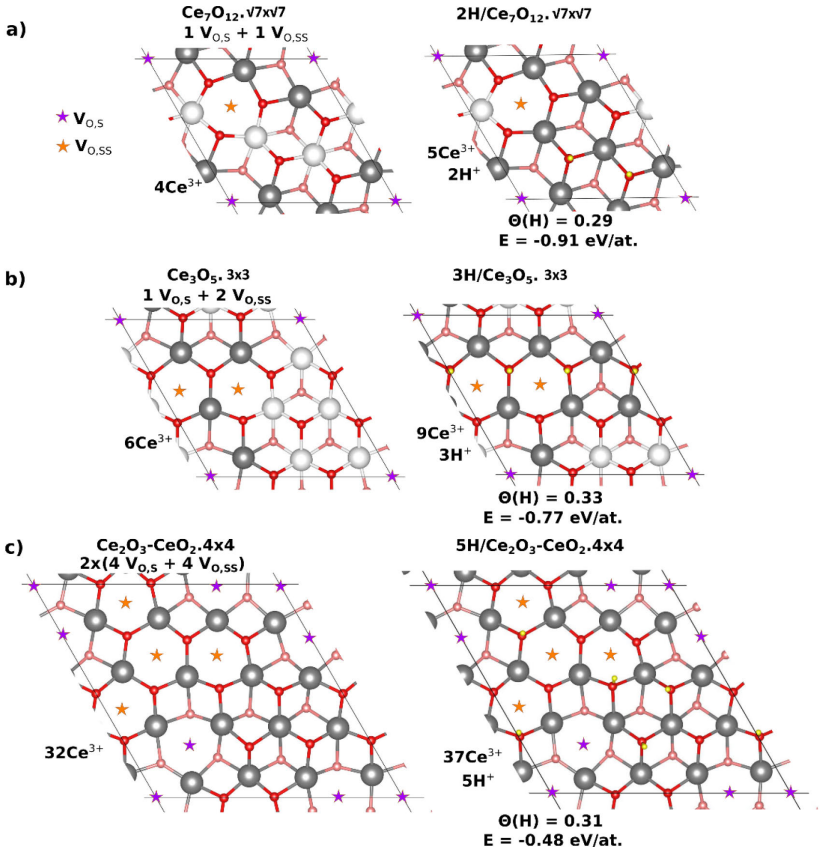

Figure 7.11: Top views of reduced CeO_{2-x}(111) surface reconstructions: pristine (left) and with adsorbed H atoms (right). a) $(\sqrt{7} \times \sqrt{7})$R19.1°, b) (3×3), and c) (4×4). The violet (orange) stars indicate the position of the $V_{O,s}$ ($V_{O,ss}$). In a), b), and c) 2, 3, and 5 H are adsorbed, with a coverage of $\Theta = 0.29$, 0.33, and 0.31, respectively. Averaged adsorption energies are in eV per H atom (w.r.t. ½ H_2). Adapted with permission from reference[1].

Discussion

Microscopic Steps and Reactivity Patterns

Upon increasing the surface temperature of chlorinated CeO_{2-x}(111) to 700 K, hydrogen leaves the surface either via H_2 or via water formation, depending on the degree of reduction x of CeO_{2-x}(111). This experimental result is remarkable since the surface structure of the chlorinated surface is identical for $\sqrt{3}$ Cl-(4×4), $\sqrt{3}$ Cl-(3×3), and $\sqrt{3}$ Cl-$(\sqrt{7} \times \sqrt{7})$R19.1°. Nevertheless, the H_2O/H_2 formation ratio varies quite considerably (cf. **Figure 7.9**). For the highly reduced $\sqrt{3}$Cl-(4×4) surface, hydrogen evolution dominates, while for the less reduced $\sqrt{3}$Cl-$(\sqrt{7} \times \sqrt{7})$R19.1° surface, water formation prevails. Water formation does not lead to a further reduction of CeO_{2-x}(111), i.e., higher Ce^{3+} fraction,

but instead only to the formation of an additional vacancy: $2\ O^{-II}H^{+I} \rightarrow H_2O\ (g) + V_O + O^{-II}$, or in the Kröger-Vink notation water formation reads: $2OH^{\bullet}_{O,s} \rightarrow H_2O(g) + V^{\bullet\bullet}_{O,s} + O^{x}_{O,s}$. Water formation is energetically favorable as long as the energy required for surface vacancy formation is lower than the energy released due to water formation. This energetic situation is encountered in case of the $\sqrt{3}$Cl-($\sqrt{7} \times \sqrt{7}$)R19.1° structure. However, on $\sqrt{3}$Cl-(4 × 4), water production is suppressed, since the CeO_{2-x}(111) surface is already highly reduced, close to Ce_2O_3(111), and therefore the surface vacancy formation energy is too high. Instead for the $\sqrt{3}$Cl-(4 × 4) surface, the formation of H_2 is favorable: $2\ O^{-II}H^{+I} + 2\ Ce^{3+} \rightarrow H_2(g) + 2\ O^{-II} + 2\ Ce^{4+}$, or in the Kröger-Vink notation: $2Ce'_{Ce} + 2OH^{\bullet}_{O,s} \rightarrow H_2(g) + 2O^{x}_{O,s} + 2Ce^{x}_{Ce}$. It becomes evident that H_2 evolution is accompanied by the oxidation of Ce^{3+} to Ce^{4+}. The Ce^{4+} state does not remain located at the surface, but rather migrates via electron hopping (polaron) to deeper layers. Otherwise, the surface structure should have been changed, which is experimentally not observed. This explains also why hydrogen evolution is suppressed for the chlorinated stoichiometric CeO_2(111) surface (cf. **Chapter 4.4**), since no Ce^{3+} sites are available,[31] while hydrogen formation occurs on all reduced CeO_{2-x}(111) surfaces. Moreover, on the stoichiometric CeO_2(111) surface, water is also not formed, but instead, adsorbed H and Cl recombine to desorb as HCl(cf. **Chapter 4.4**). The reason for not forming water is kinetics rather than thermodynamics. In order to form water, hydrogen has to diffuse on the ceria surface, and this diffusion process is activated by 1.8 eV,[31] thus suppressing water formation.

It is also quite surprising that H_2 evolution takes place around the same temperature (T ≈ 600 K) as water formation (cf. **Figure 7.9** and **Figure 7.10**), i.e., substantially lower than the Cl_2 formation temperature (T > ca. 1200 K) (cf. **Figure 7.6**). The temperature of H_2 evolution and therefore the O-H bond strength slightly depends on the degree of reduction *x* of CeO_{2-x}(111), shifting from 635 K to 610 K.

Upon increasing the surface temperature even further to 1400 K, adsorbed chlorine will ultimately desorb: $2\ Ce^{4+} + 2\ Cl^{-}_{vac} \rightarrow Cl_2(g) + 2\ V_O + 2\ Ce^{3+}$, or in the Kröger-Vink notation: $2Cl^{\bullet}_{O} + 2Ce^{x}_{Ce} \rightarrow Cl_2(g) + 2V^{\bullet\bullet}_{O} + 2Ce'_{Ce}$. Thus, Ce^{4+} will be reduced to Ce^{3+}. The adsorption energy of Cl sensitively depends on the degree of reduction *x* of CeO_{2-x}(111), shifting the maximum desorption from 1175 K (weakly reduced: ($\sqrt{7} \times \sqrt{7}$)R19.1°) to 1320 K (strongly reduced: (4 × 4)). The experimentally derived adsorption energies vary therefore by about 12%. This change in adsorption energy is reconciled with the present DFT calculations, indicating that the adsorption energy of the Cl_{vac} species decreases from 2.65 eV ($\sqrt{3}$Cl-(4 × 4)) to 1.87 eV ($\sqrt{3}$Cl-($\sqrt{7} \times \sqrt{7}$)R19.1°). For the $\sqrt{3}$Cl-(4 × 4) surface, the overall process of HCl adsorption followed by formation of H_2 and Cl_2 does not lead to changes in the oxidation state of the cations in CeO_{2-x}(111), while in case of water formation the CeO_{2-x}(111) is further reduced, such as encountered for the $\sqrt{3}$Cl-($\sqrt{7} \times \sqrt{7}$)R19.1° surface. In between, both water and hydrogen are formed, such as for the $\sqrt{3}$Cl-(3 × 3) surface. Altogether, the TPD experiments (cf. **Figure 7.6** and **Figure 7.9**) illustrate how the degree of reduction *x* of bulk CeO_{2-x}(111) affects the reactivity of the surface.

Summary

In order to elucidate the microscopic processes in the “chlorinator”, dedicated single-crystalline $CeO_{2-x}(111)$ model systems with different reduction degrees were saturated with HCl at room temperature and subsequently annealed. Supported $CeO_{2-x}(111)$ films are able to stabilize various ordered vacancy structures upon partial reduction, e.g., $(\sqrt{7} \times \sqrt{7})$R19.1°, (3 × 3), or (4 × 4) with well-defined oxygen defect concentrations.[75,90,102–105]

It was shown that bulk oxygen vacancies need to migrate towards the surface to allow for the formation of a well-ordered $(\sqrt{3} \times \sqrt{3})$R30°-$Cl_{vac}$ chlorine overlayer upon HCl exposure, independent of the specific degree of reduction x of $CeO_{2-x}(111)$. Chlorine preferentially adsorbs in the surface oxygen vacancies $V_{O,s}$ as Cl_{vac} with a binding energy that is about 3 eV stronger compared to the adsorption of Cl on top (Cl_{top}) of the undercoordinated Ce ions on the stoichiometric $CeO_2(111)$ surface.[31] These two surface chlorine species, Cl_{vac} and Cl_{top}, are considered essential reaction intermediates in the Deacon reaction mechanism (cf. **Chapter 5.1**).[16,111]

The annealing step leads to the removal of hydrogen from the surface via water or H_2 formation depending on the reduction degree. However, it is found that the Cl_{vac} species is inactive due to its strong binding energy. The chlorinated yet reduced $(\sqrt{3} \times \sqrt{3})$R30°-$Cl_{vac}$ surface acts as dedicated model system for the “oxidizer” in order to investigate the re-oxidation and de-chlorination of the surface, including activation of oxygen from the gas phase and chlorine in vacancies.

7.2 "Oxidizer": Oxidative De-Chlorination of the Model Catalyst

Introductory Experiment

As a start the re-oxidation of chlorinated $(\sqrt{3} \times \sqrt{3})$R30°-$Cl_{vac}$ surface is investigated *in operando* by annealing the sample in front of the mass spectrometer (MS) in the LEED chamber, while dosing oxygen $p(O_2) = 2 \times 10^{-6}$ mbar. The result of the experiment is shown in **Figure 7.12**.

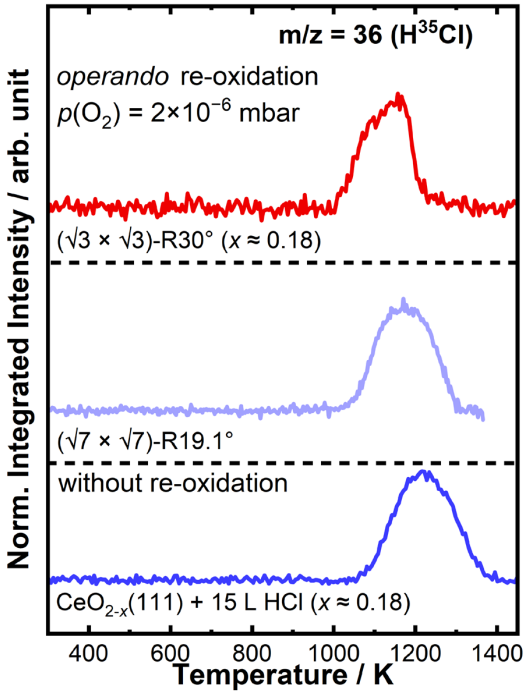

Figure 7.12: Introductory experiment: HCl temperature programmed desorption of similarly prepared $(\sqrt{3} \times \sqrt{3})$R30°-$Cl_{vac}$ CeO_{2-x}(111) surfaces in oxygen $p(O_2) = 2 \times 10^{-6}$ mbar (red) and without re-oxidation. Adapted with permission from reference[2].

It can be seen that the desorption maximum is shifted by ca. 100 K to a lower temperature compared to a similarly prepared sample without re-oxidation, which corresponds to the desorption maximum of a $\sqrt{3}$Cl-$(\sqrt{7} \times \sqrt{7})$R19.1° superstructure, although a shoulder towards lower temperatures is visible and the desorption is finished at lower temperatures. However, the initial desorption starts only at 1000 K being too high to explain and activity at a typical reaction temperature of 700K. However, it is observed that the desorption maximum is shifted to a lower temperature, indicating that a re-oxidation of the surface took place (cf. **Chapter 7.1.1**). In addition, a shoulder towards lower temperatures is visible. A possible explanation is, that the amount of dosed oxygen is not high enough. In an expected activity window for re-oxidation[28] between 500 K and 900 K, only 200 L oxygen are dosed, mainly limited by the maximum pressure limit of the MS detector.

Hence, for the re-oxidation experiments in the "oxidizer" the sample is stepwise oxidized at a fixed temperature. The re-oxidation experiment of the chlorinated CeO_{2-x}(111) mimics the de-chlorination process in **Figure 5.1** (**E-G**) and is carried out stepwise by a specific exposure of O_2 at 700 K followed by a subsequently *in situ* characterization of the sample with NEXAFS and XPS at room temperature. The temperature of 700 K is chosen, to adapt the typical reaction temperature of the ceria-based Deacon process.

7.2.1 Re-Oxidation

Re-Oxidation Experiments of Cl_{vac}-CeO_{2-x}(111): NEXAFS and XPS

In **Figure 7.13** the synchrotron-based NEXAFS Ce $M_{4,5}$ edge (Ce 3d) data in the TEY mode is shown. This detection mode is sensitive to bulk Ce, so that the average Ce^{3+} fraction of the Cl_{vac}-CeO_{2-x}(111) film can be quantified by a linear combination of the reference spectra (cf. **Chapter 6.5.2**).

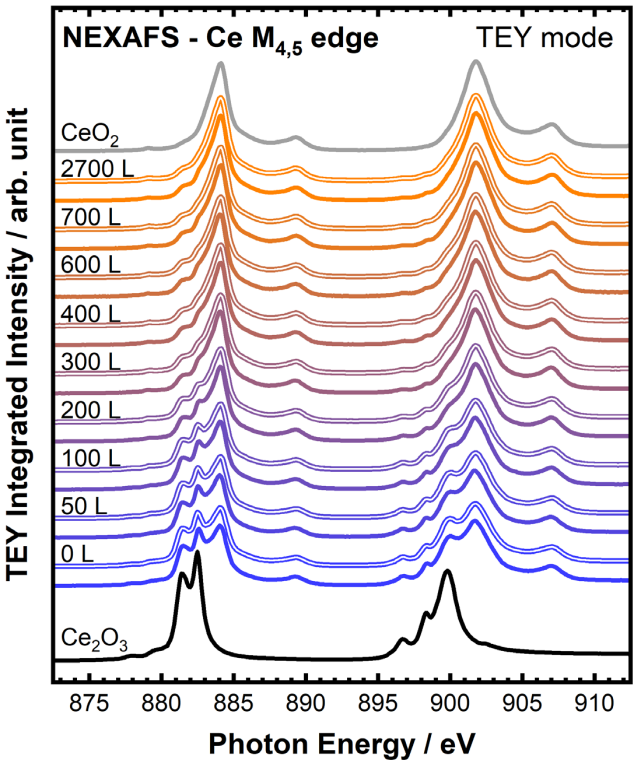

Figure 7.13: Bulk re-oxidation of Cl_{vac}-CeO_{2-x}(111): bulk-sensitive NEXAFS Ce $M_{4,5}$ edge (Ce 3d) data (total electron yield: TEY) after exposing of Cl_{vac}-CeO_{2-x}(111) to various doses of O_2, indicated in Langmuir (L), at 700 K. The reference spectra for fully oxidized CeO_2 and fully reduced Ce_2O_3 serve as references for fitting the NEXAFS data by a linear combination of these reference spectra to determine the bulk Ce^{3+} fraction of Cl_{vac}-CeO_{2-x}(111) after various doses of O_2. The optimized linear combination for each spectrum is shown as thin double line (shifted for clarity reasons) in the same color as the corresponding experimental spectrum. Adapted with permission from reference[2].

The good agreement of these fits can be assessed from inspection of **Figure 7.13**, while the quantified bulk Ce^{3+} fraction as a function of O_2 exposure is compiled in **Figure 7.14** (circles). The bulk Ce^{3+} fraction decreases linearly with O_2 exposure: at first steeply from 38% to 11% upon 300 L of O_2 and then more slowly from 11% to 7% when increasing the O_2 exposure from 300 L to 700 L (and in the end to 5% for 2700 L O_2).

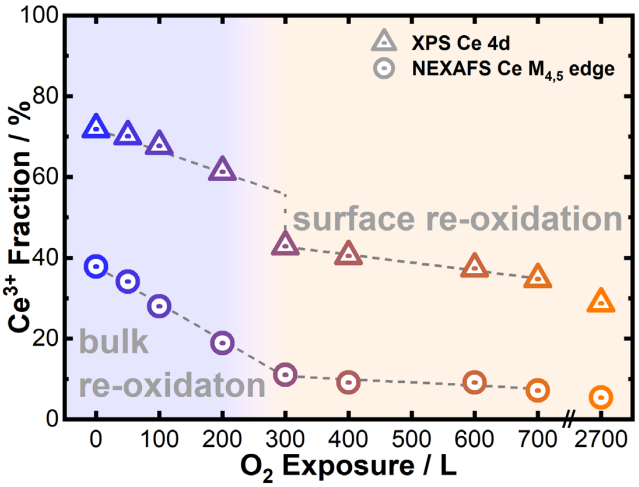

Figure 7.14: Bulk and surface re-oxidation of Cl_{vac}-CeO_{2-x}(111) depending on the O_2 exposure: the bulk Ce^{3+} fraction as derived from NEXAFS (TEY mode, circles) compared to the near-surface Ce^{3+} fraction as derived from XP Ce 4d spectra ($h\nu$ = 250 eV, triangles). The Ce^{3+} fraction is calculated using a linear combination procedure with two reference materials, namely, Ce_2O_3 and CeO_2, as described in **Chapter 6.5.2**. Adapted with permission from reference[2].

While NEXAFS in the TEY mode is bulk-sensitive, XPS measurements of Ce 4d employing a photon energy of $h\nu$ = 250 eV generating photoelectrons with a kinetic energy of $E_{kin} \approx 120$ eV are highly surface-sensitive (the escape depth of such photoelectrons is ~1 nm, cf. **Figure 2.2**).[122] Also the Ce 4d spectra in **Figure 7.15** can be fitted by a linear combination of reference Ce 4d spectra of Ce_2O_3 and CeO_2.

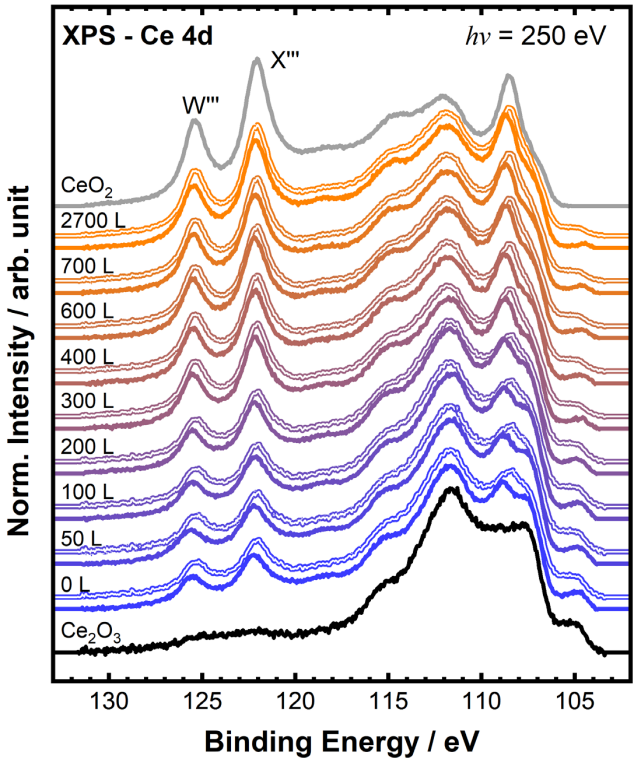

Figure 7.15: Near-surface re-oxidation of Cl_{vac}-CeO_{2-x}(111): Surface-sensitive Ce 4d spectra ($h\nu$ = 250 eV) are shown after exposing Cl-CeO_{2-x}(111) to various doses of O_2 indicated in Langmuir (L) at 700 K. The reference spectra for fully oxidized CeO_2 and fully reduced Ce_2O_3 serve as references for fitting the Ce 4d spectra by a linear combination of these reference spectra in order to determine the near-surface Ce^{3+} fraction. The optimized linear combination for each spectrum is shown as thin double line (shifted for clarity reasons) in the same color as the experimental spectrum. Adapted with permission from reference[2].

Considering the two peaks W''' and X''', assigned to a Ce $4d^9$ O $2p^6$ Ce $4f^0$ final state of Ce^{4+} at $E_{BE} \approx 122–126$ eV,[138,149] the Ce 4d spectra separate into two sets. At low O_2 exposures up to 200 L, the Ce 4d spectra vary only slightly with exposure, from 72% to 61% Ce^{3+}. Between 200 L and 300 L of O_2 an abrupt change in the Ce 4d spectra occurs with a decline of the Ce^{3+} fraction from 61% to 43%. For higher O_2 exposures above 300 L the variation in Ce 4d spectra is small again (43% to 35% Ce^{3+}). This observation is fully reconciled and quantified by the fitting procedure (**Figure 7.15**), whose derived near-surface Ce^{3+} fractions are shown in **Figure 7.14** (triangles). For O_2 exposure below 200 L (**Figure 7.14**, blue background), the fraction of near-surface Ce^{3+} of CeO_{2-x}(111) decreases more slowly than that of bulk Ce^{3+} as derived from the NEXAFS data.

The difference in Ce^{3+} fraction (bulk versus surface) as a function of O_2 exposure (0-200 L of O_2) can be traced to a preferential oxidation of bulk CeO_{2-x}(111), in agreement with previous findings.[28,103] In the O_2 exposure ranging from 200 L to 300 L, the near-surface Ce^{3+} fraction decreases quickly, while the bulk Ce^{3+} fraction (NEXAFS) of the entire film still decreases with the same rate as for lower exposures (**Figure 7.14**, transition blue/orange). This behavior points to a preferential oxidation of the surface region for O_2 exposures of 200 L to 300 L. Above 300 L both bulk and surface region further slowly oxidize with the Ce^{3+} fraction declining more rapidly in the surface than in the bulk region (**Figure 7.14**, blue background). Even after exposure of 2700 L of O_2 the Ce^{3+} fraction in the near-surface region is still 30%, while that of the bulk Ce^{3+} is only 5%. The mechanism for the initial bulk oxidation followed by the surface oxidation will be further discussed together with the DFT+U results.

The O 1s binding energy sensitively depends on the reduction degree x of CeO_{2-x}.[102,150] In **Figure 10.8**a (Appendix) surface-sensitive O 1s spectra ($h\nu$ = 580 eV) are shown depending on the O_2 exposure during re-oxidation. Up to 200 L O_2, a shift by 0.1 eV is observed in the O 1s binding energy, while from 200 L to 300 L, an additional shift of 0.1 eV is visible, remaining nearly constant then for even higher O_2 exposures. In order to resolve this subtle shift in energy, high resolution at FlexPES[21] is mandatory. More bulk-sensitive O 1s spectra are shown in **Figure 10.8**b (Appendix). Here a more continuous shift of the O 1s binding energy is evident, consistent with the NEXAFS experiments shown in **Figure 7.13**

DFT+U Calculations: Activation of O_2 and Re-oxidation Cl_{vac}-CeO_{2-x}(111):

In the following the re-oxidation of the chlorinated surface is studied by DFT+U calculations, for which O_2 needs to be initially activated. These processes are modeled by a Ce_3O_5(111)-(3 × 3) unit cell[151] with a Cl_{vac} coverage of 1/3 and with or without O vacancies in deeper oxygen layers below the surface ($V_{O,SSS}$: V = vacancy, O = oxygen, SSS = sub-sub-surface).

Activation of O_2

For the activation and adsorption of O_2 to occur the presence of a surface oxygen vacancy $V_{O,S}$ is required. O_2 species adsorbing on surface Ce sites are weakly bound by less than 0.4 eV,[152,153] thus being irrelevant for the re-oxidation process studied at 700 K. This is in also agreement with the "oxidation" experiment of the chlorinated stoichiometric CeO_2(111) surface discussed in **Chapter 4.4** (cf. **Figure 4.8**). The formation of a surface

oxygen vacancy at the $3Cl_{vac}$-$Ce_3O_5(111)$-(3 × 3) surface by desorption of molecular oxygen (½ O_2) requires 2.18 eV (Appendix, **Figure 10.13**a+b, no $V_{O,SSS}$ in the slab) and can therefore be safely ruled out at 700 K on the (111) surface. Instead, the diffusion of an oxygen vacancy from a deeper oxygen layer ($V_{O,SSS}$) of $Ce_3O_5(111)$ towards the surface is preferred as summarized in the energy diagram presented in **Figure 7.16**a **(**and **Figure 10.13**d, with one $V_{O,SSS}$ in the slab).

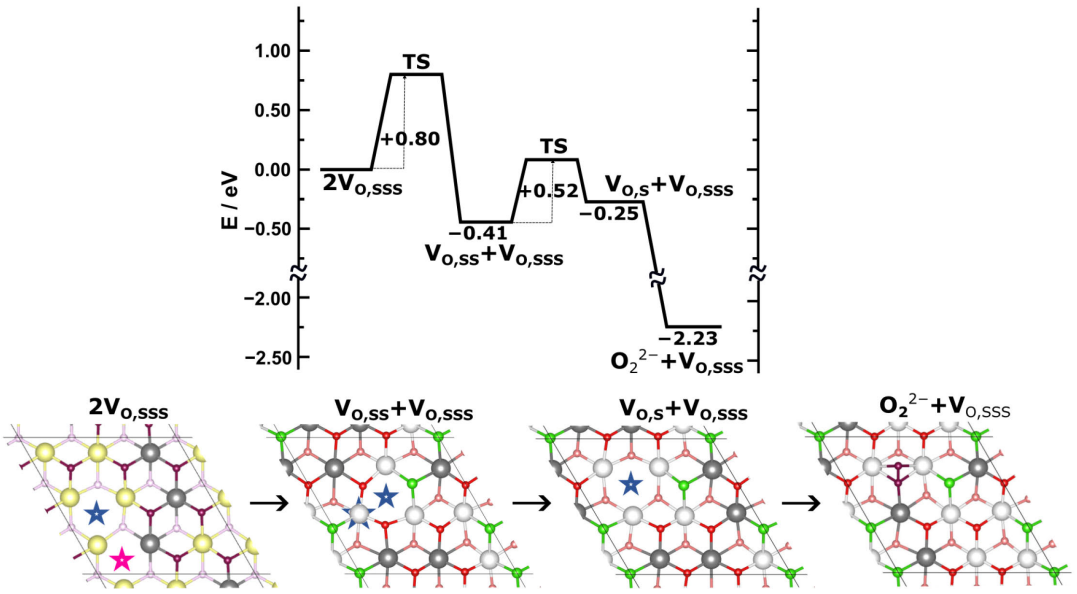

Figure 7.16: Activation of O_2 at $3Cl_{vac}$-$Ce_3O_5(111)$-(3 × 3): a) Energy diffusion path of the oxygen vacancy from the third oxygen layer ($V_{O,SSS}$) to the surface ($V_{O,S}$) of $3Cl_{vac}$-$Ce_3O_5(111)$ and the O_2^{2-} adsorption state on the oxygen vacancy (peroxo species: O_2^{2-}). Color code: Ce^{4+} in the first/second ceria trilayer are white/yellow and Ce^{3+} atoms are gray, the oxygen surface (subsurface) atoms are red (light red), and Cl atoms are green. The blue star indicates the oxygen vacancy diffusing along the pathway, whereas the pink star indicates the fixed $V_{O,SSS}$ vacancy. The energy reference point has been established as the state with two vacancies in the third oxygen layer ($V_{O,SSS}$), $3Cl^-$ adsorbed on surface oxygen vacancies, and O_2 molecules in the gas phase. Adapted with permission from reference[2].

The oxygen vacancy can diffuse towards the surface with an activation energy of 0.80 eV. The subsurface oxygen vacancy ($V_{O,SS}$: SS = sub-surface) is the most preferred site. The surface oxygen vacancy ($V_{O,S}$) is 0.16 eV less preferred than the subsurface vacancy ($V_{O,SS}$) and the activation barrier for an oxygen vacancy to diffuse from the subsurface to the surface is 0.52 eV.[147,151,154] The probability for an oxygen vacancy to be encountered at the surface is given by Boltzmann statistics. For instance, at 700 K, the probability of a surface oxygen vacancy ($V_{O,S}$) is about 7%. Whenever an O_2 molecule from the gas phase strikes a surface oxygen vacancy ($V_{O,S}$) it is strongly adsorbed by about 2 eV in the form of a peroxo species (O_2^{2-}) and pins the vacancy to the surface. The O–O bond length is 144 pm which is in fair agreement with a typical bond length of peroxide groups.[155,156]

The oxidation state of oxygen in chemisorbed O_2 species is determined by several factors, including the number of the remaining Ce^{3+} sites in system after the formation of the adsorbed O_2 species, the O–O bond length, magnetization, and Bader charges. Upon O_2 adsorption, the number of Ce^{3+} is reduced by two per (3 × 3) cell, providing evidence[157] of the formation of a peroxo species O_2^{2-}, with each O in the oxidation state –I. Additionally, the total magnetization of O_2^{2-} is 0.790 μ_B and the Bader charge difference with respect to O_2(gas) is calculated to be 1.23. These values serve as distinguishing indicators

favoring the peroxo (O_2^{2-}) over the superoxo (O_2^-) species (see Appendix, **Figure 10.14** and **Table 10.5**).

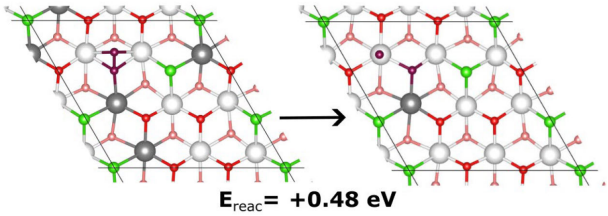

Figure 7.17: "Dissociation of adsorbed peroxo to O_{top} and O_{vac} species." Color code as in **Figure 7.16**. Adapted with permission from reference[2].

The dissociation probability of the peroxo species to form O_{top} and O_{vac} is low, since this process is endothermic by about 0.48 eV (**Figure 7.17**b). Assuming that the entropies of O_2^{2-} and O_{top}/O_{vac} are similar and utilizing the law of mass action, only 2% of the O_2^{2-} are dissociated at 700 K.

Re-Oxidation

The energy profile for the re-oxidation of Cl_{vac}-CeO_{2-x}(111) (cf. **Figure 7.18**) starts from the adsorbed surface peroxo species and assumes the existence of oxygen vacancies in deeper ceria layers ($V_{O,SSS}$ in the slab). If one of these vacancies diffuses towards the surface and the subsurface vacancy ($V_{O,SS}$) is near the peroxo species, dissociation of the peroxo species occurs. This dissociation step is exothermic by 2.41–2.58 eV and is only slightly activated by 0.31–0.68 eV, depending on the local configuration. Two lattice oxygen atoms are formed, thereby annihilating two oxygen vacancies, one on the surface ($V_{O,S}$) and the other in the subsurface ($V_{O,SS}$) underneath. This process reduces the concentration of oxygen vacancies in the near-surface region so that the chemical potential difference drives the diffusion from bulk vacancies to the surface (activation barrier: 0.80 eV), thereby re-oxidizing the bulk of CeO_{2-x}(111).

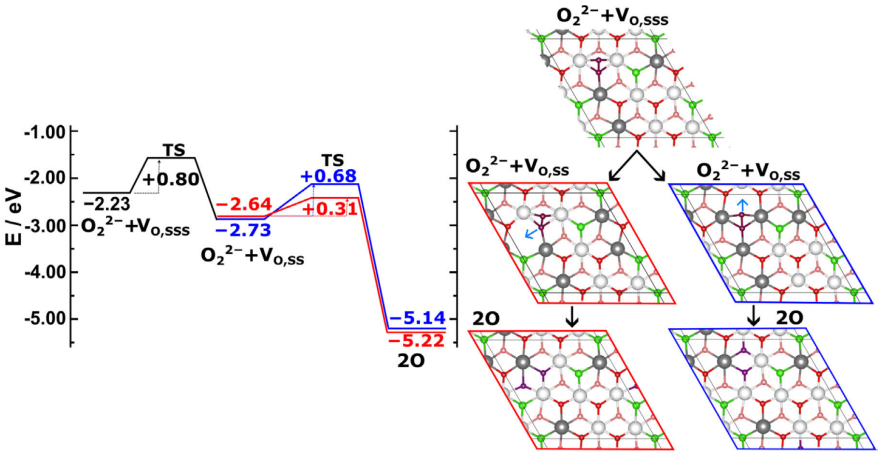

Figure 7.18: Re-oxidation process of $3Cl_{vac}$-Ce_3O_5(111)-(3 × 3). The first step is the diffusion of an oxygen vacancy $V_{O,SSS}$ to form $V_{O,SS}$. Then O_2^{2-} dissociates and fills in the $V_{O,SS}$. Depending on the local configuration this dissociation process is activated by 0.31 eV or 0.68 eV. Color code: Ce^{4+} are white and Ce^{3+} atoms are gray, the oxygen surface (subsurface) atoms are red (light red), and Cl atoms are green. The adsorbed O_2^{2-} is depicted in violet, the blue arrow indicates the movement of the O atom that fills the $V_{O,S}$ upon O_2^{2-} dissociation. The energy reference point has been established as the state with two vacancies in the third oxygen layer ($V_{O,SSS}$), $3Cl^-$ adsorbed on surface oxygen vacancies, and O_2 molecules in the gas phase. Adapted with permission from reference[2].

As interim result it is found that oxygen is activated in oxygen vacancies as peroxo species. Re-oxidation of the surface starts from the bulk and propagates to the surface. Concomitantly with re-oxidation of the surface de-chlorination is observed:

7.2.2 De-Chlorination

In order to monitor the de-chlorination of the surface it is probed with surface- and bulk-sensitive XPS.

XPS Experiments

In **Figure 7.19** the surface-sensitive XP Cl 2p spectra ($h\nu$ = 250 eV) of Cl-CeO_{2-x}(111) exposed to various doses of O_2 at 700 K are summarized. Up to 200 L of O_2 no significant changes are discernible in the Cl 2p spectra (Cl $2p_{1/2}$ and Cl $2p_{3/2}$ at 200.9 eV and 199.3 eV, respectively). That is, the changes are minor as long as the Ce^{3+} fraction in the surface-near region does not change significantly (cf. **Figure 7.14**). For higher O_2 exposures the Cl 2p doublet shifts to lower binding energies by 0.3 eV for the majority species and by 1.0 eV for the minority species (shoulder at 198.3 eV, cf. Appendix, **Figure 10.10**).

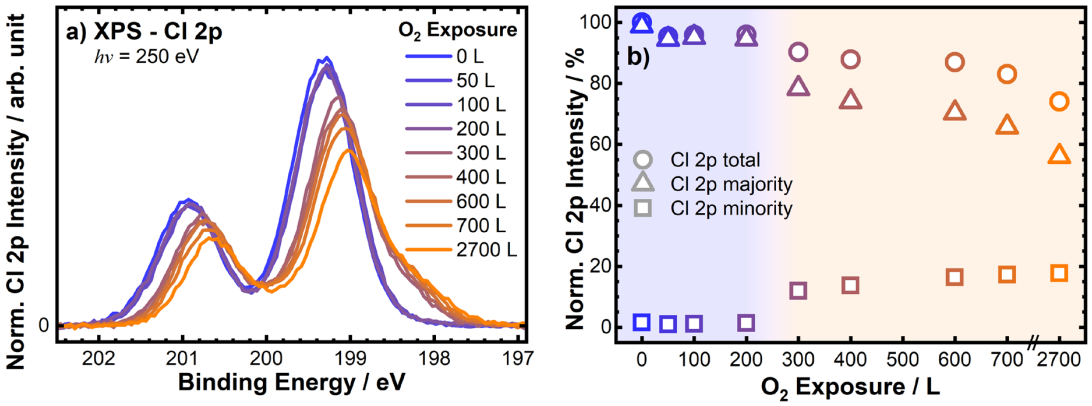

Figure 7.19: De-chlorination experiment: a) Cl 2p spectra ($h\nu$ = 250 eV) after exposing Cl_{vac}-CeO_{2-x}(111) to various doses of O_2 indicated in Langmuir (L) at 700 K. b) Intensity of Cl 2p core level spectra after exposing of Cl_{vac}-CeO_{2-x}(111) to various doses of O_2 indicated in Langmuir (L) at 700 K. Adapted with permission from reference[2].

This abrupt change in the Cl 2p spectra at 300 L coincides with the sudden decrease in the surface Ce^{3+} fraction as indicated in **Figure 7.14**. For a site change the shift in Cl 2p is likely too small, when compared to chlorine adsorption on RuO_2(110), where a site change of Cl from on-top to bridge position leads to a Cl 2p binding energy shift of 1.5 eV(cf. **Figure 3.1**b).[62,146,158] A change in the oxidation state of Cl_{vac} from –I to 0 can clearly be excluded since Cl^- is substantially stronger bound (DFT: 2.65 eV) than Cl^0 (DFT: 0.46 eV) in a vacancy position (cf. Appendix, **Figure 10.9**).

Therefore, the binding energy shift of 0.3 eV for the main peak and 1.0 eV for the shoulder in Cl 2p with respect to the spectrum with 0 L O_2 may be traced to the existence of two different chlorine Cl_{vac} species as a consequence of the re-oxidation of the surface. In **Figure 10.10** (Appendix) the deconvolution of the surface sensitive Cl 2p spectra of Cl_{vac}-CeO_{2-x}(111) in comparison to that after exposing 2700 L of O_2 at 700 K is exemplified. Similar Cl 2p spectra are recorded with $h\nu$ = 850 eV (Appendix, **Figure 10.11**; more

bulk-sensitive), evidencing that both chlorine species are located solely at the surface. In addition, the quantification of chlorine species is not affected by diffraction effects. When increasing the surface temperature from 700 K to 800 K, 900 K, 1050 K, and finally to 1200 K, the Cl 2p spectra in **Figure 10.12** (Appendix) indicate that both Cl species are stable up to 900 K and the minority Cl component desorbs at slightly lower temperatures than the chlorine in the main peak. This indicates a lower thermal stability of the minority species compared to the majority chlorine species.

The evaluation of the total amount of Cl (cf. **Figure 7.19**b) as a function of O_2 exposure at 700 K indicates a ~25% loss of surface chlorine above an exposure of 300 L O_2. Oxygen-induced removal of chlorine is only observed for the majority Cl 2p component, while the minority Cl species once formed is not affected by O_2 exposure above 300 L O_2 and is therefore not relevant for the present de-chlorination step. This finding evidences a higher chemical stability of the minority species with respect to O_2 exposure at 700 K.

TPD Experiments

The loss of 25% Cl may be traced to a destabilization of the chlorine species due to re-oxidation and its partial desorption at 700 K. In **Chapter 7.1.1** (cf. **Figure 7.6**) the Cl-overlayer on CeO_{2-x}(111) was shown to destabilize with decreasing Ce^{3+} fraction of the underlying preformed CeO_{2-x}(111) thin film of ~80% to ~40% ($0.4 < x < 0.2$). Therefore, in **Figure 7.20** lab-based Cl_2 thermal desorption spectra (monitored as $HCl^{28,31}$) of Cl_{vac}-CeO_{2-x}(111) , identically prepared as at the beamtime with ~37% Ce^{3+} fraction (w.r.t. to NEXAFS Ce^{3+} fraction) are compared before and after re-oxidation.

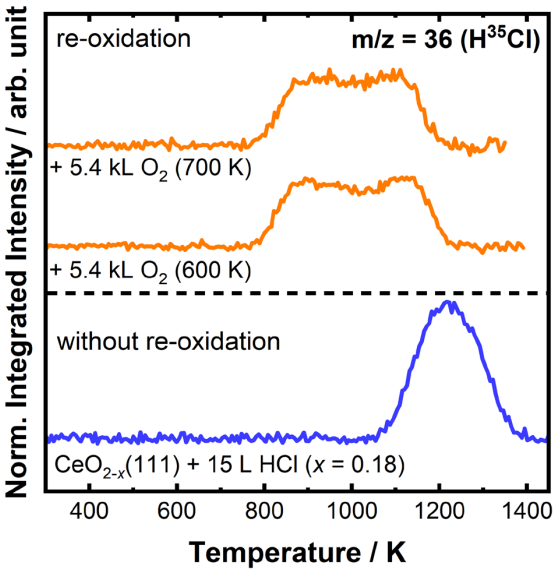

Figure 7.20: HCl temperature programmed desorption of a saturated Cl overlayer on CeO_{2-x}(111) surfaces before and after re-oxidation (2700 L O_2) at 700 K and 600 K. Adapted with permission from reference[2].

It is clearly indicated that re-oxidation of the chlorinated CeO_{2-x}(111) substantially shifts the desorption temperature of chlorine to lower temperatures, i.e., the adsorbed chlorine is significantly destabilized by the re-oxidation process. However, these experiments also show that the loss of 25% of Cl cannot be explained by this destabilization effect, since the desorption onset occurs at a temperature of 800 K (cf. **Figure 7.20**) which is

significantly higher than 700 K. Therefore, the O_2-induced removal of Cl_{vac} is caused by a surface reaction rather than a simple desorption process.

The broad feature of Cl_2 in TPD (**Figure 7.20**) of re-oxidized Cl_{vac}-CeO_{2-x}(111) from 800 K to 1200 K may be traced to a varying Ce^{3+} fraction near the surface. During Cl_2 desorption two oxygen vacancies are left on the surface so that the number of near-surface Ce^{3+} sites increases by two per Cl_2, which leads to stronger Cl bonding resulting in the broad feature in Cl_2-TPD (cf. **Figure 7.20**), consistent with previous DFT calculations.[1]

DFT+U Calculations: De-Chlorination of Cl_{vac}-CeO_{2-x}(111)

In order to model the de-chlorination process with complementary DFT+U calculations, an adsorbed surface peroxo species with the presence of an oxygen vacancy in deeper ceria layers, specifically one $V_{O,SSS}$ within the slab, is considered. This corresponds to the final state shown in **Figure 7.16**, after adsorption of one O_2^{2-}. Subsequently, the process outlined in **Figure 7.16** is repeated, which involves the migration of the $V_{O,SSS}$ vacancy towards the surface, followed by the adsorption of an O_2^{2-} species. This establishes the initial state (1) in **Figure 7.21**, wherein there is no $V_{O,SSS}$ vacancy within the slab. The energy of the initial state (**Figure 7.21**, (1), –4.32 eV, two peroxo) approximates two times (–2.23 eV, one peroxo), as indicated in the last state of **Figure 7.16**.

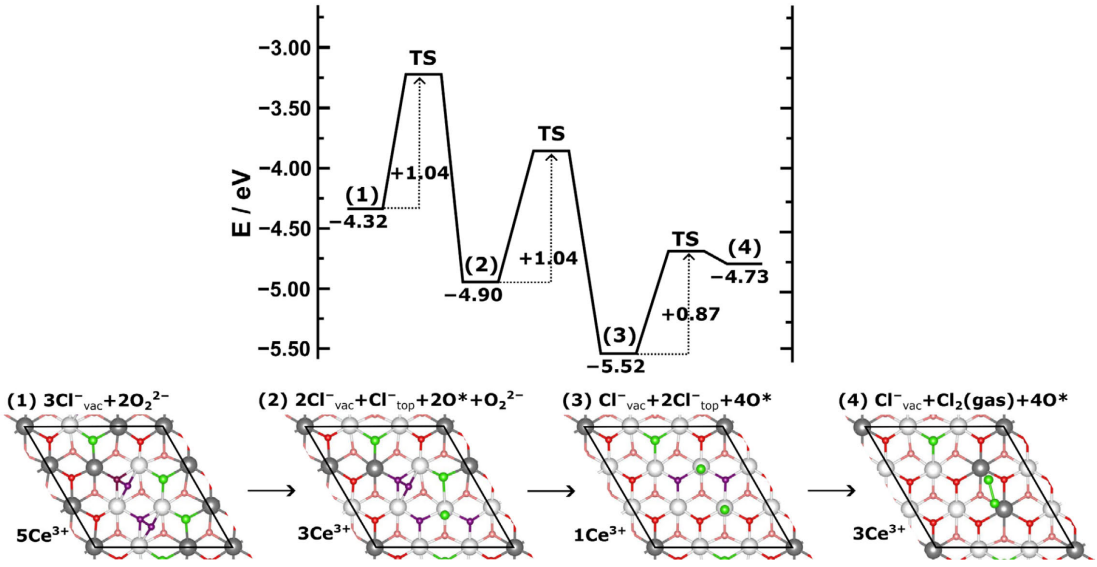

Figure 7.21: De-chlorination process of $3Cl_{vac}$-Ce_3O_5(111)-(3 × 3). Two peroxo species at the surface displace Cl_{vac} to Cl_{top}. This concerted process is activated by 1.04 eV and is exothermic by 0.6 eV. Subsequently, the two Cl_{top} species recombine to form the desired product Cl_2. Color code: Ce^{4+} are white and Ce^{3+} atoms are gray, the oxygen surface (subsurface) atoms are red (light red), and Cl atoms are green. The adsorbed O_2^{2-} species are depicted in violet. O* indicates the lattice oxygen atoms that forms after O_2^{2-} dissociation. The energy reference point has been established as the state with two vacancies in the third oxygen layer ($V_{O,SSS}$), $3Cl^-$ adsorbed on surface oxygen vacancies, and O_2 molecules in the gas phase. Adapted with permission from reference[2].

Afterwards the displacement step of Cl_{vac} to Cl_{top} can be considered, a process that is shown to be induced by the peroxo species at the surface. As soon as the peroxo species is in the proximity of a Cl_{vac} species, the dissociation of the O_2^{2-} species leads to the displacement of Cl_{vac} to Cl_{top} which is exothermic by 0.60 eV with an activation barrier of 1.04 eV. This concerted process is shown as movie frames in the supporting information (cf. Appendix, **Figure 10.15**). If it is not close to Cl_{vac}, the peroxo species needs

to diffuse along the surface to approach Cl_{vac}. In this diffusion process[152] the upper O atom of the peroxo species hops to a neighboring lattice O site forming a new peroxo species with a barrier of 1.23 eV (**Figure 7.22**, no $V_{O,SSS}$ in the slab). Both barriers can readily be overcome at 700 K. If more than two Cl_{top} species form at the surface, they can recombine and the Cl_2 is released directly into the gas phase. According to DFT calculations this association step of two Cl_{top} is activated by 0.87 eV and is endothermic by 0.79 eV (cf. **Figure 7.21**).

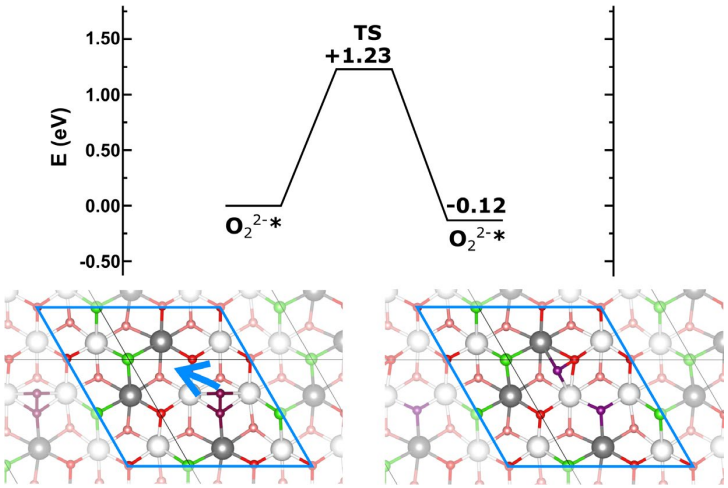

Figure 7.22: Energy diagram and pathway (DFT calculation) for surface diffusion of an O atom of the O_2^{2-} species to form another O_2^{2-} species. Adapted with permission from reference[2].

XPS: Removal of Cl_{vac} by Exposure to Atomic O at 300 K and O_2 at 500 K

The low activation energies found by DFT calculations suggest that partial removal of Cl_{vac} should even occur at lower temperature than 700 K, for instance 500 K. A corresponding set of experiments is presented in **Figure 7.23**a. Also at 500 K the Cl 2p signal decreases with O_2 exposure to 75% of the original intensity, although approximately 10 times higher O_2 doses are needed in comparison with re-oxidation at 700 K. This can be explained due to both the formation of surface vacancies and the displacement reaction are activated by 0.80 eV and 1.04 eV, respectively (cf. **Figure 7.18** and **Figure 7.21**).

In order to stabilize the peroxo species upon O_2 exposure, the presence of oxygen vacancies at the surface ($V_{O,S}$) is required. Since the concentration of surface oxygen vacancies after bulk re-oxidation of Cl_{vac}-CeO_{2-x}(111) is very low, the peroxo species remains a kind of "ghost species" that is present only in spurious amounts, and it is easily consumed by re-oxidation and the displacement reactions. However, the peroxo species can be generated in an alternative way, by exposure to atomic oxygen O.[159]

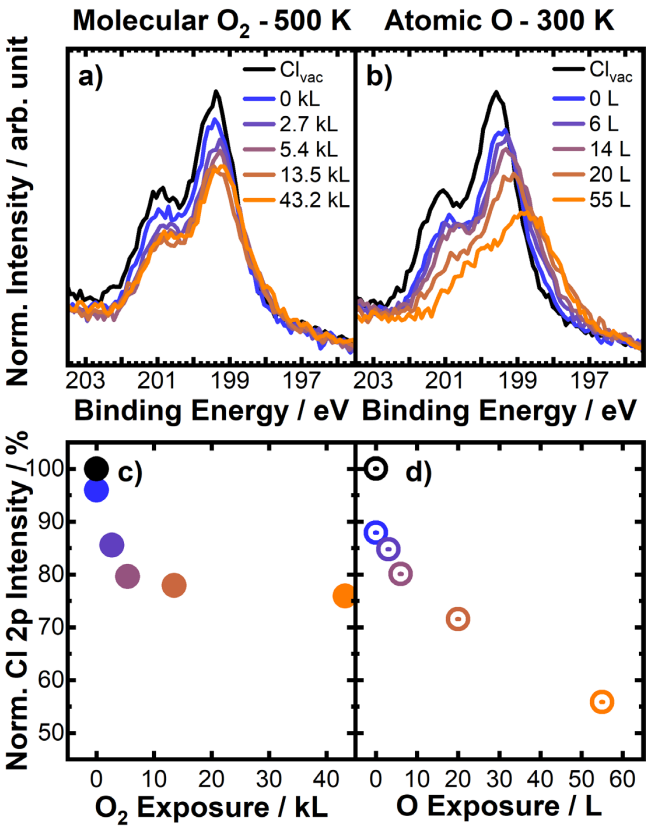

Figure 7.23: Cl 2p lab-based XP spectra: a) de-chlorination and re-oxidation at 500 K with 43.2 kL O_2. b) de-chlorination and re-oxidation at 300 K with 55 L of atomic O, c) and d): integrated intensity of the Cl 2p peak of a) and b), respectively. The exposures in panel c) are given in kL. Detector angle $\theta = 60°$ for enhanced surface sensitivity (cf. **Figure 2.3**). Adapted with permission from reference[2].

At room temperature, surface lattice O^{2-} sites can be transformed to O_2^{2-} by adsorption of atomic oxygen, without changing the oxidation state of Ce. Of course, atomic oxygen can also adsorb on surface Ce sites, but this adsorption process is less favorable by 0.48 eV than the adsorption on surface lattice O followed by the formation of O_2^{2-} (cf. **Figure 7.17**b). The peroxo species in turn induces the shift of Cl_{vac} species from the vacancy position to the top position Cl_{top}, where chlorine can subsequently recombine and desorb from the surface as Cl_2. In this way, part of the Cl_{vac} at the surface can be removed by exposing the re-oxidized Cl_{vac}-CeO_{2-x}(111) surface to atomic oxygen at 300 K. This process is monitored by the Cl 2p signal in **Figure 7.23**b showing that low exposures of ~50 L O are sufficient to remove half of the surface Cl_{vac} species. This, in turn, corroborates the preferential formation of the peroxo species and its important role in the $Cl_{vac} \rightarrow Cl_{top}$ displacement reaction. The peroxo species on the stoichiometric CeO_2(111) can also be verified in the O 1s spectrum (surface-enhanced, $\theta = 60°$) (**Figure 7.24**). The O 1s component at 531.3 eV can be discriminated from the OH species at 532.2 eV (cf. **Figure 7.10**), and according to a recent XPS study the high-energy component was assigned to the peroxo species based on DFT-derived binding energy shifts.[159]

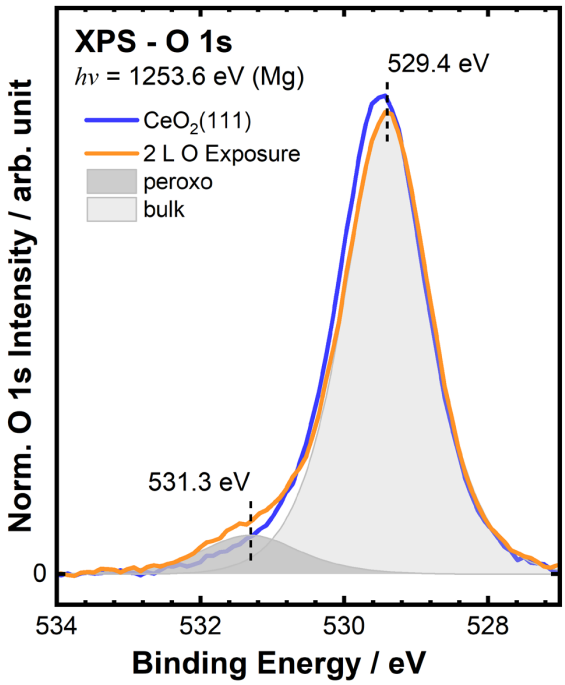

Figure 7.24: O 1s lab-based XP spectra with a spectral feature of the O_2^{2-} species of $CeO_2(111)$ when exposed to 2 L of atomic oxygen O at room temperature. Detector angle $\theta = 60°$ for enhanced surface sensitivity. Adapted with permission from reference[2].

As interim result it can be concluded that, after re-oxidation of the bulk, the Cl_{vac} is activated by adsorbed oxygen in form of a peroxo species in a concerted process and a dechlorination of the surface can be observed.

Discussion

Amrute et al.[16] predicted the Cl_{vac} to Cl_{top} displacement (cf. **Figure 5.1**) as critical step in the de-chlorination process of the ceria catalyst. They proposed that one of the oxygen atoms in the subsurface layer can diffuse towards the surface, pushing a Cl_{vac} atom towards the top site on Ce and leaving one oxygen vacancy in the subsurface region. This step has been considered rate-limiting for the Deacon process and is endothermic by 2.15 eV.[16] The following surface re-oxidation step has remained, however, largely elusive and was proposed to be carried out through "a complex diffusion-reaction mechanism"[16] that would be exothermic by nearly 3.4 eV. Altogether, this combined process of oxidative displacement is exothermic by 1.2 eV; a lower energy of 0.53 eV was reported by Wolf et al.[160] consistent with the DFT+U results in **Figure 7.21**.

With a combination of *in situ* synchrotron-based techniques (NEXAFS and XPS) the re-oxidation process is shown to start from the bulk of Cl_{vac}-$CeO_{2-x}(111)$ and then propagates towards the surface. From bulk-sensitive NEXAFS experiments (cf. **Figure 7.13**) the re-oxidation of bulk $CeO_{2-x}(111)$ is shown to proceed almost linearly with O_2 exposure up to 300 L of O_2, and above 300 L the re-oxidation is significantly slowed down. Quite in contrast, the surface-sensitive Ce 4d XP spectra (cf. **Figure 7.15**) indicate only little change of the Ce^{3+} fraction in the surface region up to 200 L of O_2, while suddenly oxidation in the near-surface region is practically completed for the exposure range from 200L up to 300 L. Only during surface oxidation, the Cl 2p spectra (cf. **Figure 7.19**) alter in that the spectral features shift slightly to lower binding energies and the integral

intensity starts to decrease with O_2 exposure. The actual activation step from Cl_{vac} to Cl_{top} is not directly observed. Instead the oxygen-driven removal of Cl_{vac} is monitored with the Cl 2p spectra, i.e. the partial de-chlorination of the Cl_{vac}-CeO_{2-x}(111) surface, by the recombination of Cl_{top} species to form Cl_2 and its instant release to the gas phase at 700 K.

The DFT+U calculations confirm the results of the re-oxidation and de-chlorination X-ray spectroscopy and TPD experiments in the "oxidizer". The most important reaction intermediate for the re-oxidation and de-chlorination of Cl_{vac}-CeO_{2-x}(111) is shown to be a peroxo species (O_2^{2-}) that is stabilized in surface oxygen vacancies by ~2 eV, in agreement with previous theoretical studies.[152,156,161–163] Whenever an additional vacancy appears in the subsurface region directly below the peroxo species, the peroxo species dissociates and replenishes two oxygen vacancies. The activation energy for the bulk re-oxidation is governed by the diffusion barrier of oxygen vacancies from the bulk towards the surface (+0.80 eV), while the activation barrier for the displacement step $Cl_{vac} \rightarrow Cl_{top}$ is +1.04 eV. From this difference in activation energies, the branching ratio at 700 K between these competing reactions is inferred to be about 1:50 in favor of bulk re-oxidation. This is fully consistent with the experimental observation that the Cl 2p XP spectra (cf. **Figure 7.19**) are practically unaltered as long as the bulk CeO_{2-x}(111) is not almost fully re-oxidized (cf. bulk-sensitive NEXAFS **Figure 7.14**).

When the bulk and the near-surface region of CeO_{2-x}(111) are essentially re-oxidized after exposing 300 L of O_2 at 700 K, the lifetime of the adsorbed peroxo species is long enough to induce the competing displacement reaction of $Cl_{vac} \rightarrow Cl_{top}$. Since the surface concentration of oxygen vacancies ($V_{O,S}$) is expected to be small after bulk re-oxidation, only very few peroxo species are formed and, as a consequence, the displacement step $Cl_{vac} \rightarrow Cl_{top}$ is quite slow. The Cl_{top} species is not persistent on the surface since the recombination of two neighboring Cl_{top} species to form Cl_2 gas is activated by only +0.87 eV and proceeds therefore rapidly at 700 K; also considering the entropy gain upon desorption. This explains as well why Cl_{top} cannot be detected in the Cl 2p spectrum (cf. **Figure 7.19**a), thus supporting the interpretation of the observed shift in Cl 2p spectra being due to re-oxidation of the surface-near region. After exposure of 2700 L O_2 the reduction in Cl_{vac} coverage saturates and amounts to 75% (cf. **Figure 7.19**b). A possible explanation is that there are not enough oxygen vacancies available at the surface into which O_2 can adsorb as a peroxo species. This terminates the displacement reaction $Cl_{vac} \rightarrow Cl_{top}$ and the subsequent recombination step of neighboring Cl_{top} species.

A de-chlorination experiment with atomic oxygen O provides indirect experimental evidence for the important role of the peroxo species in the de-chlorination process. Atomic oxygen exposure is able to form peroxo species at the surface without the need of surface oxygen vacancies.[159] The experiments in **Figure 7.23**b indicate that room temperature exposure of ~50 L of atomic oxygen is able to remove 40% of Cl_{vac} from the surface, a larger portion than that achieved by exposure of 2700 L of molecular O_2 at 700 K (25%).

In summary, in the "oxidizer" the proposed most critical step, i.e. the activation of displacing Cl_{vac} towards Cl_{top}, was elucidated. Initially bulk re-oxidation (+0.80 eV) precedes the $Cl_{vac} \rightarrow Cl_{top}$ displacement step (+1.04 eV). Both processes are shown to be

initiated by O_2 adsorption into an oxygen vacancy via the formation of a surface peroxide species (peroxo: O_2^{2-}), while its dissociation is directly coupled with the reoxidation (cf. **Figure 7.18**) and the $Cl_{vac} \rightarrow Cl_{top}$ displacement (cf. **Figure 7.21**). In conclusion, the concerted Cl_{vac} activation step is slightly exothermic by −0.6 eV with an activation energy of only +1.04 eV. Therefore, it is unlikely to be the rate-determining step in the Deacon process on the $CeO_{2-x}(111)$ surface.

8 Concluding Discussion

8.1 Catalytically Active Surface of CeO_{2-x}

The Deacon reaction over CeO_2 exhibits a positive reaction order of O_2 and typically runs under oxidizing reaction conditions, i.e., a ratio of O_2 : HCl > 1:4.[16] Nevertheless, oxidizing reaction mixtures lead to a reduction of CeO_2 yet, so that it can stabilize strongly adsorbing chlorine at the surface.[1,2,21,25,81]

In generalized terms, partial CeO_2 reduction is enabled by HCl adsorbing in an acid-base reaction resulting in OH group formation on surface lattice O and Cl atom adsorption on surface Ce. At sufficiently high temperatures, chlorine atoms are able to recombine, forming Cl_2, whereas neighboring OH groups are able to form water and an oxygen vacancy upon recombination. The formed oxygen vacancy can be occupied either by chlorine upon dissociative HCl adsorption or by oxygen forming a peroxo species. The peroxo species can adsorb at 700 K and the further dissociation of peroxo would need another subsurface O vacancy in its proximity. For kinetic reasons, chlorine adsorption is preferred over peroxo adsorption, resulting in an accumulation of chlorine in surface oxygen vacancies. Ultimately, this will chlorinate the CeO_{2-x} surface, where chlorine is strongly adsorbed in surface oxygen vacancies as Cl_{vac}. However, the underlying reaction mechanism is elusive and investigated in the present thesis.

Previously, the chlorination degree of CeO_2 powder was quantified to be less than 1 ML (ML: monolayer) in an experiment with prompt gamma-ray neutron activation analysis (PGAA)[81] and confirmed by dedicated in situ titration experiments.[1,25] Closer to the present model system are shape-controlled CeO_2 octahedrons exposing (111) facets.[71] After HCl oxidation reaction of CeO_2 nano-octahedrons with an oxidizing reaction feed O_2 : HCl = 2:1 (cf. stoichiometric feed: O_2 : HCl = 1:4), a mean Ce^{3+} fraction of 29% in the near-surface region and a Cl/Ce ratio of 15% was determined.[21] The fresh CeO_2 catalyst possesses a Ce^{3+} fraction of 20%. From these experiments, the chlorine coverage can be estimated to be about 0.4 ML, which would account for 9% of the Ce^{3+}. Each Cl^- needs one Ce^{3+} for charge compensation. Therefore, the residual 20% of Ce^{3+} needs to be compensated by 10% oxygen vacancies. In conclusion, the experiments from CeO_2 powder and shape-controlled CeO_2 nanoparticles render a chlorinated CeO_{2-x}(111) surface with a Cl_{vac} coverage of 1/3 and 10% oxygen vacancies a suitable model system of the catalytically active phase in the Deacon process and for studying the elementary reaction steps

in the chlorination, water formation, re-oxidation, and de-chlorination reaction as part of the Deacon process.[2]

8.2 Consequences for the Deacon Process

"Chlorinator"

From the experiments in the "chlorinator" it can be concluded that the reduced $CeO_{2-x}(111)$ surfaces, with $0.2 \lesssim x \lesssim 0.4$, bind chlorine in the vacancy Cl_{vac} position too strongly (cf. **Figure 7.6b**), thus suppressing evolution of Cl_2 at a reaction temperature of 700 K.[1] In contrast, the stoichiometric oxidized $CeO_2(111)$ surface, with $x = 0$, is also not active in the Deacon process, because surface H and surface Cl recombine to produce HCl that desorbs (cf. **Figure 4.7**).[1,28,31]

Furthermore, water as a byproduct does neither form on the strongly reduced (4 × 4) surface with $x \approx 0.4$ nor on the stoichiometric $CeO_2(111)$ surface with $x = 0$. In the former case, H_2 is formed, while in the latter, H recombines with Cl_{top} species instead of surface O. However, with a decrease in the degree of reduction to $x \approx 0.3$ for the (3 × 3) surface and x ≈ 0.2 for the $(\sqrt{7} \times \sqrt{7})$R19.1° surface, an increase in water formation is observed, which occurs below the Deacon reaction temperature. In conclusion, for the water formation step the $CeO_{2-x}(111)$ surface needs to be partially reduced.[1,28]

Still Cl_2 evolution is suppressed at 700 K and the two surfaces are not active. In conclusion, the catalytically active phase must be between these boundaries of stoichiometric ($x = 0$) and highly reduced ceria ($0.2 \lesssim x \lesssim 0.4$). Most likely ceria CeO_{2-x} must be slightly reduced, with $0 < x \lesssim 0.2$, and both stoichiometric and reduced areas must be present locally on the surface to produce Cl_2 and water as a byproduct.[1,28]

"Oxidizer"

A reduction degree between $0 < x \lesssim 0.2$ is encountered in the "oxidizer" during re-oxidation of the surface. Initially the surface exhibits a reduction degree of $x \approx 0.19$ (38% Ce^{3+} fraction) for the bulk (NEXAFS) and $x \approx 0.36$ (72% Ce^{3+} fraction) for the surface (XPS), yielding an average of $x \approx 0.28$ (55%) corresponding to a chlorinated (3 × 3) surface (cf. **Figure 7.1** and XPS and NEXAFS Results **Chapter 7.1.1**). Upon initial re-oxidation, below 200 L of O_2 a de-chlorination is not observed as bulk re-oxidation prevails. A sudden onset in de-chlorination respectively chlorine formation is observed after a dosage of 300 L of O_2. From this dose the reduction degree *x,* enabling Cl_2 formation through the peroxo species, can be estimated. The corresponding reduction degrees are $x \approx 0.06$ (11% Ce^{3+} fraction) for the bulk (NEXAFS) and $x \approx 0.22$ (43%) for the surface (XPS), yielding an average of $x \approx 0.14$ (27% Ce^{3+} fraction) which is in good agreement with the reported 29% Ce^{3+} fraction (lab-based XPS) reported by Li et al.[21] for nano-octahedrons exposing the (111) facet (cf. **Chapter 8.1**).

The reason for the observed de-chlorination and activity of the surface can be attributed to the formation of a peroxo species at the surface activating Cl_{vac} in oxygen vacancies and leading towards the formation of Cl_2. The activation process is summarized in **Figure 8.1** including re-oxidation and de-chlorination as shown in **Chapter 7.2** (cf. **Figure 7.16**

and **Figure 7.21**). Initially, three chlorine atoms reside in oxygen vacancies, while two vacancies are located in deeper layers (2 $V_{O,SSS}$) and two oxygen molecules O_2 are in the gas phase. One V_O diffuses to the surface (white background, cf. **Figure 7.16**) upon which an oxygen molecule from the gas phase adsorbs forming a peroxo species. Afterwards, the second V_O diffuses to the surface (green background, cf. **Figure 7.16**) enabling the adsorption of a second oxygen molecule and forming a second peroxo species. Subsequently, each peroxo species can displace one Cl atom in an oxygen vacancy in a concerted reaction leading to the formation of two Cl_{top} species which can recombine and form the desired product Cl_2. The re-oxidation and de-chlorination processes are shown to be exothermic and likely to take place, as the maximum activation barrier is around +1.0 eV which can be overcome at the typical reaction temperature of 700 K (**Figure 7.19**) or even 500K (**Figure 7.23**). However, during re-oxidation with molecular oxygen a maximum de-chlorination of 25% is observed at both temperatures. This is attributed to missing oxygen vacancies at the surface $V_{O,S}$ (cf. **Chapter 7.2.2**) which might be the actual bottle neck for the Deacon reaction on $CeO_{2-x}(111)$ as discussed in the next chapter.

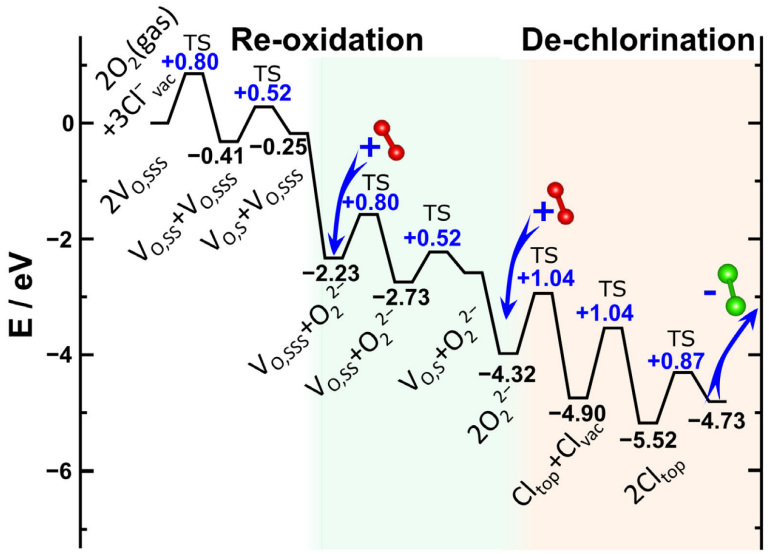

Figure 8.1: Summary of the activation of O_2 on and the re-oxidation and de-chlorination process of $3Cl_{vac}$-$Ce_3O_5(111)$-(3 × 3) as shown by DFT+U calculations: initially, an oxygen vacancy diffuses from the third oxygen layer ($V_{O,SSS}$) to the surface ($V_{O,S}$) of $3Cl_{vac}$-$Ce_3O_5(111)$ upon which O_2 adsorbs forming a peroxo species O_2^{2-} (white background). This process is repeated with a second oxygen vacancy diffusing from the third oxygen layer ($V_{O,SSS}$) (green background). Finally, the two peroxo species at the surface displace Cl_{vac} to Cl_{top} in a concerted process, activated by 1.04 eV and exothermic by 0.6 eV. Subsequently, the two Cl_{top} species recombine to form the desired product Cl_2. The energy reference point has been established as the state with two vacancies in the third oxygen layer ($V_{O,SSS}$), $3Cl^-$ adsorbed on surface oxygen vacancies, and two O_2 molecules in the gas phase. The figure is a courtesy of Pablo G. Lustemberg.

8.3 Proposed Reaction Mechanism Revised

Relevance of the Proposed Peroxo Mechanism

In the present thesis it is shown that the activation of chlorine by an oxygen surface vacancy is not the rate-determining or most energy-demanding step[16] as it proceeds in a concerted reaction via displacement of a peroxo species with a maximum activation

barrier of around 1 eV. Although this activation step is the key finding of the "oxidizer" and an important building block in the reaction mechanism on the $CeO_{2-x}(111)$ surface, it needs to be further investigated whether this activation mechanism is the only one responsible for the activity of the surface.

Considering the reaction equation ($4\ HCl + O_2 \rightarrow 2\ Cl_2 + 2\ H_2O$) of the Deacon process and the re-oxidation mechanism summarized in **Figure 8.1**, it can be concluded that for the formation of two chlorine molecules Cl_2 in total four oxygen molecules O_2 need to be activated, resulting in a annihilation of eight oxygen vacancies and finally in an oxidation of the catalyst. Therefore, the sustainable supply respectively formation of oxygen vacancies at the surface is essential.

Based on this, the following preliminary considerations can be made: either there must be an underlying mechanism suppling oxygen vacancies from the bulk or there must be an additional chlorine evolution mechanism at the surface which forms chlorine already during the adsorption of HCl and lead to additional oxygen vacancies due to water formation: $2\ CeO_2 + HCl \rightarrow 2\ Ce_2O_3 + Cl_2 + H_2O$.

The latter situation is encountered in **Chapter 4.4** on the stoichiometric $CeO_2(111)$ surface, as it was shown that HCl formation is preferred over Cl_2 formation. However, it might possible that a peroxo induced Cl_{top} species reacts with another Cl_{top} species from a dissociated HCl molecule on the surface leading to the formation of Cl_2 and leaving an OH group behind. This step is encountered in the proposed reaction mechanism (cf. **Figure 5.1**, F → G). Afterwards, another HCl molecule is adsorbed forming water with the hydroxyl group and Cl_{top} (cf. **Figure 5.1**, A → B). The water can desorb from the surface by being replaced with the Cl_{top} species in a concerted reaction forming Cl_{vac} (cf. **Figure 5.1**, B → C). The Cl_{vac} species could be activated again by a peroxo species, thus restarting the cycle. This reaction mechanism corresponds to the mechanism depicted in cf. **Figure 5.1** whereas instead of adsorption of ½ O_2 the Cl is activated in a concerted process by the peroxo species. However, in this proposed mechanism there is yet missing the oxygen vacancy which activates O_2 from the gas phase to form the peroxo species. The formation of the oxygen vacancy has already been a crucial point in the original publication by Amrute et al. and motivates further experiments.

The ideal case for the investigation of the influence of oxygen vacancies would be a $CeO_{2-x}(111)$ where the reduction degree could be changed *operando*. A dedicated experiment to govern and investigate the amount of oxygen vacancies at the surface is the construction of a so-called electrochemical pumping cell adapted from Chueh et al.[164–166] schematically depicted in **Figure 8.2**.

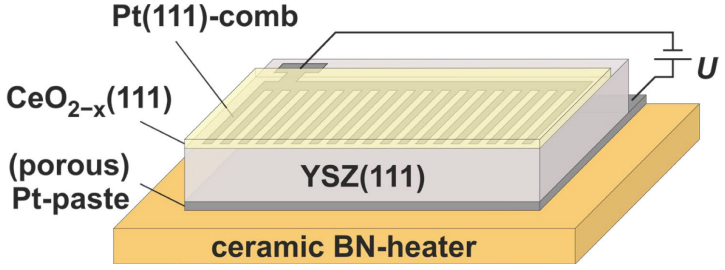

Figure 8.2: Electrochemical pumping cell. Two platinum electrodes are attached to a Yttria-stabilized zirconia YSZ(111) crystal in form of a "comb" on top and porous platinum paste below. A $CeO_{2-x}(111)$ film is prepared on YSZ(111) single crystal covering the Pt-"comb". The whole cell is mounted on top of a ceramic boron nitride heater.

Instead of a CeO_{2-x}(111) thin film on Ru(0001), the film is prepared on single-crystalline yttria-stabilized zirconia YSZ(111).[91] The YSZ single crystal is enclosed between two Pt electrodes allowing for pumping of oxygen in and out of the CeO_{2-x}(111) film on top, via the application of a voltage *U*. The system is heated to the process temperature by a ceramic boron nitride heater. With this setup it might be possible, for example, to repeat the re-oxidation experiment of the oxidizer. Via pumping, oxygen vacancies might be created enabling the formation of peroxo species and a reactivation and de-chlorination of the CeO_{2-x}(111) surface.

8.4 Peroxo Species is Essential for Oxidation Catalysis over CeO_2

The ability to remove/uptake oxygen from the lattice while maintaining structural integrity endows ceria with unique properties in catalysis science and technology.[35,70] The mass-specific amount of oxygen that can be exchanged with the oxide catalyst is called the oxygen storage capacity (OSC).[167,168] The O_2 incorporation requires two oxygen vacancies and electrons supplied from the oxidation of Ce^{3+}.[72] Frequently, the OSC serves as a simple descriptor for the activity in oxidation catalysis of reducible oxides.[111,134,169–172] Oxygen vacancies are considered mandatory for catalysis on ceria.[173–175]

Based on previous spectroscopic experiments on CeO_2 powders[176–181] and CeO_{2-x}(111) platelets,[163] superoxo and peroxo species have been identified and assumed to play an important role in the oxidation chemistry of ceria. In **Chapter 7.2.1** it was shown that the adsorption energy of the peroxo species at oxygen vacancies of CeO_{2-x}(111) is quite high (~2 eV). Therefore, the peroxo species is quite persistent on the surface even at high temperatures of 700 K. For the re-oxidation of CeO_{2-x}, it was shown that two neighboring surface oxygen vacancy sites for direct O_2 dissociation are not required.[72] Instead, the re-oxidation process can take place in two consecutive steps, namely the activation of O_2 gas to form the peroxo species at the surface oxygen vacancy $V_{O,S}$ and its dissociation as soon as another subsurface oxygen vacancy approaches the peroxo species. Therefore, the peroxo species is mandatory for the oxygen storage capacity (OSC).[167,168]

For comparison, a recent study demonstrated by a combination of infrared vibrational spectroscopy and DFT calculations[162] that the activation of O_2 at vacancies on single-crystalline CeO_{2-x}(100) and CeO_{2-x}(110) takes place via peroxo and superoxo species, but not on CeO_{2-x}(111). The main reason for this apparent discrepancy with the present results is the low adsorption temperature of 110 K in Ref.[162] For such low temperatures, oxygen vacancies of CeO_{2-x}(111) are frozen in the subsurface region and are not accessible to O_2 adsorption from the gas phase. In the present thesis O_2 adsorption takes place at higher temperatures and therefore oxygen vacancies, although with low concentration, are available on the surface of CeO_{2-x}(111).

The peroxo group can diffuse across the (111) surface. In fact, not the whole peroxo species diffuses, but rather the upper oxygen atom of O_2^{2-} diffuses to the neighboring surface lattice O site and transforms it into another peroxo species. With an activation energy of 1.2 eV, this barrier can easily be overcome at 500−700 K, making the peroxo species a mobile surface species (cf. **Figure 7.22**). This structure diffusion process is reminiscent of the diffusion of protons in water (Grotthuss mechanism). For supported catalysts with CeO_2 being the carrier, the mobility of this peroxo species allows facile oxygen exchange between the catalytically active particle and the CeO_2 support in the form of spillover and back-spillover species.

Superoxide (superoxo: O_2^-) and peroxide (peroxo: O_2^{2-}) are known to be important oxygen species in catalytic oxidation reactions[182,183] on ceria-based catalysts that were studied both experimentally and theoretically (see, e.g., Ref.[153,155,156,183–193]). Here, the studies by Pushkarev et al. [178]and Wu et al.[180] who identified the peroxo species via Raman spectroscopy on ceria powder samples and shape-controlled particles, respectively, are emphasized. Additionally, Wan et al.[159] investigated the peroxo species by XPS and DFT+U calculations on the CeO_2(111) surface (cf. **Figure 7.24**).

The peroxo species could be further investigated in dedicated synchrotron-based model studies. As a start the experiment in **Figure 7.24** could be repeated by exposing a pristine CeO_2(111) surface to atomic oxygen, in order to identify the peroxo species via surface-sensitive XPS with high resolution. Spectroscopy of the peroxo species might also bear the possibility to investigate the diffusion of oxygen vacancies to the surface. As a start, a pristine reduced CeO_{2-x}(111) surface is cooled down to low temperatures (e.g. 110 K), at which formation of peroxo species is unlikely. Subsequently molecular oxygen is dosed, while the surface is annealed. Concomitantly the surface is monitored with XPS or NEXAFS, if formation of the peroxo species can be observed, resulting in the re-oxidation of the film.

In the present thesis, the crucial role of the peroxo species in the HCl oxidation reaction during the re-oxidation and de-chlorination process was revealed. The peroxo species induces the displacement of Cl from the vacancy position (Cl_{vac}) towards the on-top position (Cl_{top}) and the subsequent desorption in the form of Cl_2. The concerted displacement of Cl maintains the oxidation state of −1, while the desorption step leads to the oxidation of chlorine towards 0 oxidation state, accompanied with reduction of the catalyst. In general, the concerted displacement of reaction intermediates may be of general importance for oxidation catalysis over ceria.

8.5 Comparison of the Deacon Reaction over $RuO_2(110)$ and $CeO_{2-x}(111)$

Although an understanding of the reaction mechanism up to the level on $RuO_2(110)$ is under research yet, a fundamental comparison of the mechanisms is possible.

Table 8.1: Comparison of the $RuO_2(110)$ and $CeO_{2-x}(111)$ surface in the Deacon reaction.

Surface	$RuO_2(110)$	$CeO_{2-x}(111)$
Structure	2-fold symmetry	3-fold symmetry ($x = 0$)
	Tasker type 2	Tasker type 2
Temperature	"Low" (T < 620K)	"High" (T > 700K)
Stability	Chlorination of bridge rows	Reactivation possible[16,25]
Deactivation	Volatilization (leaching)	Bulk chlorination
Reactor	Isothermal	Adiabatic
Mechanism	Quasi-1D Langmuir-Hinshelwood-like	Mars-van Krevelen-like
	Along Ru_{cus} rows	Across the surface and in bulk
Oxygen Activation	Along Ru_{cus} sites[57]	In oxygen vacancies[2]
Rate-Determining Step	H transfer during H_2O formation[57]	Oxygen vacancy formation?[2] H transfer?[31]

The surfaces of $RuO_2(110)$ (cf. **Figure 3.1**) and $CeO_2(111)$ (cf. **Figure 3.1**) are structurally different. $RuO_2(110)$ exposes a twofold symmetry while $CeO_2(111)$ exposes a threefold symmetry. However, both surfaces are categorized as Tasker type 2 surfaces, meaning they have no dipole moment perpendicular to the surface, while the planes of the surface are not charge neutral. In the Deacon process $RuO_2(110)$ is active and stable at comparably low temperatures (T < 620K), while $CeO_{2-x}(111)$ is active and stable at high temperatures (T > 700K). The stability of $RuO_2(110)$ in the Deacon reaction is ascribed to a chlorination of the bridge rows. However, at too high temperatures volatilization is possible leading to deactivation. Therefore, RuO_2-based reactors are run at isothermal conditions while $CeO_{2-x}(111)$-based ones run at adiabatic conditions. The de-activation of the $CeO_{2-x}(111)$-based catalyst occurs due to bulk chlorination at temperatures too low (T < 660K)[194] or HCl feeds too high ($HCl:O_2$ 4.5:1.5)[25]. However, a reactivation in oxygen-rich streams is possible[16,25] and a volatilization not observed. The reaction mechanism on the $RuO_2(110)$ surface corresponds to a quasi-1D Langmuir-Hinshelwood-like reaction mechanism along the Ru_{cus} rows. The rection mechanism on the $CeO_{2-x}(111)$ surface, on the other hand, rather corresponds to a Mars-van Krevelen mechanism, as water formation and activation of oxygen involves oxygen vacancies at the surface. On the $RuO_2(110)$ surface, molecular oxygen O_2 is activated along the Ru_{cus} sites. The rate-determining step was shown to be the hydrogen transfer within water formation.[57] On the $CeO_{2-x}(111)$ the rate-controlling step is still elusive. The present thesis indicates that it is

not the activation of chlorine by an oxygen vacancy. Instead, it is likely to be the formation of oxygen vacancies, which might be limited by the desorption of water. The latter might also be addressed to the limited diffusion of hydrogen across the surface,[31] thus inhibiting water formation. In summary, the reaction mechanism of the Deacon reaction on CeO_{2-x}(111) differs fundamentally from that of RuO_2(110).

9 Summary and Outlook

In the present thesis the Deacon process was investigated on CeO_{2-x}(111) in dedicated model studies. The basis for the present thesis are the proposed reaction mechanism by Amrute et al. and pioneering model studies within the doctoral thesis of Christian Sack. In a thought experiment, the proposed reaction mechanism was separated into an exothermic chlorination by HCl, forming water ("chlorinator"), and an endothermic oxidative de-chlorination by O_2, forming Cl_2 ("oxidizer"). This separation into partial reactions is used in chemical looping, which was transferred to dedicated model experiments in the "chlorinator" and "oxidizer."

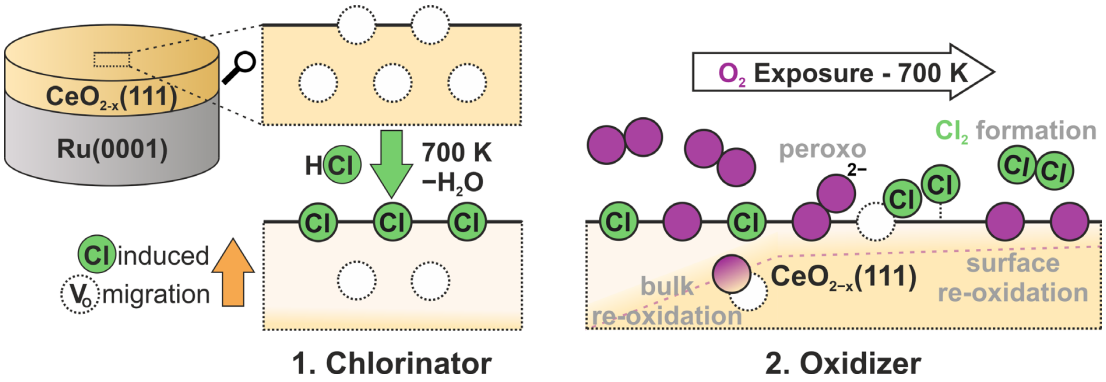

Figure 9.1: Schematic depiction of the chemical looping model experiments in the present thesis. In the "chlorinator", a reduced CeO_{2-x}(111) thin film is initially exposed to HCl at room temperature. Upon annealing to 700K, Hydrogen desorbs in the form of water or hydrogen. At the surface a $(\sqrt{3} \times \sqrt{3})$R30°-$Cl_{vac}$ overlayer structure form with chlorine residing in oxygen vacancies for which migration from the bulk is necessary. Afterwards the chlorinated yet reduced surface is re-oxidized stepwise. It was found that initially the bulk of the film is re-oxidized and only upon surface re-oxidation is a de-chlorination of the surface observed. Both processes are enabled by a peroxo species formed upon adsorption into an oxygen vacancy. Adapted with permission from references[1,2].

"Chlorinator"

Initially the microscopic steps in the Deacon reaction over ceria were studied during chlorination with HCl starting from a reduced CeO_{2-x}(111) surface. The CeO_{2-x}(111) thin film is prepared on a Ru(0001) single crystal via PVD. The thickness, determined by XRR, was in fair agreement with the previous[28] thickness determination by XPS. Depending on the degree of reduction *x,* the reduced CeO_{2-x}(111) surface is able to stabilize various ordered structures, $(\sqrt{7} \times \sqrt{7})$R19.1°, (3×3), or (4×4). Saturating these reduced CeO_{2-x}(111) surfaces with 15 L HCl (or more) led in all cases to the development of a

uniformly covering ($\sqrt{3} \times \sqrt{3}$)R30°-Cl_{vac} overlayer structure upon annealing to 700 K. By LEED fingerprinting, DFT calculations, and XPS, the Cl coverage and the local adsorption geometry of the ($\sqrt{3} \times \sqrt{3}$)R30°-Cl structure on CeO_{2-x}(111) is found to be independent of the original degree of reduction x ($0.2 \lesssim x \lesssim 0.4$). In a dedicated synchrotron beamtime, the ($\sqrt{3} \times \sqrt{3}$)R30°-Cl_{vac} overlayer structure could be reproduced, confirming the lab-based findings.[1,28] DFT+U calculations indicate that chlorine occupies an oxygen vacancy position (Cl_{vac}) with an adsorption energy that is 3 eV higher than that for the stoichiometric CeO_2(111) surface, where Cl resides in an on-top position of surface Ce sites (Cl_{top}). However, the adsorption energy of Cl in the surface vacancy position is too high to explain the Deacon activity at 700 K. The invariance of the ($\sqrt{3} \times \sqrt{3}$)R30°-Cl_{vac} overlayer on CeO_{2-x}(111) with the degree of reduction x requires sufficient mobility of the surface and bulk oxygen vacancies, being one key result of the "chlorinator."[1]

Temperature programmed desorption and temperature-dependent Cl 2p XPS indicate that the adsorption energy of Cl in the oxygen vacancy sensitively depends on the degree of reduction x of CeO_{2-x}(111): chlorine desorption shifts from 1175 K to 1320 K when the degree of reduction x is increased from $CeO_{1.8}$(111) (weakly reduced: ($\sqrt{7} \times \sqrt{7}$)R19.1°) to $CeO_{1.6}$(111) (strongly reduced: (4 × 4)). Also, the formation of the byproduct water critically depends on the degree of reduction x of CeO_{2-x}(111). In the case of a high degree of reduction x, H_2 is formed instead of water, whereas on the stoichiometric oxidized CeO_2(111), H-Cl recombination is observed instead of water formation. However, water formation becomes possible with a decrease in the degree of reduction x such as that of the ($\sqrt{7} \times \sqrt{7}$)R19.1° reconstruction.[1]

In conclusion, in the "chlorinator" the open questions (cf. **Chapter 5.2**) could be answered. In addition to the Cl_{top} species,[31] the Cl_{vac} species[1,28] could be identified and water formation was revealed to be dependent on the degree of reduction. The ($\sqrt{3} \times \sqrt{3}$)R30°-Cl_{vac} overlayer on CeO_{2-x}(111) at the end of the reaction in the "chlorinator" was subsequently moved to the "oxidizer."

"Oxidizer"

The critical reaction step in the HCl oxidation over ceria was predicted to be part of the "oxidizer". Based on a previous DFT study, the displacement step of the Cl_{vac} species towards Cl_{top} was identified,[16] although this displacement step is highly endothermic.[16] Synchrotron-based techniques, including in situ near edge X-ray absorption fine structure (NEXAFS) and in situ high-resolution X-ray photoelectron spectroscopy (XPS), in combination with first principles DFT calculations were employed to elucidate this critical reaction step in the HCl oxidation reaction. A dedicated experiment was designed, modeling the re-oxidation of a ($\sqrt{3} \times \sqrt{3}$)R30°-Cl_{vac} overlayer on the CeO_{2-x}(111) model catalyst at 700 K, a typical reaction temperature for the HCl oxidation. The photon energies in synchrotron-based XPS were carefully chosen in order to be highly surface-sensitive, while Ce $M_{4,5}$ edge NEXAFS (Ce 3d) in the total electron yield mode probed bulk properties. With this combination of surface- and bulk-sensitive methods, it was demonstrated that the re-oxidation of the chlorinated CeO_{2-x}(111) surface at 700 K starts from the bulk

and propagates subsequently towards the surface. The underlying mechanism can be described with complementary DFT+U calculations. The re-oxidation of Cl_{vac}-CeO_{2-x}(111) considerably weakens the adsorption energy of the Cl_{vac} species. Ultimately, part of the Cl_{vac} species is shifted to on-top positions Cl_{top}, where they recombine readily to form Cl_2. Both the re-oxidation of CeO_{2-x}(111) and the $Cl_{vac} \rightarrow Cl_{top}$ displacement step of surface chlorine are predicted with DFT+U calculations to be induced by a previously postulated[28] peroxo species (O_2^{2-}). In this way the displacement step and surface re-oxidation are coupled so that the concerted displacement step becomes exothermic by 0.6 eV with an activation barrier of about ~1 eV. With such a low activation barrier the $Cl_{vac} \rightarrow Cl_{top}$ site change is shown to take place even at 500 K, although requiring a higher O_2 exposure than for the re-oxidation at 700 K. The peroxo species not only impacts the Deacon process, but is also of general importance for catalytic oxidation reactions on CeO_2-supported catalysts. Oxygen spillover effects for supported particles on CeO_2 are intimately correlated with the peroxo species and their facile diffusion across the surface.[2]

In conclusion, it could be shown (cf. **Chapter 5.2**) in the "oxidizer" that oxygen can be activated in surface oxygen vacancies V_O by the formation of a peroxo species, which, in addition to re-oxidation is also responsible for the activation of Cl_{vac} in order to enable Cl_2 formation. It was found that the concerted activation step is not the bottle neck, as discussed in the literature. Instead, the bottle neck may be the supply of V_O at the surface.

Although chemical looping might be challenging for technical application (cf. **Chapter 5.2**), it was shown that the separation into partial reactions allows for valuable insights into the reaction mechanism of the Deacon process over ceria-based catalysts. The peroxo mechanism was identified as an important "building block" of the reaction mechanism. In a next step the chemical looping approach could be adapted to reaction conditions under ambient pressure in a flow reactor.

Chemical Looping under Ambient Pressure

Another possibility is to transfer the chemical looping approach of the present thesis to the flow reactor in the Over research group. In this way, the model experiments of the present thesis can be transferred to ambient pressure conditions. Instead of cycling the catalyst it is also possible to cycle the educt stream.[116] In **Figure 9.2** the graphical abstract of recent publication by Sun et al.[25] is shown, separated into a chlorination ("chlorinator") and oxidation ("oxidizer") step.

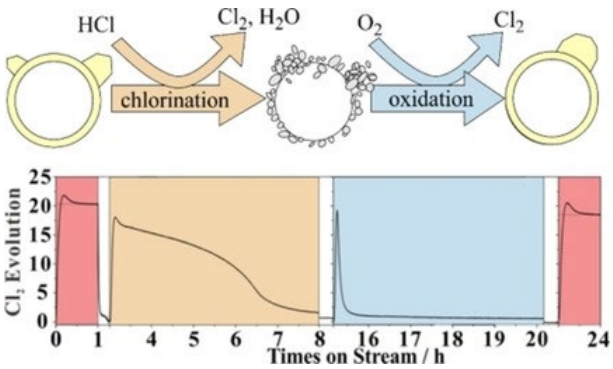

Figure 9.2: Table of contents graphic of a recent publication by Sun et al..[25] The chlorine evolution is monitored as a function of time on stream on a CeO_2-based catalyst (20 mol% of CeO_2 supported on ZrO_2 particles). The reaction mixture is changed from stable mild ($HCl:O_2$ = 1.5:3, red) to deactivating harsh conditions ($HCl:O_2$ = 3:1, orange). These two steps correspond to the chlorination of the catalyst ("chlorinator"). In blue, the re-oxidation and concomitant de-chlorination of the catalyst is shown ("oxidizer"). Afterwards the catalyst is active again under mild conditions. Adapted with permission from reference[25].

In red, a stable operation of the catalyst under mild conditions is observed, whereas harsh conditions lead to a deactivation of the catalyst, due to bulk chlorination. However, by dosage of oxygen the catalyst can be de-chlorinated and re-activated and operates again under mild conditions afterwards.

The model experiments might be transferred to the flow reactor by using CeO_{2-x} octahedrons exposing the (111) facet[21,71]. From re-oxidation of the "mildly" chlorinated catalyst, the actual chlorination degree of the surface might be quantified. This was already investigated by Alexander Spriewald-Luciano in the Over research group in preliminary experiments.

10 Appendix

Parts of the following chapter are based on and adapted with permission from the publications *Dynamic Response of Oxygen Vacancies in the Deacon Reaction over Reduced Single Crystalline CeO_{2-x}(111) Surfaces.* Koller, V.; Sack, C.; Lustemberg, P.; Ganduglia-Pirovano, M.V.; Over, H. *J. Phys. Chem. C* 2022, 126, 13202–13212, reference[1], Copyright © 2022 American Chemical Society and *Critical step in the HCl oxidation reaction over single-crystalline CeO_{2-x}(111): Peroxo-induced site change of strongly adsorbed surface chlorine.* Koller, V.; Lustemberg, P., Spriewald-Luciano, A.; Gericke, S.M.; Larsson, A.; Sack, C., A.; Preobrajenski, A.; Lundgren, E.; Ganduglia-Pirovano, M.V.; Over, H. *ACS Catal.* 2023, *13*, 12994–13007, reference[1,2], licensed under CC-BY 4.0. Copyright © 2023 The Authors, published by American Chemical Society.

10.1 Supporting Information

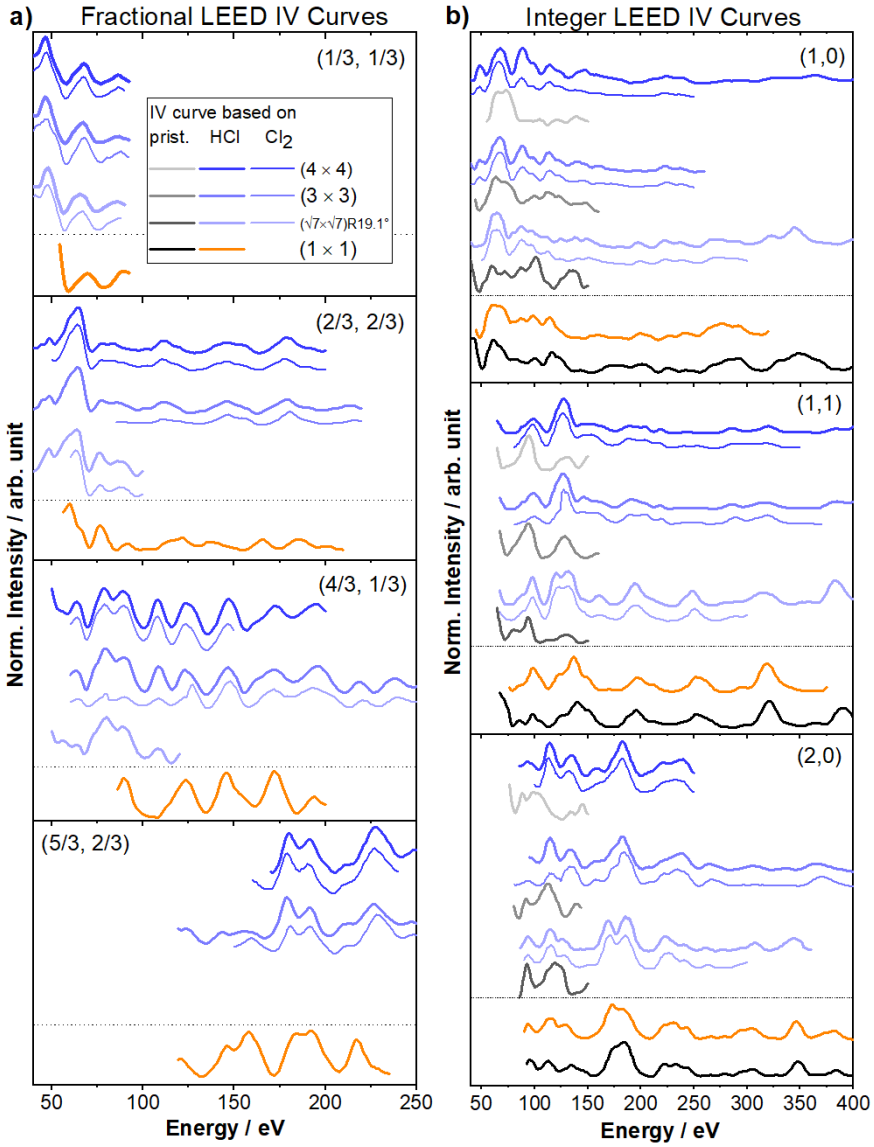

Figure 10.1: a) LEED IV curves (fractional order beams) of (√3 × √3)R30°-Cl phases, prepared from various reduced CeO_{2-x}(111) reconstructed, ordered phases ((√7 × √7)R19.1°, (3 × 3), or (4 × 4)) and stoichiometric CeO_2(111) (1 × 1) after saturation to 15 L (or more) HCl or Cl_2 at 300 K and subsequent annealing to 900 K under UHV conditions. b) LEED IV curves (integer order beams) of the same phases as in a). Adapted with permission from reference[1] and a) from reference.[28]

Quantitative comparison (Pendry R_P-factors) of fractional and integer order LEED IV curves as shown in Figure 10.1.

Table 10.1: Comparison of **fractional** order LEED IV curves between the HCl-induced (√3 × √3)R30°-Cl+H surface structure on stoichiometric CeO_2(111) and HCl-induced (√3 × √3)R30°-Cl_{vac} surface structures on differently reduced CeO_{2-x}(111) surface reconstructions. Adapted with permission from references[1,28].

HCl-induced	vs.	**HCl**- induced	**(1/3, 1/3)**	**(2/3, 2/3)**	**(4/3, 1/3)**	**(5/3, 2/3)**	**Average**
√3Cl-(1 × 1)		√3Cl-(√7×√7)R19.1°	0.72	0.56	0.71	-	**0.66**
√3Cl-(1 × 1)		√3Cl-(3 × 3)	0.44	0.95	0.43	0.74	**0.71**
√3Cl-(1 × 1)		√3Cl-(4 × 4)	0.32	0.96	0.47	0.66	**0.68**

Table 10.2: Comparison of **fractional** order LEED IV curves between Cl_2-induced (√3 × √3)R30°-Cl_{vac} surface structures on differently reduced CeO_{2-x}(111) surfaces among each other. Adapted with permission from references[1,28].

Cl_2- induced	vs.	**Cl_2**- induced	**(1/3, 1/3)**	**(2/3, 2/3)**	**(4/3, 1/3)**	**(5/3, 2/3)**	**Average**
√3Cl-(√7 × √7)R19.1°		√3Cl-(3 × 3)	0.29	0.55	-	-	**0.35**
√3Cl-(√7 × √7)R19.1°		√3Cl-(4 × 4)	0.15	0.41	-	-	**0.25**
√3Cl-(3 × 3)		√3Cl-(4 × 4)	0.14	0.20	0.19	0.20	**0.19**

Table 10.3: Comparison of **fractional** order LEED IV curves between HCl- and Cl_2- induced (√3 × √3)R30°-Cl_{vac} on similar reduced CeO_{2-x}(111) surfaces. Adapted with permission from references[1,28].

HCl-induced	vs.	**Cl_2**-induced	**(1/3, 1/3)**	**(2/3, 2/3)**	**(4/3, 1/3)**	**(5/3, 2/3)**	**Average**
√3Cl-(√7×√7)R19.1°		√3Cl-(√7×√7)R19.1°	0.10	0.16	-	-	**0.13**
√3Cl-(3 × 3)		√3Cl-(3 × 3)	0.24	0.20	0.24	0.33	**0.24**
√3Cl-(4 × 4)		√3Cl-(4 × 4)	0.05	0.13	0.04	0.11	**0.09**

Table 10.4: Comparison of **integer** order LEED IV curves of the pristine surface (reconstructions) on differently reduced CeO_{2-x}(111) surfaces with each other. Adapted with permission from reference[1].

pristine	vs.	**pristine**	**(1, 0)**	**(1, 1)**	**(2, 0)**	**Average**
(√7 × √7)R19.1°		(3 × 3)	0.81	0.36	0.73	**0.58**
(√7 × √7)R19.1°		(4 × 4)	0.94	0.47	1.48	**0.87**
(3 × 3)		(4 × 4)	0.73	0.47	1.00	**0.68**

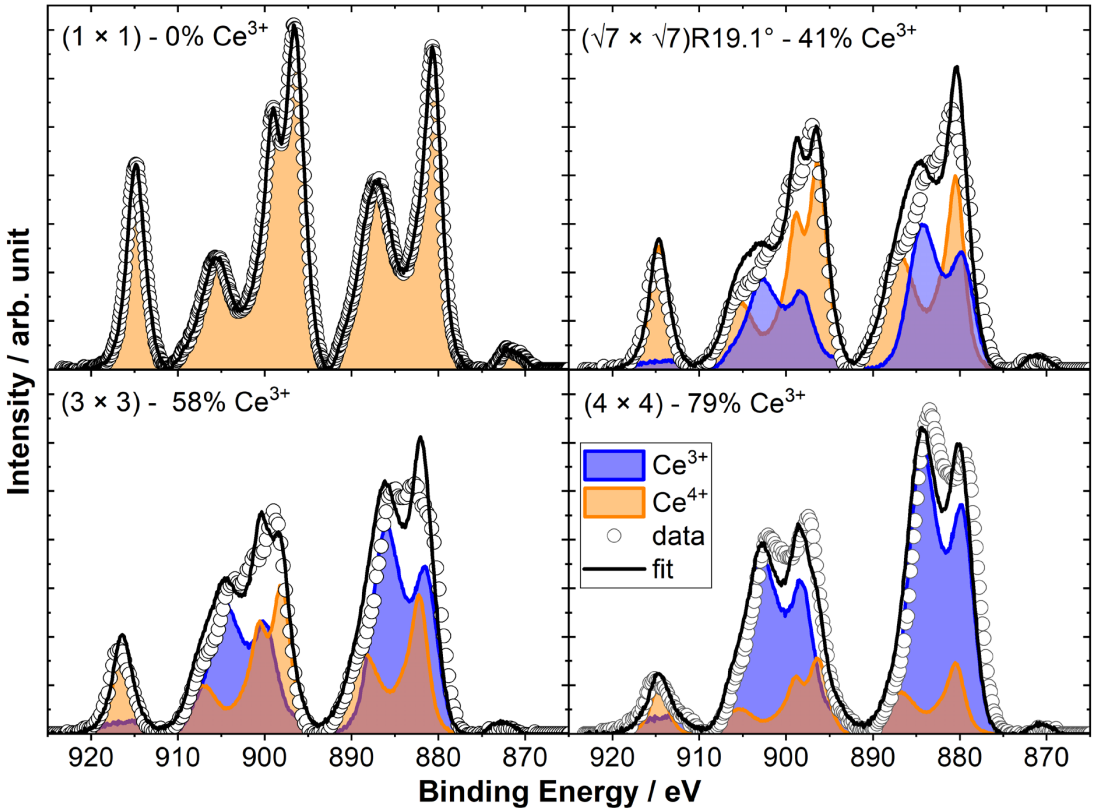

Figure 10.2: Fitting of Ce 3d spectra of CeO_{2-x}(111) (1 × 1): 0% Ce^{3+} ($x = 0$), ($\sqrt{7} \times \sqrt{7}$)R19.1°: 41% ($x = 0.21$), (3 × 3): 58% ($x = 0.29$), or (4 × 4): 79% ($x = 0.40$) by superposition of Ce 3d of fully-reduced Ce_2O_3(111) (blue) and stoichiometric CeO_2(111) (orange). Adapted with permission from references[1,28].

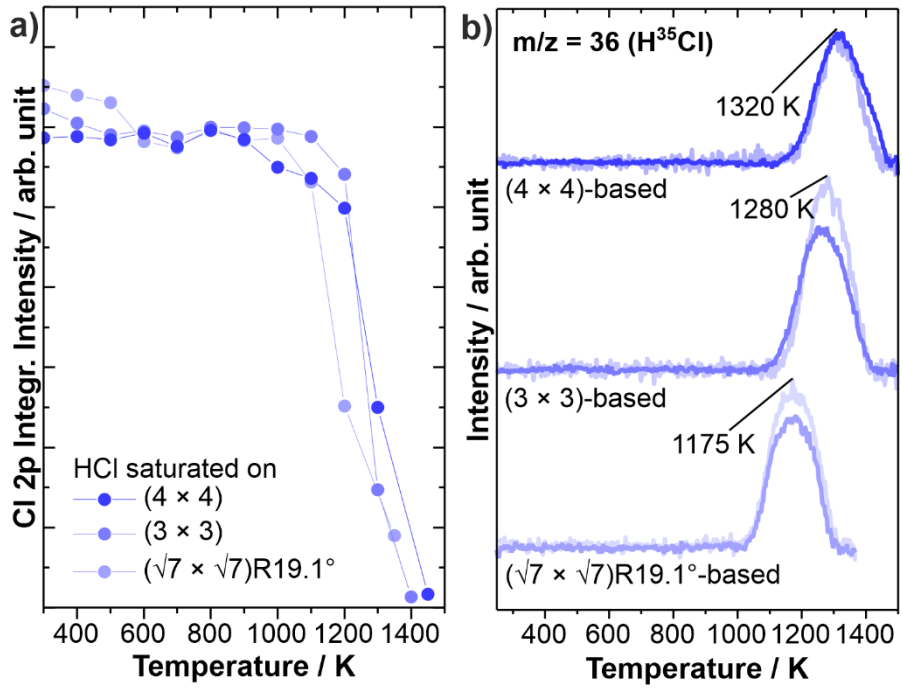

Figure 10.3: a) Cl 2p XP spectra of ($\sqrt{3} \times \sqrt{3}$)R30°Cl_{vac} surface structure upon annealing to various temperatures monitoring the actual Cl-coverage on the surface. b) Temperature programmed desorption comparison of chlorine/Cl, desorbing from at 300K Cl_2- and HCl-saturated (transparent, cf. **Figure 7.6**) reduced CeO_{2-x}(111) surfaces. Adapted with permission from references[1,28].

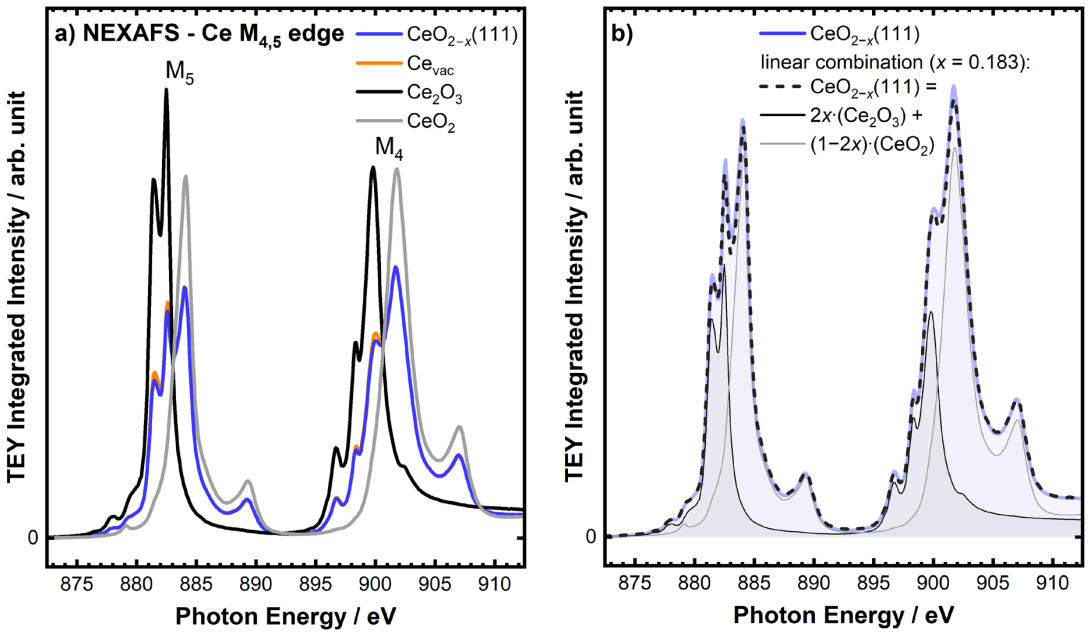

Figure 10.4: a) Bulk-sensitive NEXAFS Ce $M_{4,5}$ edge (Ce 3d) spectra measured in total electron yield (TEY) mode of partly reduced, pristine $CeO_{2-x}(111)$ (blue), chlorinated Cl_{vac}-$CeO_{2-x}(111)$ (orange), fully reduced reference Ce_2O_3 (black) and fully oxidized reference $CeO_2(111)$ (gray). b) Procedure of linear combination for NEXAFS exemplified for pristine $CeO_{2-x}(111)$: NEXAFS ($CeO_{2-x}(111)$) = $2x\cdot$ NEXAFS (Ce_2O_3) + $(1\text{-}2x)\cdot$ NEXAFS (CeO_2), with $x = 0.18$ (37% Ce^{3+} fraction). Adapted with permission from reference[2].

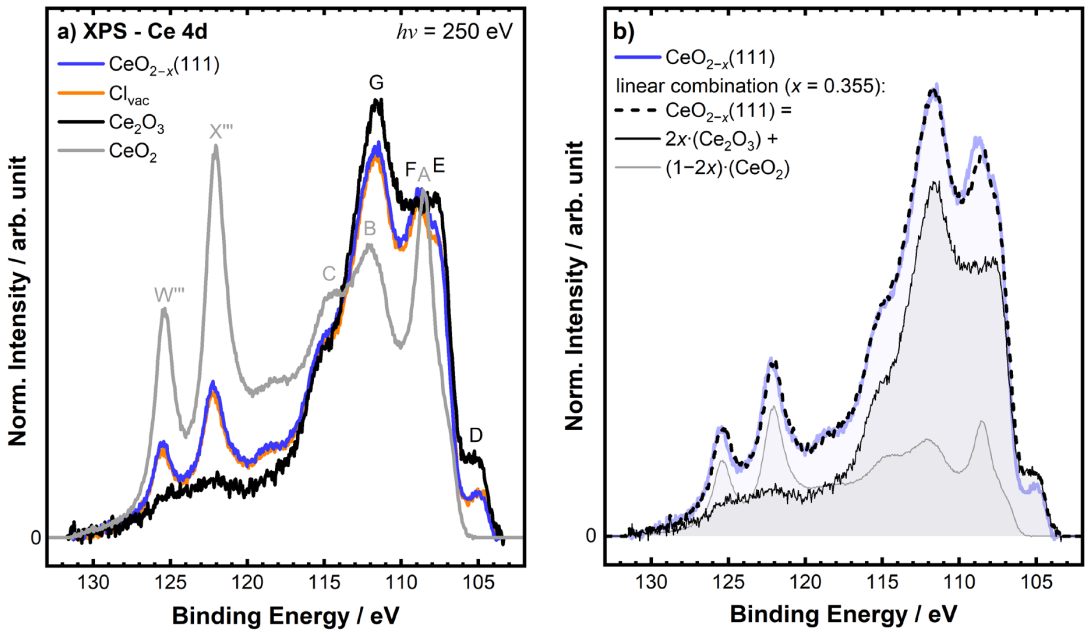

Figure 10.5: a) Surface-sensitive Ce 4d XP spectra ($h\nu = 250$ eV) of partly reduced, pristine $CeO_{2-x}(111)$ (blue), chlorinated Cl_{vac}- $CeO_{2-x}(111)$ (orange), fully reduced reference Ce_2O_3 (black) and fully oxidized reference $CeO_2(111)$ (gray). b) Procedure of linear combination for XPS exemplified for pristine $CeO_{2-x}(111)$: XPS($CeO_{2-x}(111)$) = $(1\text{-}2x)\cdot$XPS(CeO_2) + $2x\cdot$XPS(Ce_2O_3), with $x = 0.35$ (71% Ce^{3+} fraction). Adapted with permission from reference[2].

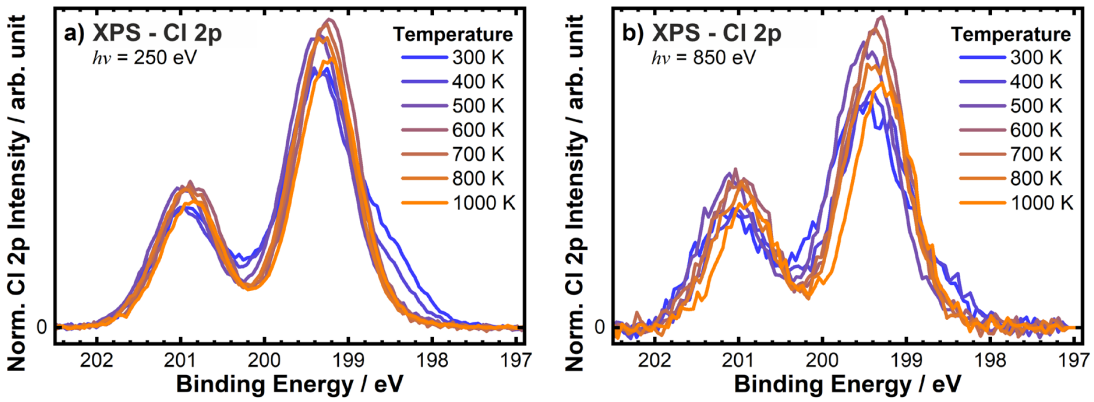

Figure 10.6: Cl 2p XP spectra of CeO_{2-x}(111) when exposed to 15 L HCl at room temperature and subsequently annealed to 1000 K to remove hydrogen. a) surface sensitive: $h\nu$ = 250 eV, b) bulk sensitive $h\nu$ = 850 eV. Adapted with permission from reference[2].

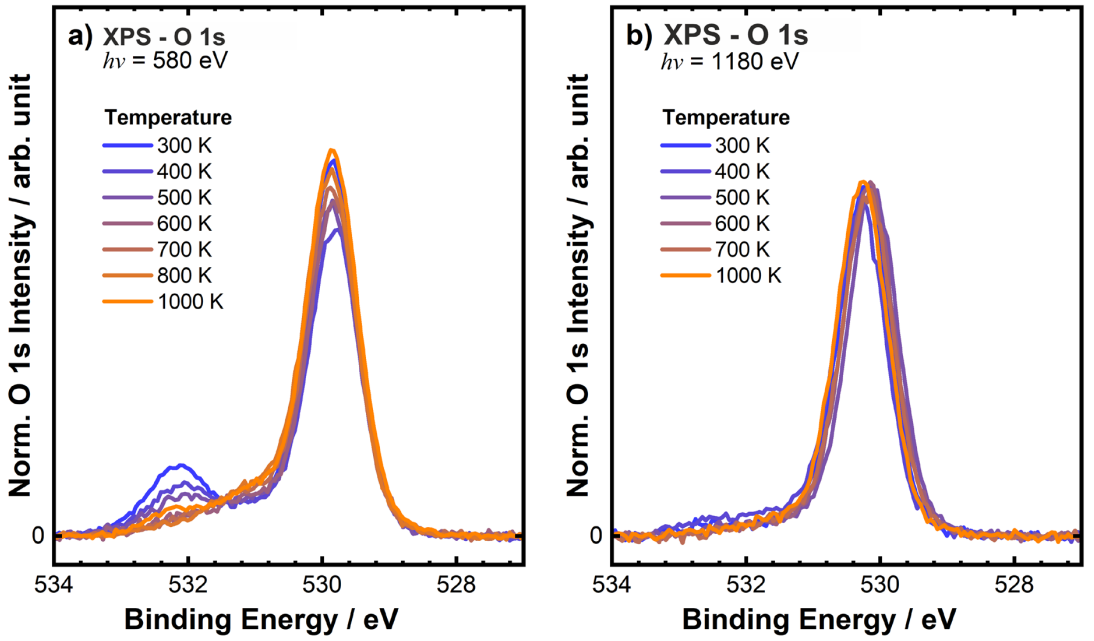

Figure 10.7: O1 s XP spectra of CeO_{2-x}(111) when exposed to 15 L HCl at room temperature and subsequently annealed to 1000 K in steps of 100 K and 200 K to remove hydrogen. a) surface sensitive: $h\nu$ = 580 eV, b) bulk sensitive $h\nu$ = 1180 eV. Adapted with permission from reference[2].

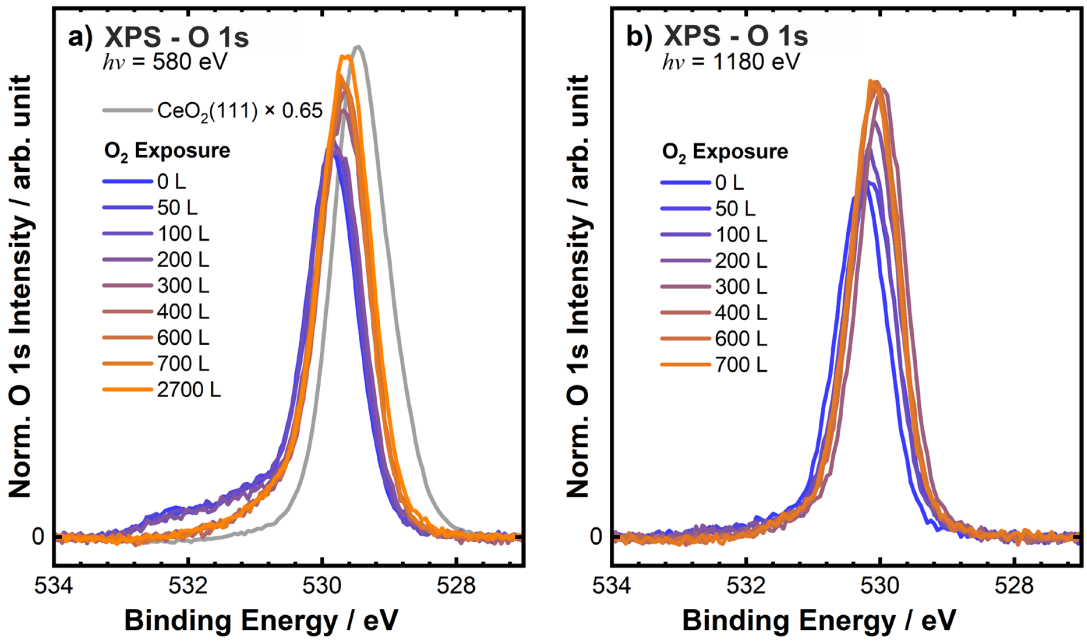

Figure 10.8: O 1s XP spectra of during the re-oxidation at 700K of the fully chlorinated Cl_{vac}-CeO_{2-x}(111) at two photon energies. a) surface sensitive: $h\nu$ = 580 eV, b) bulk sensitive $h\nu$ = 1180 eV. Adapted with permission from reference[2].

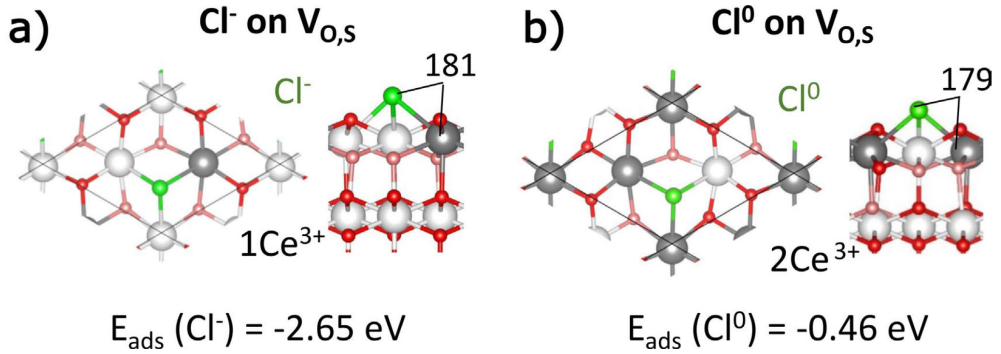

Figure 10.9: Ball and stick model (DFT calculation) of a) Cl^- and b) Cl^0 adsorbed on a surface oxygen vacancy ($V_{O,S}$) on CeO_{2-x}(111) with periodicity ($\sqrt{3} \times \sqrt{3}$)R30°. The Cl–Ce distance is shown in pm and the adsorption energy, E_{ads}, is with respect to the energy of the clean surface with $V_{O,S}$ and 1/2 Cl_2gas. Adapted with permission from reference[2].

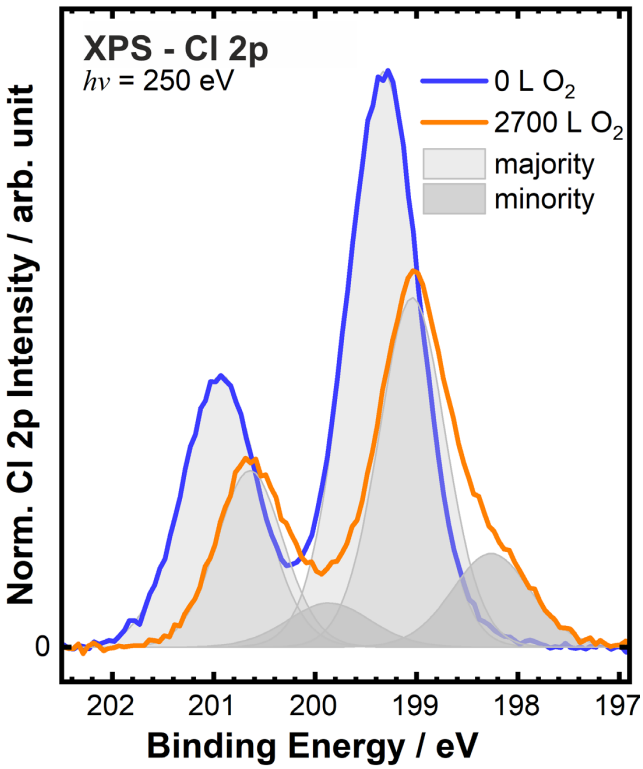

Figure 10.10: Deconvolution of surface sensitive Cl 2p XP spectra ($h\nu$ = 250 eV) of Cl_{vac}-CeO_{2-x}(111) before (0 L O_2) and after (2700 L O_2) re-oxidation. Adapted with permission from reference[2].

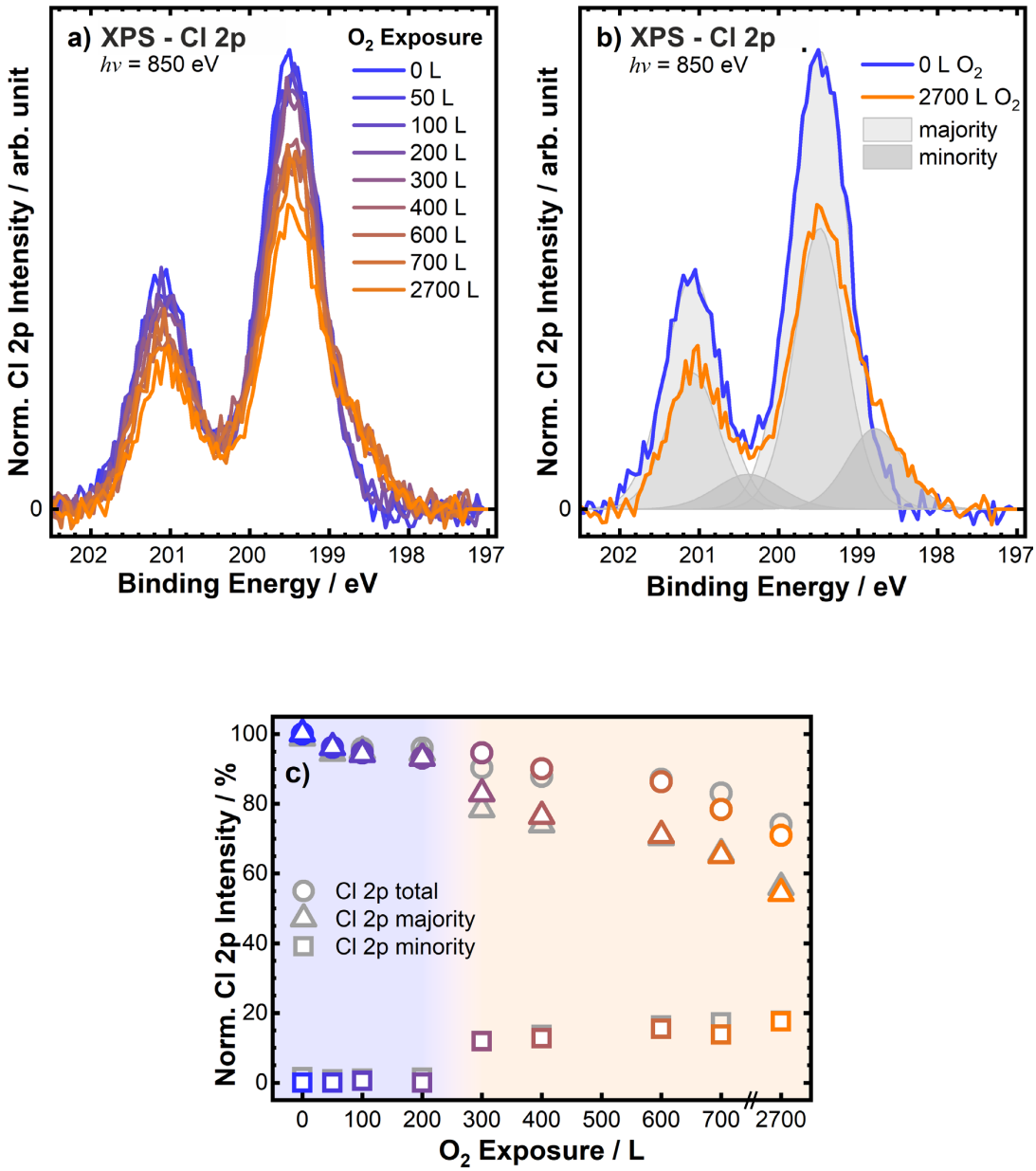

Figure 10.11: a) Bulk-sensitive Cl 2p XP spectra during re-oxidation of Cl_{vac}-CeO_{2-x}(111) at 700 K with various O_2 exposures, for $h\nu$ = 850 eV. b) Deconvolution of bulk sensitive Cl 2p spectrum ($h\nu$ = 850 eV) of Cl_{vac}-CeO_{2-x}(111) before (0 L O_2) and after (2700 L O_2) re-oxidation. c) Intensity of bulk sensitive Cl 2p core level spectra ($h\nu$ = 850 eV) after exposing of Cl_{vac}-CeO_{2-x}(111) to various doses of O_2 at 700 K indicated in Langmuir (L) in comparison with surface sensitive intensity $h\nu$ = 250 eV (gray). Adapted with permission from reference[2].

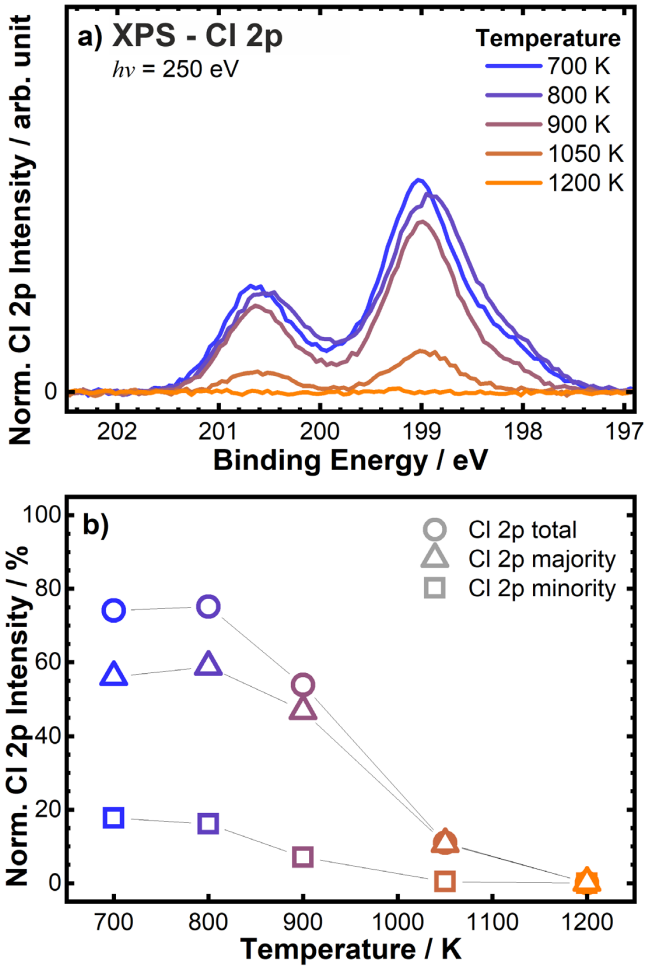

Figure 10.12: a) Thermal desorption of Cl_2 followed by surface sensitive Cl 2p XP spectra, for $h\nu$ = 250 eV with b) the corresponding intensity after deconvolution. Adapted with permission from reference[2].

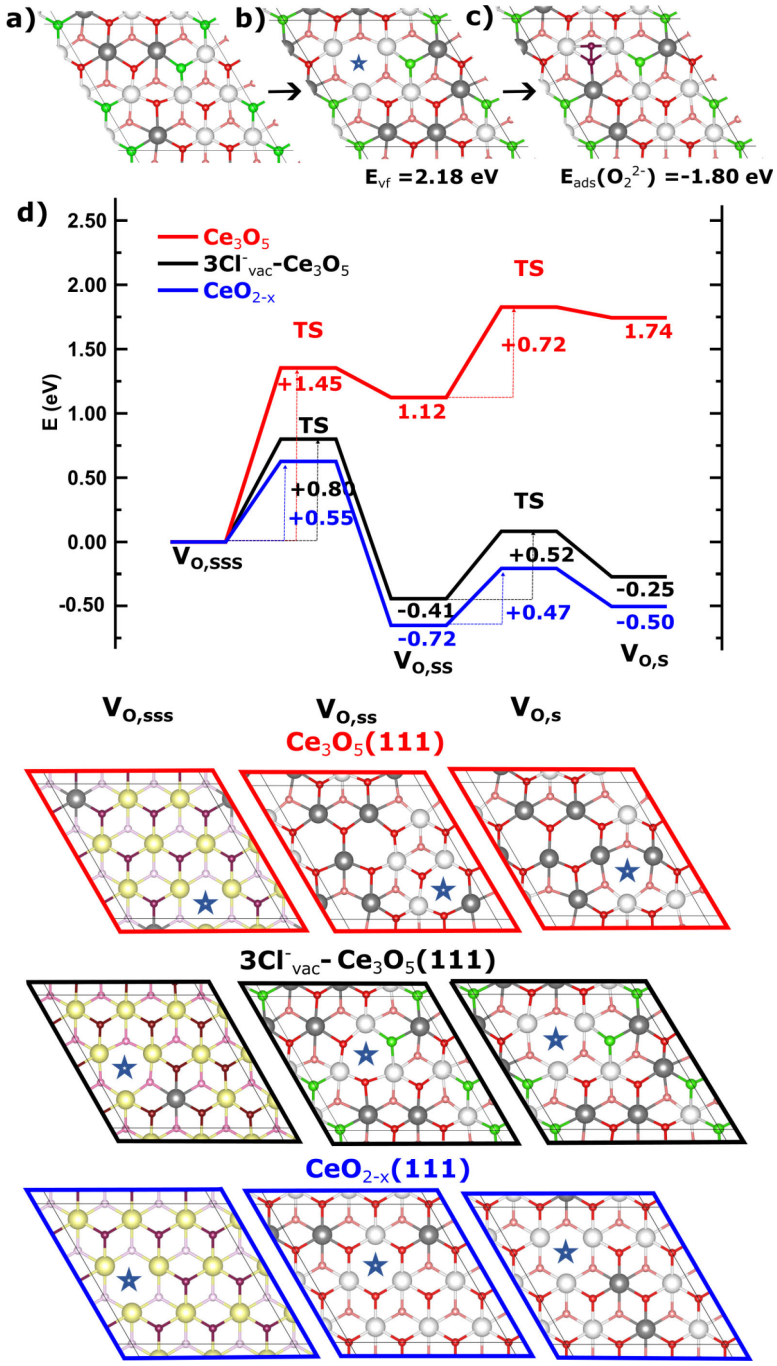

Figure 10.13: Ball and stick model (DFT calculations) of a) $3Cl_{vac}$ atoms adsorbed oxygen vacancies ($V_{O,S}$) on $Ce_3O_5(111)$-(3 × 3), b) The blue star indicates the oxygen vacancy and c) the O_2^{2-} adsorption state on the oxygen vacancy. d) Energy diffusion path of the oxygen vacancy from the third oxygen layer ($V_{O,SSS}$) to the $V_{O,S}$ on the $Ce_3O_5(111)$ with $2V_{O,S}$ and $1V_{O,SS}$ (red path), without oxygen vacancies on $CeO_2(111)$ (blue path) and on $3Cl_{vac}$-$Ce_3O_5(111)$ (black path). Color code: Ce^{4+} first/second trilayers (Ce^{3+}) atoms are white/yellow (gray), the oxygen surface (subsurface) atoms are red (light red), and Cl atoms are in green. Adapted with permission from reference[2].

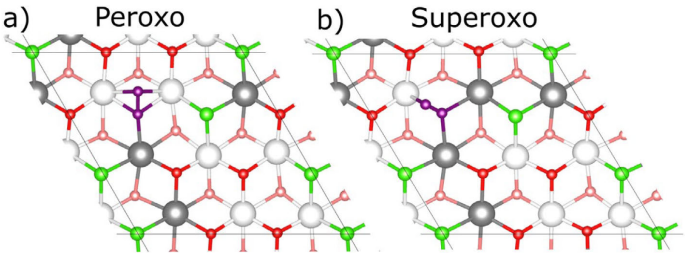

Figure 10.14: a) Peroxo- and b) superoxospecies adsorbed on $3Cl_{vac}$-$Ce_3O_5(111)$-(3×3). Note that there is one more Ce^{3+} in the case of superoxo compared to peroxo species. Adapted with permission from reference[2].

Table 10.5: Comparison between peroxo and superoxo species shown in **Figure 10.14**. Adapted with permission from reference[2].

O_2 species	Relative Energy (eV)	d(O–O) (pm)	Magnetization per O atom	Total Magnetization of O_2 species	Bader Charge difference wrt. O_2 gas
Peroxo	0.00	144	0.000 ; 0.000	0.000	1.23
Superoxo	+0.59	134	0.300 ; 0.490	0.790	0.73

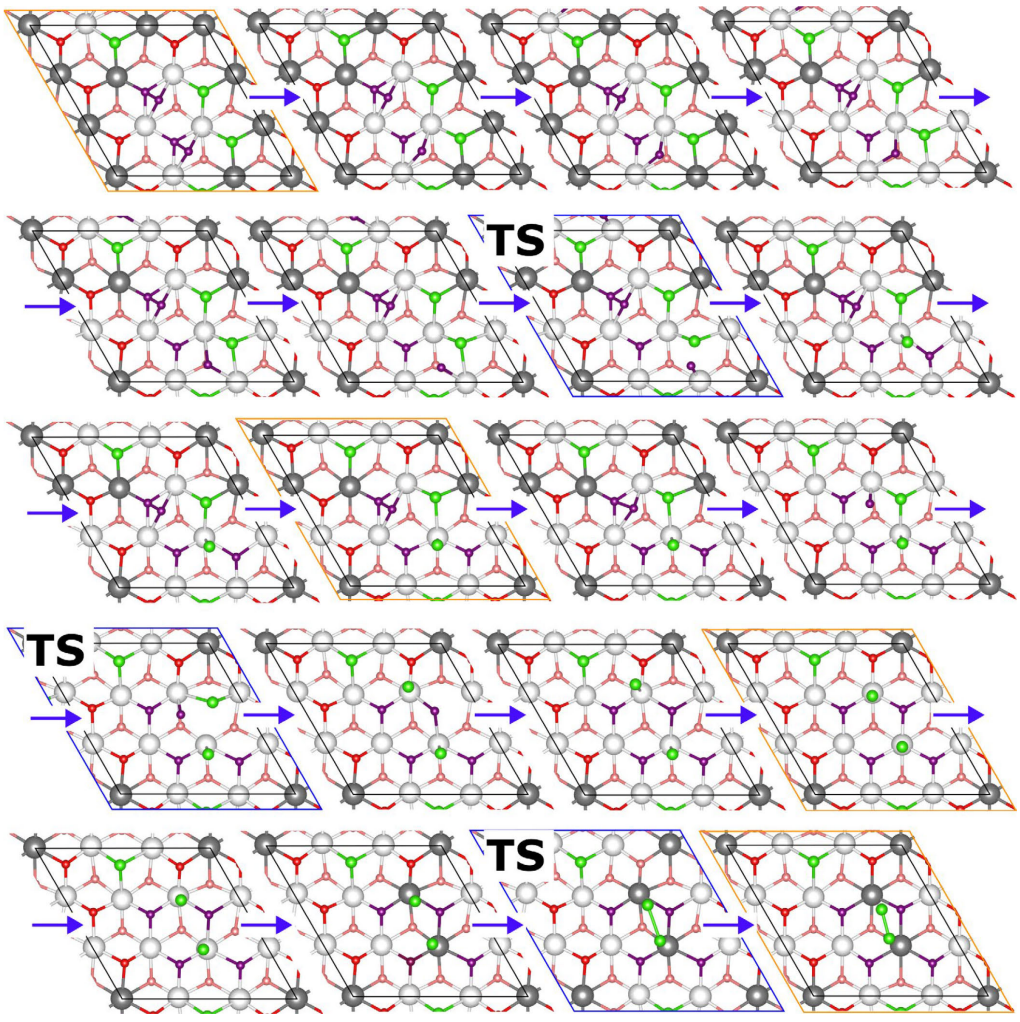

Figure 10.15: Movie frames (DFT calculations) of the de-chlorination process from two adsorbed O_2^{2-} species and three Cl^- adsorbed on oxygen vacancies. The yellow-bordered states are local minima, the transition states (TS) are highlighted in blue, and the remaining states are intermediate states of the reaction paths. Adapted with permission from reference[2].

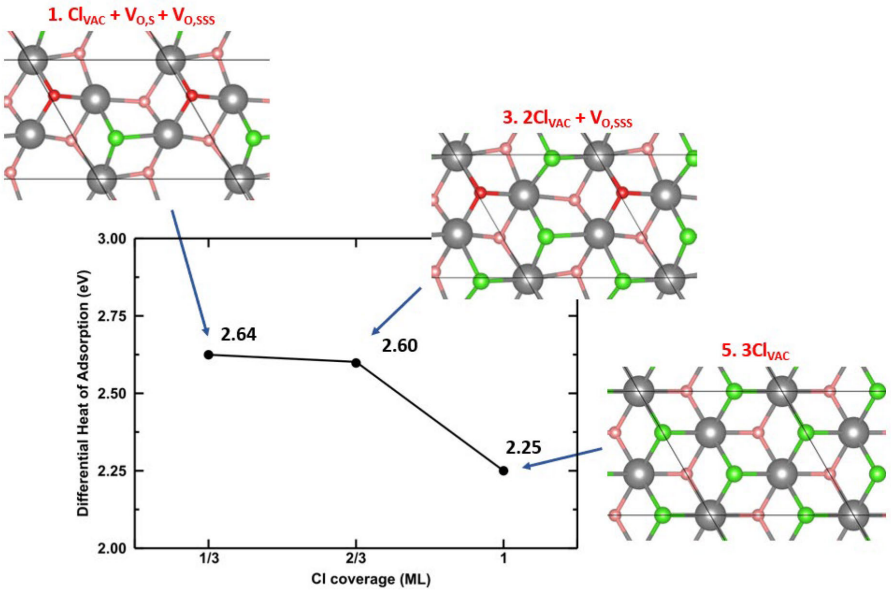

Figure 10.16: Differential heat of adsorption (DFT calculation) of Cl atoms at 1/3 ML, 2/3 ML, and 1 ML in the $(\sqrt{3} \times \sqrt{3})$R30° with 3 oxygen vacancies. Adapted with permission from reference[2].

The differential heat of adsorption is calculated by applying the following formula: $-(E((n+1)\mathrm{Cl}) - E(n\mathrm{Cl}) - 1/2 \cdot E(\mathrm{Cl_2gas}))$ where n= 0, 1, or 2 indicates the number of chlorine atoms, $E(\mathrm{Cl_2gas})$ is the energy of Cl_2 in the gas phase, and the terms $E((n+1)\mathrm{Cl})/E(n\mathrm{Cl})$ are the total energies of the n+1/n chlorine atoms adsorbed in the unit cell $(\sqrt{3} \times \sqrt{3})$R30°. When n = 0, $E(0\mathrm{Cl})$ is the total energy of the CeO_{2-x} surface, where the formula becomes minus the adsorption energy of a chlorine atom ($-E_{ads}(\mathrm{Cl})$).

The reported results correspond to the lower energy obtained by optimizing the adsorption site of the Cl atom, the position of the Ce^{3+}, and the oxygen vacancies. In these calculations the $(\sqrt{3} \times \sqrt{3})$R30° have 5 trilayers, 3 oxygen vacancies which may be distributed in the first three oxygen layers ($V_{O,S}$; $V_{O,SS}$; $V_{O,SSS}$), the 5, 4 and 3 Ce^{3+} arising from the 3 oxygen vacancies and the adsorption of $1Cl^-$, $2Cl^-$ and $3Cl^-$, respectively, are distributed in the top three trilayers.

10.2 Modeling of the CeO_{2-x}(111) Surface

The DFT calculations were realized by Pablo G. Lustemberg and M. Verónica Ganduglia-Pirovano. The CeO_{2-x}(111) surfaces are modeled with a lattice constant of 5.485 Å calculated from the CeO_2 bulk. Different Cl phases in **Chapter 7.1** with $(\sqrt{3} \times \sqrt{3})$R30°, $(\sqrt{7} \times \sqrt{7})$R19.1°, (3 × 3) and (4 × 4) symmetry are modeled according to what was reported by Olbrich et al.,[90] where each phase is characterized by the number of surface ($V_{O,s}$) and subsurface ($V_{O,ss}$) vacancies, as described in **Table 10.6**.

Additionally the Cl surface phase in **Chapter 7.2** is modeled based on the (3 × 3) unit cell reported by Olbrich et al.[39] for describing the formation of reduced CeO_{2-x}(111) surface reconstructions with one surface ($V_{O,S}$, V: Vacancy, O: Oxygen, S: Surface) and two subsurface ($V_{O,SS}$, SS: Sub-Surface) oxygen vacancies in the outermost O–Ce–O trilayer. As the results in **Chapter 7.2** involve the modeling of oxygen vacancies in the third oxygen layer ($V_{O,SSS}$, SSS: Sub-Sub-Surface, i.e. a vacancy in the third oxygen layer), a slab

containing three O−Ce−O trilayers was used, keeping the bottom trilayer fixed, and ~21 Å of vacuum separation between consecutive slabs.

All surface models used in this work have ~21 Å of vacuum separation between consecutive slabs. The number of trilayers (three O−Ce−O), *k*-point mesh using the Monkhorst−Pack method,[195] and the number of Ce^{3+} atoms per trilayer are also indicated in **Table 10.6**. For the calculations of the HCl, O_2, H_2 and Cl_2 molecules in the gas-phase, a (15 × 15 × 15) $Å^3$ cell was used, with Γ-point only.

Table 10.6: Characteristics of the different Cl-CeO_{2-x} modeled phases. The number of surface ($V_{O,s}$) and subsurface ($V_{O,ss}$) vacancies is indicated. In the case of the (4 × 4) phase, the third and fourth oxygen layers of the second trilayer each also have 4 oxygen vacancies.

Phase	(√3 × √3)R30°		(√7 × √7)R19.1°	(3 × 3)	(4 × 4)
No. $V_{O,s}$	1	2	1	1	4
No. $V_{O,ss}$	--	--	1	2	4
No. Ce atoms per trilayer	3	3	7	9	16
No. Ce^{3+} 1st trilayer	2	3	4	4	16
No. Ce^{3+} 2nd trilayer	--	1	--	2	15
No. Ce^{3+} 3rd trilayer	--	--	--	--	1
k-points mesh	4×4×1		3×3×1	2×2×1	1×1×1
No. atomic trilayers	4		3	3	4
Relaxed/fixed layers	3/1		2/1	2/1	3/1
Surface area (nm^2)	0.10		0.91	1.17	2.08

The reported Cl adsorption energies in **Chapter 7.1** are calculated per Cl atom according to the following equation:

$$E_{ads}(Cl) = (E[N\text{Cl}/CeO_{2-x}] - E[CeO_{2-x}] - N/2\ E[Cl_{2,gas}])/N$$

where $E[N\text{Cl}/CeO_{2-x}]$ is the total energy of N atoms of Cl adsorbed on the reduced CeO_{2-x} surface, the $E[CeO_{2-x}]$ is the total energy of the clean $CeO_{2-x}(111)$ surface and $E[Cl_{2,gas}]$ is the energy of the chlorine molecule in gas phase.

The adsorption energy of chemisorbed O_2 in **Chapter 7.2** species is calculated according to the following equation:

$$E_{ads} = E[(nO_2/3Cl_{vac}\text{-}CeO_{2-x}(111)] - E[3Cl_{vac}\text{-}CeO_{2-x}(111)] - nE[O_{2,gas}],$$

where n = 1,2 is the number of adsorbed O_2 species, $E[(nO_2/3Cl_{vac}\text{-}CeO_{2-x}(111)]$ is the total energy of the O_2 molecules atoms adsorbed on the chlorinated surface with two oxygen vacancies on the third oxygen layer ($3Cl_{vac}\text{-}Ce_3O_5(111)\text{-}(3 \times 3)+2V_{O,SSS}$), $E[3Cl_{vac}\text{-}CeO_{2-x}(111)]$ is the total energy of the surface without the adsorbate, and $E[O_{2,gas}]$ is the energy of the oxygen molecule in gas phase.

10.3 Experimental Details DFT Calculations

Spin-polarized DFT calculations were carried out using the slab−supercell approach,[51] with the Vienna Ab-initio Simulation Program (VASP, version 5.3.5 and 5.4.4).[196–200] The Ce (4f, 5s, 5p, 5d, 6s), O (2s, 2p), Cl (2s, 2p), and H (1s) electrons are explicitly treated as valence states using the projector augmented wave (PAW) method.[201] A plane-wave cutoff energy of 400 eV is applied, while the remaining electrons are considered part of the atomic cores. The energies and forces were calculated using the DFT+U approach by Dudarev et al.[202] (U_{eff} = U − J = 4.5 eV for the Ce 4f electrons) with the generalized gradient approximation (GGA) proposed by Perdew, Burke, and Ernzerhof (PBE).[203] DFT(PBE)+U is a widely employed approach in the study of ceria-based systems. However, it's widely acknowledged that hybrid functionals, which incorporate a mixture of DFT(GGA) and Hartree-Fock exchange energies, offer enhanced computational accuracy for ceria-based systems, albeit at a significantly higher computational cost. Notably, for the results in **Chapter 7.2**, these methods excel in describing the relative stability of surface and subsurface oxygen vacancies, as well as the interaction of molecular O_2 with reduced ceria surfaces. Both hybrid and DFT(PBE)+U methodologies consistently indicate that O vacancies tend to form preferentially on subsurface sites, with the two excess electrons localizing on next-nearest-neighbor Ce^{3+} ions, as demonstrated by Ganduglia-Pirovano et al..[154] Additionally, Preda et al.[155] employed small Ce_2O_3 clusters and both hybrid and DFT(PBE)+U methodologies, consistently finding that on reduced ceria nanoparticles, superoxide O_2^- species are formed through the direct interaction of O_2 with low-coordinated Ce^{3+} ions.

The oxidation state of a given Ce ion has been estimated by considering its local magnetic moment (the difference between up and down spin on the atoms), which can be estimated by integrating the site- and angular momentum-projected spin-resolved density of states over spheres with radii chosen as the Wigner−Seitz radii of the PAW potentials. For reduced Ce ions, the occupation of Ce f states is close to 1, and the magnetic moment is ~1 μB. Hence, those ions are referred to as Ce^{3+}. The number of the Ce^{3+} ions results from optimizing the structure, while the optimal configuration of the excess electrons is found through a two-step procedure. Initially, to attain a desired configuration, the Ce atoms in which excess electrons were intended to be incorporated were reclassified as a different species and assigned the Ce^{3+} pseudopotential provided by the VASP's pseudopotential repository. Due to the larger ionic radius of Ce^{3+} in comparison to Ce^{4+}, the atomic positions of all atoms were optimized, resulting in the desired structural configuration. Subsequently, in a second optimization step, the structure obtained in the previous step was further optimized. However, in this case, all Ce atoms were represented with the Ce^{4+} pseudopotential. This second step was crucial in obtaining the energy of the chosen spatial configuration.

It is important to mention the PBE gradient approximation tendency to overestimate the bond energy of O_2 by up to 0.5 eV.[203] A variation of 0.5 eV in this regard would have no significant impact in our conclusions.

To locate transition state (TS) structures, the climbing image nudged elastic band method (CI-NEB)[204] was employed with seven images for each reaction pathway. For all the TS

reported in this work, only one imaginary frequency was found, and the full geometry optimizations starting from its back and forward nearest configurations (along the reaction path) end in a non-dissociated and dissociated state, respectively. In the calculated potential energy profiles, the energy barrier, $E_{\mathrm{Barrier}} = E_{\mathrm{TS}} - E_{\mathrm{IS}}$, equals the difference between the energy of the transition state, E_{TS}, and the initial state, E_{IS}.

11 List of Abbreviations

Cl_{top}	Chlorine on Top of Cerium
Cl_{vac}	Chlorine in an Oxygen Vacancy
DFT	Density Functional Theory
fcc	Face-Centered Cubic
GGA	Generalized Gradient Approximation
hcp	Hexagonal Closely Packed
IMFP	Inelastic Mean Free Path
IV	Intensity versus Voltage
L	Langmuir
LEED	Low-Energy Electron Diffraction
ML	Monolayer
MS	Mass Spectrometer
NC-AFM	Non-Contact Atomic Force Microscopy
NEXAFS	Near Edge X-ray Absorption Fine Structure
OSC	Oxygen Storage Capacity
PAW	Projector Augmented Wave
PBE	Perdew, Burke, and Ernzerhof
PC	Polycarbonate
PGAA	Prompt Gamma-ray Neutron Activation Analysis
PU	Polyurethane
PVD	Physical Vapor Deposition
SS	Sub-Surface
SSS	Sub-Sub-Surface
STM	Scanning Tunneling Microscopy
TEY	Total Electron Yield
TPD	Temperature Programmed Desorption
UHV	Ultra-High Vacuum
VASP	Vienna Ab-initio Simulation Program
XPS	X-ray Photoelectron Spectroscopy
XRR	X-ray Reflectivity

12 References

(1) Koller, V.; Sack, C.; Lustemberg, P.; Ganduglia-Pirovano, M. V.; Over, H. Dynamic Response of Oxygen Vacancies in the Deacon Reaction over Reduced Single Crystalline CeO_{2-x}(111) surface. *J. Phys. Chem. C* **2022**, *126*, 13202–13212.

(2) Koller, V.; Lustemberg, P. G.; Spriewald-Luciano, A.; Gericke, S. M.; Larsson, A.; Sack, C.; Preobrajenski, A.; Lundgren, E.; Ganduglia-Pirovano, M. V.; Over, H. Critical Step in the HCl Oxidation Reaction over Single-Crystalline CeO_{2-x}(111): Peroxo-Induced Site Change of Strongly Adsorbed Surface Chlorine. *ACS Catal.* **2023**, *13*, 12994–13007.

(3) www.offshore-technology.com/analyst-comment/global-chlorine-capacity-additions/ (accessed 2024-03-27).

(4) Kleoff, M.; Voßnacker, P.; Riedel, S. The Rise of Trichlorides Enabling an Improved Chlorine Technology. *Angew. Chem. Int. Ed.* **2023**, *62*, e202216586.

(5) www.chlorineindustryreview.com/wp-content/uploads/2023/10/Chlor-Alkali-Industry-Review-CORRECTED-2023-10-06.pdf (accessed 2024-03-27).

(6) Lin, R.; Amrute, A. P.; Pérez-Ramírez, J. Halogen-Mediated Conversion of Hydrocarbons to Commodities. *Chem. Rev.* **2017**, *117*, 4182–4247.

(7) Pérez-Ramírez, J.; Modelli, C.; Schmidt, T.; Schlüter, O. F.-K.; Wolf, A.; Mleczko, L.; Dreier, T. Sustainable Chlorine Recycling via Catalyzed HCl Oxidation: From Fundamentals to Implementation. *Energy Environ Sci.* **2011**, *4*, 4786-4799.

(8) Abts, G.; Eckel, T.; Wehrmann, R. Polycarbonates. In *Ullmann's Encyclopedia of Industrial Chemistry*; Wiley-VCH Verlag GmbH & Co. KGaA, 2014; pp 1–18.

(9) Iwanaga, K.; Seki, K.; Hibi, T.; Issoh, K.; Suzuta, T.; Nakada, M.; Mori, Y., Abe. T. The Development of Improved Hydrogen Chloride Oxidation Process, Sumitomo Chemical Co., Ltd., R&D Report, *"SUMITOMO KAGAKU"*, vol. 2004-I.

(10) Hisham, M. W. M.; Benson, S. W. Thermochemistry of the Deacon Process. *J. Phys. Chem.* **1995**, *99*, 6194–6198.

(11) Moussallem, I.; Jörissen, J.; Kunz, U.; Pinnow, S.; Turek, T. Chlor-alkali Electrolysis with Oxygen Depolarized Cathodes: History, Present Status and Future Prospects. *J. Appl. Electrochem.* **2008**, *38*, 1177–1194.

(12) Over, H.; Schomäcker, R. What Makes a Good Catalyst for the Deacon Process? *ACS Catal.* **2013**, *3*, 1034–1046.

(13) Townsend, C. A. An Evaluation of Ferdinand Hurter's Contribution to the Development of the Nineteenth Century Alkali Industry, Dissertation, Liverpool John Moores University, Liverpool, UK, 1998.

(14) Deacon, H. Improvement in the Manufacture of Chlorine. US 0085370 A, 1868.

(15) Deacon, H. XXIX.—On Deacon's Method of Obtaining Chlorine, as Illustrating Some Principles of Chemical Dynamics. *J. Chem. Soc.* **1872**, *25*, 725–767.

(16) Amrute, A. P.; Mondelli, C.; Moser, M.; Novell-Leruth, G.; López, N.; Rosenthal, D.; Farra, R.; Schuster, M. E.; Teschner, D.; Schmidt, T.; Pérez-Ramírez, J. Performance, Structure, and Mechanism of CeO_2 in HCl Oxidation to Cl_2. *J. Catal.* **2012**, *286*, 287–297.

(17) Scharfe, M.; Zichittella, G.; Paunović, V.; Pérez-Ramírez, J. Ceria in Halogen Chemistry. *Chin. J. Catal.* **2020**, *41*, 915–927.

(18) Abundance of Elements in the Earth's Crust and in the Sea, in *CRC Handbook of Chemistry and Physics*, 97th Ed.; Haynes, W. M.; Lide, D. R.; Bruno, T. J., Eds., CRC Press, 2017, 14–17.

(19) Moser, M.; Mondelli, C.; Schmidt, T.; Girgsdies, F.; Schuster, M. E.; Farra, R.; Szentmiklósi, L.; Teschner, D.; Pérez-Ramírez, J. Supported CeO_2 Catalysts in Technical Form for Sustainable Chlorine Production. *Appl. Catal. B* **2013**, *132–133*, 123–131.

(20) Kanzler, C. H.; Urban, S.; Zalewska-Wierzbicka, K.; Hess, F.; Rohrlack, S. F.; Wessel, C.; Ostermann, R.; Hofmann, J. P.; Smarsly, B. M.; Over, H. Electrospun Metal Oxide Nanofibers for the Assessment of Catalyst Morphological Stability under Harsh Reaction Conditions. *ChemCatChem* **2013***, 5*, 2621−2626.

(21) Li, C.; Sun, Y.; Djerdj, I.; Voepel, P.; Sack, C.-C.; Weller, T.; Ellinghaus, R.; Sann, J.; Guo, Y.; Smarsly, B. M.; Over, H. Shape-Controlled CeO_2 Nanoparticles: Stability and Activity in the Catalyzed HCl Oxidation Reaction. *ACS Catal.* **2017**, *7*, 6453–6463.

(22) Farra, R.; García-Melchor, M.; Eichelbaum, M.; Hashagen, M.; Frandsen, W.; Allan, J.; Girgsdies, F.; Szentmiklósi, L.; López, N.; Teschner, D. Promoted Ceria: A Structural, Catalytic, and Computational Study. *ACS Catal.* **2013**, *3*, 2256–2268.

(23) Urban, S.; Tarabanko, N.; Kanzler, C. H.; Zalewska-Wierzbicka, K.; Ellinghaus, R.; Rohrlack, S. F.; Chen, L.; Klar, P. J.; Smarsly, B. M.; Over, H. Stable and Active Mixed Zr–Ce Oxides for Catalyzing the Gas Phase Oxidation of HCl. *Catal. Lett.* **2013**, *143*, 1362–1367.

(24) Möller, M.; Urban, S.; Cop, P.; Weller, T.; Ellinghaus, R.; Kleine-Boymann, M.; Fiedler, C.; Sann, J.; Janek, J.; Chen, L.; Klar, P. J.; Hofmann, D. M.; Philipps, J.; Dolcet, P.; Gross, S.; Over, H.; Smarsly, B. M. Synthesis and Physicochemical Characterization of $Ce_{1-x}Gd_xO_{2-\delta}$: A Case Study on the Impact of the Oxygen Storage Capacity on the HCl Oxidation Reaction. *ChemCatChem* **2015**, *7*, 3738–3747.

(25) Sun, Y.; Hess, F.; Djerdj, I.; Wang, Z.; Weber, T.; Guo, Y.; Smarsly, B. M.; Over, H. Reactivation of CeO_2-based Catalysts in the HCl Oxidation Reaction: In situ Quantification of the Degree of Chlorination and Kinetic Modeling. *ChemCatChem* **2020**, *12*, 5511–5522.

(26) Hasegawa, T.; Shahed, S. M. F.; Sainoo, Y.; Beniya, A.; Isomura, N.; Watanabe, Y.; Komeda, T. Epitaxial Growth of CeO_2(111) Film on Ru(0001): Scanning Tunneling Microscopy (STM) and X-Ray Photoemission Spectroscopy (XPS) Study. *J. Chem. Phys.* **2014**, *140*, 044711.

(27) Mullins, D. R.; Radulovic, P. V.; Overbury, S. H. Ordered Cerium Oxide Thin Films Grown on Ru(0001) and Ni(111). *Surf. Sci.* **1999**, *429*, 186–198.

(28) Sack, C. C. CeO_x(111)/Ru(0001) as Model Catalyst for the HCl-Oxidation. Dissertation, Justus-Liebig-University Giessen, Giessen, Germany, 2019.

(29) Metcalfe, I. S.; Ray, B.; Dejoie, C.; Hu, W.; Leeuwe, C. de; Dueso, C.; García-García, F. R.; Mak, C.-M.; Papaioannou, E. I.; Thompson, C. R.; Evans, J. S. O. Overcoming Chemical Equilibrium Limitations using a Thermodynamically Reversible Chemical Reactor. *Nat. Chem.* **2019**, *11*, 638–643.

(30) Mortensen, M.; Minet, R. G.; Tsotsis, T. T.; Benson, S. A Two-stage Cyclic Fluidized Bed Process for Converting Hydrogen Chloride to Chlorine. *Chem. Eng. Sci.* **1996**, *51*, 2031–2039.

(31) Sack, C.; Lustemberg, P.; Koller, V.; Ganduglia-Pirovano, M. V.; Over, H. Interaction of HCl with a CeO_2(111) Layer Supported on Ru(0001): A Theory and Experiment Combined Study. *J. Phys. Chem. C* **2018**, *122*, 19584–19592.

(32) Rupprechter, G. Surface Science Approach to Heterogeneous Catalysis. In *Surface and Interface Science*; Wandelt, K., Ed.; Wiley, 2016; pp 459–528.

(33) Attard, G.; Barnes, C. *Surfaces*; Oxford Chemistry Primers, Vol. 59; Compton, R. G., Ed., Oxford University Press, 2011.

(34) www.uni-giessen.de/de/fbz/fb08/Inst/physchem/over (accessed 2024-03-27).

(35) Mullins, D. R. The Surface Chemistry of Cerium Oxide. *Surf. Sci. Rep.* **2015**, *70*, 42–85.

(36) Khare, P., Kumar, N.; Kumari, K. M.; Srivastava, S. S. Atmospheric Formic and Acetic Acids: An Overview. *Rev. Geophys*. **1999**, *37*, 227–248.

(37) Gasperi, G.; Luches, P.; Barth, C. Stability of Ultrathin Ceria Films on Pt(111) Exposed to Air and Treated in Redox Cycles. *J. Phys. Chem. C* **2018**, *122*, 25954–25963.

(38) Exner, K. S.; Heß, F.; Over, H.; Seitsonen, A. P. Combined Experiment and Theory Approach in Surface Chemistry: Stairway to Heaven? *Surf. Sci.* **2015**, *640*, 165–180.

(39) Stöhr, J. *NEXAFS Spectroscopy*, Ertl, G.; Gomer, R.; Mills, D. L.; Lotsch, H. K. V., Eds.; Springer Series in Surface Science, Vol. 25; Springer, 2003.

(40) Als-Nielsen, J.; McMorrow, D. *Elements of Modern X-ray Physics*, 2nd ed.; John Wiley & Sons Ltd, 2017.

(41) Preobrajenski, A.; Generalov, A.; Öhrwall, G.; Tchaplyguine, M.; Tarawneh, H.; Appelfeller, S.; Frampton, E.; Walsh, N. FlexPES: A Versatile Soft X-ray Beamline at MAX IV Laboratory. *J. Synchrotron Radiat.* **2023**, *30*, 831-840.

(42) Nilsson, A. Applications of Core Level Spectroscopy to Adsorbates. *J. Electron Spectrosc. Relat. Phenom.* **2002**, *126*, 3–42.

(43) Christmann, K. *Introduction to Surface Physical Chemistry*; Baumgärtel, H.; Franck, E.U.; Grünbein, W., Eds.; Topics in Physical Chemistry, Vol. 1; Springer, 1991.

(44) Seidel, C.; Kopf, H.; Gotsmann, B.; Vieth, T.; Fuchs, H.; Reihs, K. Ar Plasma Treated and Al Metallised Polycarbonate: a XPS, Mass Spectroscopy and SFM study. *Appl. Surf. Sci.* **1999**, *150*, 19–33.

(45) www-ssrl.slac.stanford.edu/stohr/nexafs.htm (accessed 2024-03-27).

(46) Besley, N. A. Density Functional Theory Based Methods for the Calculation of X-ray Spectroscopy. *Acc. Chem. Res.* **2020**, *53*, 1306–1315.

(47) Renaud, G.; Lazzari, R.; Leroy, F. Probing Surface and Interface Morphology with Grazing Incidence Small Angle X-Ray Scattering. *Surf. Sci. Rep.* **2009**, *64*, 255–380.

(48) Kiessig, H. Untersuchungen zur Totalreflexion von Röntgenstrahlen. *Ann. Phys.* **1931**, *402*, 715–768.

(49) Chason, E.; Mayer, T. M. Thin Film and Surface Characterization by Specular X-ray Reflectivity. *Crit. Rev. Solid State Mater. Sci.* **1997***, 22*, 1–67.

(50) Sholl, D. S.; Steckel, J. A. *Density Functional Theory: A Practical Introduction*; John Wiley & Sons, Inc., 2009.

(51) Payne, M. C.; Teter, M. P.; Allan, D. C.; Arias, T. A.; Joannopoulos, J. Iterative Minimization Techniques for Ab Initio Total-Energy Calculations: Molecular Dynamics and Conjugate Gradients. *Rev. Mod. Phys.* **1992**, *64*, 1045−1097.

(52) Seki, K. Development of RuO_2/Rutile-TiO_2 Catalyst for Industrial HCl Oxidation Process, *Catal. Surv. Asia* **2010**, *14*, 168.

(53) Hess, F. Is There a Stable Deacon Catalyst? Computational Screening Approach for the Stability of Oxide Catalysts under Harsh Conditions. *ACS Catal.* **2022***, 12*, 497–511.

(54) www.ourworldindata.org/electricity-mix (accessed 2024-03-27).

(55) Schmittinger, P.; Florkiewicz, T.; Curlin, L. C.; Lüke, B.; Scannell, R.; Navin, T.; Zelfel, E.; Bartsch, R. Chlorine. In *Ullmann's Encyclopedia of Industrial Chemistry*; Wiley-VCH Verlag GmbH & Co. KGaA, 2000; p 799.

(56) Allen, J. A. Energetic Criteria for Oxychlorination Catalysts. *J. Appl. Chem. (London, U. K.)* **1962**, *12*, 406–412.

(57) Hess, F.; Over, H. Rate-Determining Step or Rate-Determining Configuration? The Deacon Reaction over RuO_2(110) Studied by DFT-Based KMC Simulations. *ACS Catal.* **2017***, 7*, 128–138.

(58) Ando, H.; Uchida, Y.; Seki, K.; Knapp, C.; Omoto N.; Kinoshita, M. Trends and Views in the Development of Technologies for Chlorine Production from Hydrogen Chloride, Sumitomo Chemical Co., Ltd., R&D Report, *"SUMITOMO KAGAKU"*, vol. 2010-II

(59) www.sumitomo-chem.co.jp/technology-licensing/success-stories/covestro/ (accessed 2024-03-27).

(60) www.covestro.com/en/news-pages/ch/covestros-new-chlorine-production-plant-deacon-ii-starts-up-in-shanghai (accessed 2024-03-27).

(61) Over, H. Atomic-Scale Understanding of the HCl Oxidation Over RuO_2, A Novel Deacon Process. *J. Phys. Chem. C* **2012***, 116*, 6779–6792.

(62) Zweidinger, S.; Crihan, D.; Knapp, M.; Hofmann, J. P.; Seitsonen, A. P.; Weststrate, C. J.; Lundgren, E.; Andersen, J. N.; Over, H. Reaction Mechanism of the Oxidation of HCl over RuO_2(110). *J. Phys. Chem. C* **2008***, 112*, 9966–9969.

(63) www.statista.com/statistics/1046426/ruthenium-price/ (accessed 2024-03-27).

(64) Feng, K.; Li, C.; Guo, Y.; Zhan, W.; Ma, B.; Chen, B.; Yuan, M.; Lu, G. An Efficient Cu-K-La/γ-Al_2O_3 Catalyst for Catalytic Oxidation of Hydrogen Chloride to Chlorine. *App. Catal. B* **2015***, 164*, 483–487.

(65) Sun, Y.; Li, C.; Guo, Y.; Zhan, W.; Guo, Y.; Wang, L.; Wang, Y.; Lu, G. Catalytic Oxidation of Hydrogen Chloride to Chlorine over Cu-K-Sm/γ-Al_2O_3 Catalyst with Excellent Catalytic Performance. *Catal. Today* **2018***, 307*, 286–292.

(66) Tang, J.; Chen, X.; Fei, Z.; Zhao, J.; Cui, M.; Qiao, X. HCl Oxidation to Recycle Cl_2 over a Cu/Ce Composite Oxide Catalyst. Part 1. Intrinsic Kinetic Study. *Ind. Eng. Chem. Res.* ***2013****, 52*, 11897–11903.

(67) Yang, G.; Sun, Y.; Zhang, J.; Li, Z.; Wang, Y. Clean Production of Chlorine from Hydrogen Chloride with Mn-compound as Intermediate. *Chin. J. Chem. Eng.* ***2015****, 23*, 435–440.

(68) Amrute, A. P.; Larrazábal, G. O.; Mondelli, C.; Pérez-Ramírez, J. $CuCrO_2$ Delafossite: A Stable Copper Catalyst for Chlorine Production. *Angew. Chem. Int. Ed.* **2013**, *125*, 9954–9957.

(69) www.statista.com/statistics/450146/global-reo-cerium-oxide-price-forecast/ (accessed 2024-03-27).

(70) *Catalysis by Ceria and Related Materials*, 2nd ed.; Trovarelli, A., Fornasiero, P., Eds.; Catalytic Science Series, Vol. 12; Imperial College Press, 2013.

(71) Trovarelli, A.; Llorca, J. Ceria Catalysts at Nanoscale: How Do Crystal Shapes Shape Catalysis? *ACS Catal.* **2017**, *7*, 4716–4735.

(72) Maier, J. *Physical Chemistry of Ionic Materials*: *Ions and Electrons in Solids*; John Wiley & Sons Ltd, 2004.

(73) *Catalysis by Ceria and Related Materials*; Trovarelli, A. Ed.; Catalytic Science Series, Vol. 2; Imperial College Press, 2005.

(74) Adachi, G.; Imanaka, N. The Binary Rare Earth Oxides. *Chem. Rev.* **1998**, *98*, 1479−1514

(75) Höcker, J.; Krisponeit, J.-O.; Schmidt, T.; Falta, J.; Flege, J. I. The Cubic-to-Hexagonal Phase Transition of Cerium Oxide Particles: Dynamics and Structure. *Nanoscale* **2017**, *9*, 9352-9358.

(76) Shannon, R. D. Revised Effective Ionic Radii and Systematic Studies of Interatomic Distances in Halides and Chalcogenides. *Acta Crystallogr., Sect. A* **1976**, *32*, 751–767.

(77) Lee, G.; Lee, S. W.; Sohn, I.; Kwon, Y. C.; Song, J.; Son, C.-S.; WO2009035234-A2, Assigned to Hanwha Chemical Corporation, 2009.

(78) Wolf, A.; Mleczko, L.; Schlüter, O. F.-K.; Schubert, S. WO2010133313-A1, Assigned to Bayer Material Science, 2010.

(79) Hagemeyer, A.; Trübenbach, P.; Rieker, C. W.; Wünsch, M.; Watzenberger, O. EP Patent 0761594-A1, Assigned to BASF Aktiengesellschaft, 1997.

(80) Amrute, A. P.; Mondelli, C.; Hevia, M. A. G.; Pérez-Ramírez, J. Mechanism–Performance Relationships of Metal Oxides in Catalyzed HCl Oxidation. *ACS Catal.* **2011***, 1*, 583–590.

(81) Farra, R.; Eichelbaum, M.; Schlögl, R.; Szentmiklósi, L.; Schmidt, T.; Amrute, A. P.; Mondelli, C.; Pérez-Ramírez, J.; Teschner, D. Do Observations on Surface Coverage-reactivity Correlations Always Describe the True Catalytic Process? A Case Study on Ceria. *J. Catal.* **2013***, 297*, 119–127.

(82) Farra, R.; Girgsdies, F.; Frandsen, W.; Hashagen, M.; Schlögl, R.; Teschner, D. Synthesis and Catalytic Performance of CeOCl in Deacon Reaction. *Catal. Lett.* **2013***, 143*, 1012–1017.

(83) Farra, R.; Wrabetz, S.; Schuster, M. E.; Stotz, E.; Hamilton, N. G.; Amrute, A. P.; Pérez-Ramírez, J.; López, N.; Teschner, D. Understanding CeO_2 as a Deacon Catalyst by Probe Molecule Adsorption and in situ Infrared Characterisations. *Phys. Chem. Chem. Phys.* **2013***, 15*, 3454–3465.

(84) Fei, Z.; Xie, X.; Dai, Y.; Liu, H.; Chen, X.; Tang, J.; Cui, M.; Qiao, X. HCl Oxidation for Sustainable Cl_2 Recycle over the $Ce_xZr_{1-x}O_2$ Catalysts: Effects of Ce/Zr Ratio on Activity and Stability. *Ind. Eng. Chem. Res.* **2014***, 53*, 19438–19445.

(85) Li, D.; Wang, Z.; Huang, J.; Fei, Z.; Cui, M.; Qiao, X. Ultrafine CeO_2 Nanodots Embedded in Porous ZrO_2 for Efficient and Sustainable Chlorine Recycle through Hydrochloric Acid Catalytic Oxidation. *Chem. Sel.* **2020***, 5*, 12442–12449.

(86) Sun, Y.; Li, C.; Djerdj, I.; Khalid, O.; Cop, P.; Sann, J.; Weber, T.; Werner, S.; Turke, K.; Guo, Y.; Smarsly, B. M.; Over, H. Oxygen Storage Capacity versus Catalytic Activity of Ceria–zirconia Solid Solutions in CO and HCl Oxidation. *Catal. Sci. Technol.* **2019***, 9*, 2163–2172.

(87) Cop, P.; Maile, R.; Sun, Y.; Khalid, O.; Djerdj, I.; Esch, P.; Heiles, S.; Over, H.; Smarsly, B. M. Impact of Aliovalent/Isovalent Ions (Gd, Zr, Pr, and Tb) on the Catalytic Stability of Mesoporous Ceria in the HCl Oxidation Reaction. *ACS Appl. Nano Mater.* **2020***, 3*, 7406–7419.

(88) Zhou, K.; Wang, X.; Sun, X.; Peng, Q.; Li, Y. Enhanced Catalytic Activity of Ceria Nanorods from Well-defined Reactive Crystal Planes. *J. Catal.* **2005***, 229*, 206–212.

(89) Tasker, P. W.; The Stability of Ionic Crystal Surfaces. *J. Phys. C: Solid State Phys.* **1979**, *12*, 4977-4984.

(90) Olbrich, R.; Murgida, G. E.; Ferrari, V.; Barth, C.; Llois, A. M.; Reichling, M.; Ganduglia-Pirovano, M. V. Surface Stabilizes Ceria in Unexpected Stoichiometry. *J. Phys. Chem. C* **2017***, 121*, 6844–6851.

(91) Siegel, D. A.; Chueh, W. C.; El Gabaly, F.; McCarty, K. F.; de la Figuera, J.; Blanco-Rey, M. Determination of the Surface Structure of CeO_2(111) by Low-energy Electron Diffraction. *J. Chem. Phys.* **2013***, 139,* 114703.

(92) Barth, C.; Laffon, C.; Olbrich, R.; Ranguis, A.; Parent, P.; Reichling, M. A Perfectly Stoichiometric and Flat CeO_2(111) Surface on a Bulk-like Ceria Film. *Sci. Rep.* **2016**, *6*, 21165.

(93) Alexandrou, M.; Nix, R. M. The Growth, Structure and Stability of Ceria Overlayers on Pd(111). *Surf. Sci.* **1994***, 321*, 47–57.

(94) Schierbaum, K.-D. Ordered Ultra-thin Cerium Oxide Overlayers on Pt(111) Single Crystal Surfaces Studied by LEED and XPS. *Surf. Sci.* **1998***, 399*, 29–38.

(95) Luches, P.; Pagliuca, F.; Valeri, S. Structural and Morphological Modifications of Thermally Reduced Cerium Oxide Ultrathin Epitaxial Films on Pt(111). *Phys. Chem. Chem. Phys.* **2014***, 16*, 18848–18857.

(96) Castellarin-Cudia, C.; Surnev, S.; Schneider, G.; Podlucky, R.; Ramsey, M. G.; Netzer, F. P. Strain-induced Formation of Arrays of Catalytically Active Sites at the Metal–oxide Interface. *Surf. Sci.* **2004***, 554*, .120-126.

(97) Lu, J.-L.; Gao, H.-J.; Shaikhutdinov, S.; Freund, H.-J. Morphology and Defect Structure of the CeO_2(111) Films Grown on Ru(0001) as Studied by Scanning Tunneling Microscopy. *Surf. Sci.* **2006***, 600*, 5004–5010.

(98) Ma, S.; Rodriguez, J.; Hrbek, J. STM Study of the Growth of Cerium Oxide Nanoparticles on Au(111). *Surf. Sci.* **2008***, 602*, 3272–3278.

(99) Dvořák, F.; Stetsovych, O.; Steger, M.; Cherradi, E.; Matolínová, I.; Tsud, N.; Škoda, M.; Skála, T.; Mysliveček, J.; Matolín, V. Adjusting Morphology and Surface Reduction of CeO_2(111) Thin Films on Cu(111). *J. Phys. Chem. C* **2011***, 115*, 7496–7503.

(100) Kaemena, B.; Senanayake, S. D.; Meyer, A.; Sadowski, J. T.; Falta, J.; Flege, J. I. Growth and Morphology of Ceria on Ruthenium (0001). *J. Phys. Chem. C* **2013***, 117*, 221–232.

(101) Flege, J. I.; Kaemena, B.; Senanayake, S. D.; Höcker, J.; Sadowski, J. T.; Falta, J. Growth Mode and Oxidation State Analysis of Individual Cerium Oxide Islands on Ru(0001). *Ultramicroscopy* **2013***, 130*, 87–93.

(102) Stetsovych, V.; Pagliuca, F.; Dvořák, F.; Duchoň, T.; Vorokhta, M.; Aulická, M.; Lachnitt, J.; Schernich, S.; Matolínová, I.; Veltruská, K.; Skála, T.; Mazur, D.; Mysliveček, J.; Libuda, J.; Matolín, V. Epitaxial Cubic Ce_2O_3 Films via Ce–CeO_2 Interfacial Reaction. *J. Phys. Chem. Lett.* **2013***, 4*, 866–871.

(103) Duchoň, T.; Dvořák, F.; Aulická, M.; Stetsovych, V.; Vorokhta, M.; Mazur, D.; Veltruská, K.; Skála, T.; Mysliveček, J.; Matolínová, I.; Matolín, V. Ordered Phases of Reduced Ceria As Epitaxial Films on Cu(111). *J. Phys. Chem. C* **2014***, 118*, 357–365.

(104) Duchoň, T.; Dvořák, F.; Aulická, M.; Stetsovych, V.; Vorokhta, M.; Mazur, D.; Veltruská, K.; Skála, T.; Mysliveček, J.; Matolínová, I.; Matolín, V. Comment on "Ordered Phases of Reduced Ceria as Epitaxial Films on Cu(111)". *J. Phys. Chem. C* **2014***, 118*, 5058–5059.

(105) Murgida, G. E.; Ferrari, V.; Llois, A. M.; Ganduglia-Pirovano, M. V. Reduced CeO_2(111) Ordered Phases as Bulk Terminations: Introducing the Structure of Ce_3O_5. *Phys. Rev. Mater.* **2018**, *2*, 083609.

(106) Han, Z.-K.; Yang, Y.-Z.; Zhu, B.; Ganduglia-Pirovano, M. V.; Gao, Y. Unraveling the Oxygen Vacancy Structures at the Reduced CeO_2(111) Surface. *Phys. Rev. Mater.* **2018**, *2*, 035802.

(107) Kümmerle, E. A.; Heger, G. The Structures of C-$Ce_2O_{3+\delta}$, Ce_7O_{12}, and $Ce_{11}O_{20}$. *J. Solid State Chem.* **1999**, *147* ,485-500.

(108) Mullins, D. R.; Robbins, M. D.; Zhou, J. Adsorption and Reaction of Methanol on Thin-film Cerium Oxide. *Surf. Sci.* **2006***, 600*, 1547–1558.

(109) Henderson, M. A.; Perkins, C. L.; Engelhard, M. H.; Thevuthasan, S.; Peden, C. Redox Properties of Water on the Oxidized and Reduced Surfaces of CeO_2. *Surf. Sci.* **2003***, 526*, 1–18.

(110) Fernández-Torre, D.; Carrasco, J.; Ganduglia-Pirovano, M. V.; Pérez, R. Hydrogen Activation, Diffusion, and Clustering on CeO_2(111): a DFT+U study. *J. Chem. Phys.* **2014***, 141*, 14703.

(111) Capdevila-Cortada, M.; Vilé, G.; Teschner, D.; Pérez-Ramírez, J, López, N. Reactivity Descriptors for Ceria in Catalysis. *App. Catal. B* **2016**, *197*, 299-312.

(112) Mars, P.; van Krevelen, D. W. Oxidations Carried out by Means of Vanadium Oxide Catalysts. *Chem. Eng. Sci.* **1954***, 3*, 41–59.

(113) Zeng, L.; Cheng, Z.; Fan, J. A.; Fan, L.-S.; Gong, J. Metal Oxide Redox Chemistry for Chemical Looping Processes. *Nat. Rev. Chem.* **2018**, *2*, 349–364.

(114) Pan, H. Y.; Minet, R. G.; Benson, S. W.; Tsotsis, T. T. Process for Converting Hydrogen Chloride to Chlorine. *Ind. Eng. Chem. Res.* **1994**, *33*, 2996–3003.

(115) Han, M.; Chang, P.; Hu, G.; Chen, Z.; Wang, D.; Wei, F. Conversion of Hydrogen Chloride to Chlorine by Catalytic Oxidation in a Two-zone Circulating Fluidized bed Reactor. *Chem. Eng. Process.* **2011**, *50*, 593–598.

(116) Nieken, U.; Watzenberger, O. Periodic Operation of the Deacon Process. *Chem. Eng. Sci.* **1999**, *54*, 2619–2626.

(117) Hu, Z.; Metiu, H. Halogen Adsorption on CeO_2: The Role of Lewis Acid–Base Pairing. *J. Phys. Chem. C* **2012**, *116*, 6664–6671.

(118) Metiu, H.; Chrétien, S.; Hu, Z.; Li, B.; Sun, X. Chemistry of Lewis Acid–Base Pairs on Oxide Surfaces. *J. Phys. Chem. C* **2012**, *116*, 10439–10450.

(119) Cen, W.; Liu, Y.; Wu, Z.; Liu, J.; Wang, H.; Weng, X. Cl Species Transformation on CeO_2(111) Surface and Its Effects on CVOCs Catalytic Abatement: A First-Principles Investigation. *J. Phys. Chem. C* ***2014***, *118*, 6758–6766.

(120) Yin, L.-L.; Gong, X.-Q. Influence of Cl Substitution on the Electronic Structure and Catalytic Activity of Ceria. *Sci. China Chem.* **2015**, *58*, 601–606.

(121) www.maxiv.lu.se/beamlines-accelerators/beamlines/flexpes/experimental-station/surface-material-science-branch/ (accessed 2024-03-27).

(122) Seah, M. P.; Dench, W. A. Quantitative Electron Spectroscopy of Surfaces: A Standard Data Base for Electron Inelastic Mean Free Paths in Solids. *Surf. Interface Anal.* **1979**, *1*, 2–11.

(123) Cooper, J. W. Photoionization from Outer Atomic Subshells. A Model Study. *Phys. Rev.* **1962**, *128*, 681–693.

(124) Yeh, J. J.; Lindau, I. Atomic Subshell Photoionization Cross Sections and Asymmetry Parameters: $1 \leqslant Z \leqslant 103$. *At. Data Nucl. Data Tables* **1985**, *32*, 1–155.

(125) Krause, P. P. T. Visualisierung des elektrochemischen Oxidationsverhaltens der Ru(0001)-Oberfläche. Dissertation, Justus-Liebig-University Giessen, Giessen, Germany, 2015.

(126) Over, H.; Bludau, H.; Skottke-Klein, M.; Moritz, W.; Ertl. G.; Campbell, C. T. Coverage Dependence of Adsorption-Site Geometry in the Cs/Ru(0001) System: A Low-Energy Electron Diffraction Analysis. *Phys. Rev. B* **1992**, *45*, 8638-8649.

(127) Hofmann, J. P.; Rohrlack, S. F.; Heß, F.; Goritzka, J. C.; Krause, P. P. T.; Seitsonen, A. P.; Moritz, W.; Over, H. Adsorption of Chlorine on Ru(0001)—A Combined Density Functional Theory and Quantitative Low Energy Electron Diffraction Study. *Surf. Sci.* **2012**, *606*, 297–304.

(128) Instruction Manual UHV Evaporator EFM3, Version 2.2, Focus GmbH, Taunusstein, Germany, 1999.

(129) Thermal Gas Cracker TC50-Manual, Tech. Rep., 2.1, Oxford Applied Research Ltd, Witney, U.K., 2005.

(130) Naya, K.; Ishikawa, R.; Fukui, K. Oxygen-Vacancy-Stabilized Positively Charged Au Nanoparticles on CeO_2(111) Studied by Reflection−Absorption Infrared Spectroscopy. *J. Phys. Chem. C* **2009**, *113*, 10726–10730.

(131) Dvořák, F.; Szabová, L.; Johánek, V.; Camellone, M. F.; Stetsovych, V.; Vorokhta, M.; Tovt, A.; Skála, T.; Matolínová, I.; Tateyama, Y.; Mysliveček, J.; Fabris, S.; Matolín, V. Bulk Hydroxylation and Effective Water Splitting by Highly Reduced Cerium Oxide: The Role of O Vacancy Coordination. *ACS Catal.* **2018***, 8*, 4354–4363.

(132) Kotani, A.; Jo, T.; Parlebas, J. C. Many-body Effects in Core-level Spectroscopy of Rare-earth Compounds. *Adv. Phys.* **1988***, 37*, 37–85.

(133) Kotani, A.; Ogasawara, H. Theory of Core-level Spectroscopy of Rare-earth Oxides. *J. Electron Spectrosc. Relat. Phenom.* **1992***, 60*, 257–299.

(134) Signorelli, A. J.; Hayes., R. G., X-Ray Photoelectron Spectroscopy of Various Core Levels of Lanthanide Ions: The Roles of Monopole Excitation and Electrostatic Coupling. *Phys. Rev. B,* **1973**, *8*, 81-86

(135) Kowalczyk, S. P.; Edelstein, N.; McFeely, F. R.; Ley, L.; Shirley, D. A. X-ray Photoemission Spectra of the 4d Levels in Rare-earth Metals. *Chem. Phys. Lett.* **1974***, 29*, 491–495.

(136) Kaindl, G.; Kalkowski, G.; Brewer, W. D.; Perscheid, B.; Holtzberg, F. *M*-edge X-ray Absorption Spectroscopy of 4*f* Instabilities in Rare-earth Systems (Invited). *J. Appl. Phys.* **1984**, *55*, 1910–1915.

(137) Yagci, O. The $M_{4,5}$ Photo-Absorption Spectra of Cerium in CeO_2 and Oxidation of Metallic Cerium. *J. Phys. C: Solid State Phys.* **1986**, *19*, 3487–3495.

(138) Mullins, D.; Overbury, S.; Huntley, D. Electron Spectroscopy of Single Crystal and Polycrystalline Cerium Oxide Surfaces. *Surf. Sci.* **1998**, *409*, 307–319.

(139) Hackl, J.; Duchoň, T.; Gottlob, D. M.; Cramm, S.; Veltruská, K.; Matolín, V.; Nemšák, S.; Schneider, C. M. On the Growth Mechanisms of Polar (100) Surfaces of Ceria on Copper (100). *Surf. Sci.* **2018**, *671*, 1–5.

(140) Heinz, K. Structural Analysis of Surfaces by LEED. *Prog. Surf. Sci.* **1988**, *27*, 239–326.

(141) Over, H.; Gierer, M.; Bludau, H.; Ertl, G.; Tong, S. Y. Fingerprinting Technique in Low-Energy Electron Diffraction. *Surf. Sci.* **1994**, *314*, 243–268.

(142) Pendry, J. B. Reliability Factors for LEED Calculations. *J. Phys. C: Solid State Phys.* **1980***, 13*, 937–944.

(143) Zhang, B.; Liu, J.; Shen, F. Heterogeneous Mercury Oxidation by HCl over CeO_2 Catalyst: Density Functional Theory Study. *J. Phys. Chem. C* **2015**, *119*, 15047–15055

(144) Allahgholi, A.; Flege, J. I.; Thiess, S.; Drube, W.; Falta, J. Oxidation-State Analysis of Ceria by x-Ray Photoelectron Spectroscopy. *Chem. Phys. Chem.* **2015**, *16*, 1083-1091.

(145) Crihan, D.; Knapp, M.; Zweidinger, S.; Lundgren, E.; Weststrate, C. J.; Andersen, J. N.; Seitsonen, A. P.; Over, H. Stable Deacon Process for HCl Oxidation over RuO_2. *Angew. Chem. Int. Ed.* **2008**, *47*, 2131–2134.

(146) Hofmann, J. P.; Zweidinger, S.; Knapp, M.; Seitsonen, A. P.; Schulte, K.; Andersen, J. N.; Lundgren, E.; Over, H. Hydrogen-Promoted Chlorination of RuO_2(110). *J. Phys. Chem. C* **2010**, *114*, 10901–10909.

(147) Zhang, D.; Han, Z.-K.; Murgida, G. E.; Ganduglia-Pirovano, M. V.; Gao, Y. Oxygen-Vacancy Dynamics and Entanglement with Polaron Hopping at the Reduced CeO_2(111) Surface. *Phys. Rev Lett.* **2019**, *122*, 96101.

(148) Mullins, D. R.; Albrecht, P. M.; Chen, T. L.; Calaza, F. C.; Biegalski, M. D.; Christen, H. M.; Overbury, S. H. Water Dissociation on CeO_2(100) and CeO_2(111) Thin Films. *J. Phys. Chem. C* **2012**, *116*, 19419–19428.

(149) Liu, Z.; Grinter, D. C.; Lustemberg, P. G.; Nguyen-Phan, T.-D.; Zhou, Y.; Luo, S.; Waluyo, I.; Crumlin, E. J.; Stacchiola, D. J.; Zhou, J., Carrasco, J.; Busnengo, H. F.; Ganduglia-Pirovano, M. V.; Senanayake, S. D.; Rodriguez, J. A. Dry Reforming of Methane on a Highly-Active Ni-CeO_2 Catalyst: Effects of Metal-Support Interactions on C-H Bond Breaking. *Angew. Chem., Int. Ed.* **2016**, *55*, 7455–7459.

(150) Posada-Borbón, A.; Bosio, N.; Grönbeck, H. On the Signatures of Oxygen Vacancies in O1s Core Level Shifts. *Surf. Sci.* **2021**, *705*, 121761.

(151) Murgida, G. E.; Ganduglia-Pirovano, M. V. Evidence for Subsurface Ordering of Oxygen Vacancies on the Reduced CeO_2(111) Surface Using Density-Functional and Statistical Calculations. *Phys. Rev. Lett.* **2013**, *110*, 246101.

(152) Huang, M.; Fabris, S. Role of Surface Peroxo and Superoxo Species in the Low-Temperature Oxygen Buffering of Ceria: Density Functional Theory Calculations. *Phys. Rev. B* **2007**, *75*, 081404(R).

(153) Zhao, Y.; Teng, B.-T.; Wen, X.-D.; Zhao, Y.; Chen, Q.-P.; Zhao, L.-H.; Luo, M.-F. Superoxide and Peroxide Species on CeO_2(111), and Their Oxidation Roles. *J. Phys. Chem. C* **2012**, *116*, 15986–15991.

(154) Ganduglia-Pirovano, M. V.; Da Silva, J. L. F.; Sauer, J. Density-Functional Calculations of the Structure of Near-Surface Oxygen Vacancies and Electron Localization on CeO_2(111). *Phys. Rev. Lett.* **2009**, *102*, 26101.

(155) Preda, G.; Pacchioni, G. Formation of Oxygen Active Species in Ag-modified CeO_2 Catalyst for Soot Oxidation: A DFT study. *Catal. Tod.* **2011**, *177*, 31–38.

(156) Bosio, N.; Di, M.; Skoglundh, M.; Carlsson, P.-A.; Grönbeck, H. Interface Reactions Dominate Low-Temperature CO Oxidation Activity over Pt/CeO_2. *J. Phys. Chem. C* **2022**, *126*, 16164–16171.

(157) Lykhach, Y.; Kozlov, S. M.; Skála, T.; Tovt, A.; Stetsovych, V.; Tsud, N.; Dvořák, F.; Johánek, V.; Neitzel, A.; Mysliveček, J., Fabris, S.; Matolín, V., Neyman, K. M., Libuda J. Counting Electrons on Supported Nanoparticles. *Nat. Mater.* **2016**, *15*, 284–288.

(158) Hofmann, J. P.; Zweidinger, S.; Seitsonen, A. P.; Farkas, A.; Knapp, M.; Balmes, O.; Lundgren, E.; Andersen, J. N.; Over, H. Dynamic Response of Chlorine Atoms on a RuO_2(110) Model Catalyst Surface. *Phys. Chem. Chem. Phys.* **2010**, *12*, 15358–15366.

(159) Wan, W.; Geiger, J.; Berdunov, N.; Lopez Luna, M.; Chee, S. W.; Daelman, N.; López, N.; Shaikhutdinov, S.; Roldan Cuenya, B. Highly Stable and Reactive Platinum Single Atoms on Oxygen Plasma-Functionalized CeO_2 Surfaces: Nanostructuring and Peroxo Effects. *Angew. Chem., Int. Ed.* **2022**, *61*, e202112640.

(160) Wolf, M. J.; Larsson, E. D.; Hermansson, K. Oxygen Chemistry of Halogen-Doped CeO_2(111). *Phys. Chem. Chem. Phys.* **2021**, *23*, 19375–19385.

(161) Paier, J.; Penschke, C: Sauer, J. Oxygen Defects and Surface chemistry of Ceria: Quantum chemical Studies Compared to Experiment. *Chem. Rev.* **2013**, *113*, 3949–3985.

(162) Yang, C.; Yu, X.; Heißler, S.; Weidler, P. G.; Nefedov, A.; Wang, Y.; Wöll, C.; Kropp, T.; Paier, J.; Sauer, J. O_2 Activation on Ceria Catalysts – The Importance of Substrate Crystallographic Orientation. *Angew. Chem., Int. Ed.* **2017**, *56*, 16399–16404.

(163) Schilling, C.; Ganduglia-Pirovano, M. V.; Hess, C. Experimental and Theoretical Study on the Nature of Adsorbed Oxygen Species on Shaped Ceria Nanoparticles. *J. Phys. Chem. Lett.* **2018**, *9*, 6593–6598.

(164) Chueh, W. C.; Hao, Y.; Jung, W.; Haile, S. M. High Electrochemical Activity of the Oxide Phase in Model Ceria-Pt and Ceria-Ni Composite Anodes. *Nat. Mater.* **2011***, 11*, 155–161.

(165) Feng, Z. A.; Machala, M. L.; Chueh, W. C. Surface Electrochemistry of CO_2 Reduction and CO Oxidation on Sm-doped CeO_{2-x}: Coupling between Ce^{3+} and Carbonate Adsorbates. *Phys. Chem. Chem. Phys.* **2015***, 17*, 12273–12281.

(166) Chueh, W. C.; McDaniel, A. H.; Grass, M. E.; Hao, Y.; Jabeen, N.; Liu, Z.; Haile, S. M.; McCarty, K. F.; Bluhm, H.; El Gabaly, F. Highly Enhanced Concentration and Stability of Reactive Ce^{3+} on Doped CeO_2 Surface Revealed In Operando. *Chem. Mater.* **2012***, 24*, 1876–1882.

(167) Yao, H. C.; Yao, Y. F. Y. Ceria in Automotive Exhaust Catalysts: I. Oxygen Storage. *J. Catal.* **1984**, *86*, 254–265.

(168) Li, P.; Chen, X.; Li, Y.; Schwank, J. W. A Review on Oxygen Storage Capacity of CeO_2-Based Materials: Influence Factors, Measurement Techniques, and Applications in Reactions Related to Catalytic Automotive Emissions Control. *Catal. Today* **2019**, *327*, 90–115.

(169) Grasselli, R. K. Fundamental Principles of Selective Heterogeneous Oxidation Catalysis. *Top. Catal.* **2002**, *21*, 79–88.

(170) Wachs, I. E. Recent Conceptual Advances in the Catalysis Science of Mixed Metal Oxide Catalytic Materials. *Catal. Today* **2005**, *100*, 79–94.

(171) Merkle, R.; Maier, J. The Significance of Defect Chemistry for the Rate of Gas–Solid Reactions: Three Examples. *Top. Catal.* **2006**, *38*, 141–145.

(172) Montini, T.; Melchionna, M.; Monai, M.; Fornasiero, P. Fundamentals and Catalytic Applications of CeO_2-Based Materials. *Chem. Rev.* **2016**, *116*, 5987–6041.

(173) Campbell, C. T.; Peden, C. H. F. Oxygen Vacancies and Catalysis on Ceria Surfaces. *Science* **2005**, *309*, 713–714.

(174) Esch, F.; Fabris, S.; Zhou, L.; Montini, T.; Africh, C.; Fornasiero, P.; Comelli, G.; Rosei, R. Electron Localization Determines Defect Formation on Ceria Substrates. *Science* **2005**, *309*, 752–755.

(175) Chung, C.-H.; Tu F.-Y.; Chiu, T.-A.; Wu, T.-T.; Yu, W.-Y. Critical Roles of Surface Oxygen Vacancy in Heterogeneous Catalysis over Ceria-based Materials: A Selected Review. *Chem. Lett.* **2021**, *50*, 856–865.

(176) Che, M.; Tench, A. J. Characterization and Reactivity of Mononuclear Oxygen Species on Oxide Surfaces. *Adv. Catal.* **1982**, *31*, 77–133.

(177) Li, C.; Domen, K.; Maruya, K.; Onishi, T. Dioxygen Adsorption on Well-Outgassed and Partially Reduced Cerium Oxide Studied by FT-IR. *J. Am. Chem. Soc.* **1989**, *111*, 7683–7687.

(178) Pushkarev, V. V.; Kovalchuk, V. I.; d'Itri, J. L. Probing Defect Sites on the CeO_2 Surface with Dioxygen. *J. Phys. Chem. B* **2004**, *108*, 5341–5348.

(179) Martínez-Arias, A.; Conesa, J. C.; Soria, J. O_2-probe EPR as a Method for Characterization of Surface Oxygen Vacancies in Ceria-based Catalysts. *Res. Chem. Intermed.* **2007**, *33*, 775–791.

(180) Wu, Z.; Li, M.; Howe, J.; Meyer III, H. M.; Overbury, S. H. Probing Defect Sites on CeO_2 Nanocrystals with Well-Defined Surface Planes by Raman Spectroscopy and O_2 Adsorption. *Langmuir* **2010**, *26*, 16595–16606.

(181) Schilling, C.; Hofmann, A.; Hess, C.; Ganduglia-Pirovano, M. V. Raman Spectra of Polycrystalline CeO_2: A Density Functional Theory Study. *J. Phys. Chem. C* **2017**, *121*, 20834–20849.

(182) Anpo, M.; Costentin, G.; Giamello, E.; Lauron-Pernot, H.; Sojka, Z. Characterisation and Reactivity of Oxygen Species at the Surface of Metal Oxides. *J. Catal.* **2021**, *393*, 259–280.

(183) Etim, U. J.; Bai, P.; Gazit, O. M.; Zhong, Z. Low-Temperature Heterogeneous Oxidation Catalysis and Molecular Oxygen Activation. *Catal. Rev.* **2023**, *65*, 239–425.

(184) Guzman, J.; Carrettin, S.; Corma, A. Spectroscopic Evidence for the Supply of Reactive Oxygen During CO Oxidation Catalyzed by Gold Supported on Nanocrystalline CeO_2. *J. Am. Chem. Soc.* **2005**, *127*, 3286–3287.

(185) Choi, Y. M.; Abernathy, H.; Chen, H.-T.; Lin, M. C.; Liu, M. Characterization of O_2-CeO_2 Interactions Using in situ Raman Spectroscopy and First-Principle Calculations. *ChemPhysChem* **2006**, *7*, 1957–1963.

(186) Camellone, M. F.; Fabris, S. Reaction Mechanisms for the CO Oxidation on Au/CeO_2 Catalysts: Activity of Substitutional Au^{3+}/Au^{+} Cations and Deactivation of Supported Au^{+} Adatoms. *J. Am. Chem. Soc.* **2009**, *131*, 10473–10483.

(187) Wang, Y.-G.; Mei, D.; Glezakou, V.-A.; Li, J.; Rousseau, R. Dynamic Formation of Single-atom Catalytic Active Sites on Ceria-supported Gold Nanoparticles. *Nat. Commun.* **2015**, *6*, 6511.

(188) Soler, L.; Casanovas, A.; Escudero, C.; Pérez-Dieste, V.; Aneggi, E.; Trovarelli A.; Llorca, J. Ambient Pressure Photoemission Spectroscopy Reveals the Mechanism of Carbon Soot Oxidation in Ceria-Based Catalysts. *ChemCatChem* **2016**, *8*, 2748–2751.

(189) Schilling, C.; Ziemba, M.; Hess, C.; Ganduglia-Pirovano, M. V. Identification of Single-atom Active Sites in CO Oxidation Over Oxide-supported Au Catalysts. *J. Catal.* **2020**, *383*, 264–272.

(190) Piliai, L.; Matvija, P.; Dinhová, T. N.; Khalakhan, I.; Skála, T.; Doležal, Z.; Bezkrovnyi, O.; Kepinski, L.; Vorokhta, M.; Matolínová, I. In Situ Spectroscopy and Microscopy Insights into the CO Oxidation Mechanism on Au/CeO_2(111). *ACS Appl. Mater. Interfaces* **2022**, *14*, 56280–56289.

(191) Wang, J.; Cheng, D.-G.; Chen, F.; Zhan, X. Chlorine-Decorated Ceria Nanocubes for Facilitating Low-Temperature Cyclohexane Oxidative Dehydrogenation: Unveiling the Decisive Role of Surface Species and Acid Properties. *ACS Catal.* **2022**, *12*, 4501–4516.

(192) Su, Z.; Li, X.; Si, W.; Artiglia, L.; Peng, Y.; Chen, J.; Wang, H.; Chen, D.; Li, J. Probing the Actual Role and Activity of Oxygen Vacancies in Toluene Catalytic Oxidation: Evidence from In Situ XPS/NEXAFS and DFT + U Calculation. *ACS Catal.* **2023***, 13*, 3444–3455.

(193) Zhu. Y.; Wang, J.; Patel, S. B.; Li, C.; Head, A. R.; Boscobinik, J. A.; Zhou, G. Tuning the Surface Reactivity of Oxides by Peroxide Species. *Proc. Natl. Acad. Sci. U. S. A.* **2023**, *120*, e3315189120..

(194) Li, C.; Hess, F.; Djerdj, I.; Chai, G.; Sun, Y.; Guo, Y.; Smarsly, B. M.; Over, H. The Stabilizing Effect of Water and High Reaction Temperatures on the CeO_2-Catalyst in the Harsh HCl Oxidation Reaction. *J. Catal.* **2018***, 357*, 257–262.

(195) Monkhorst, H. J.; Pack, J. D. Special Points for Brillouin-Zone Integrations. *Phys. Rev. B* **1976**, *13*, 5188−5192.

(196) Kresse, G.; Hafner, J. Ab Initio Molecular Dynamics for Liquid Metals. *Phys. Rev. B: Condens. Matter Mater. Phys.* **1993**, *47*, 558–561.

(197) Kresse, G.; Hafner, J. Ab Initio Molecular-Dynamics Simulation of the Liquid-Metal-Amorphous-Semiconductor Transition in Germanium. *Phys. Rev. B: Condens. Matter Mater. Phys.* **1994**, *49*, 14251–14269.

(198) Kresse, G.; Furthmüller, J. Efficiency of Ab-Initio Total Energy Calculations for Metals and Semiconductors Using a Plane-Wave Basis Set. *Comput. Mater. Sci.* **1996**, *6*, 15–50.

(199) Kresse, G.; Furthmüller, J. Efficient Iterative Schemes for Ab Initio Total-Energy Calculations Using a Plane-Wave Basis Set. *Phys. Rev. B: Condens. Matter Mater. Phys.* **1996**, *54*, 11169–11186.

(200) Kresse, G.; Joubert, D. From Ultrasoft Pseudopotentials to the Projector Augmented-Wave Method. *Phys. Rev. B: Condens. Matter Mater. Phys.* **1999**, *59*, 1758–1775.

(201) Blöchl, P. E. Projector Augmented-Wave Method. *Phys. Rev. B: Condens. Matter Mater. Phys.* **1994**, *50*, 17953–17979.

(202) Dudarev, S. L.; Botton, G. A.; Savrasov, S. Y.; Humphreys, C. J.; Sutton, A. P. Electron-Energy-Loss Spectra and the Structural Stability of Nickel Oxide: An LSDA+U Study. *Phys. Rev. B: Condens. Matter Mater. Phys.* **1998**, *57*, 1505–1509.

(203) Perdew, J. P.; Burke, K.; Ernzerhof, M. Generalized Gradient Approximation Made Simple. *Phys. Rev. Lett.* **1996**, *77*, 3865–3868.

(204) Henkelman, G.; Uberuaga, B. P.; Jónsson, H. A Climbing Image Nudged Elastic Band Method for Finding Saddle Points and Minimum Energy Paths. *J. Chem. Phys.* **2000**, *113*, 9901–9904.